INTER-LAYER COHERENCE LENGTH AND THE CRITICAL TEMPERATURE ANISOTROPY OF LSCO

Itay Mangel

INTER-LAYER COHERENCE LENGTH AND THE CRITICAL TEMPERATURE ANISOTROPY OF LSCO

Research Thesis

Submitted in partial fulfillment of the requirements

for the degree of Doctor of Philosophy

Itay Mangel

Submitted to the Senate

of the Technion — Israel Institute of Technology

Av 5784 Haifa August 2024

The Research was done in the Department of Physics under The Supervision of Prof. Amit Keren.

Some results in this thesis have been published as articles by the author and research collaborators in conferences and journals during the authors PhD period, the most up-to-date versions of which being:

Mangel, I., Kapon, I., Blau, N., Golubkov, K., Gavish, N., & Keren, A. 2020, Stiffnessometer: A magnetic-field-free superconducting stiffness meter and its application, PHYSICAL REVIEW B 102, 024502 (2020)

Mangel, I., & Keren, A. 2024, Ground-state Inter-plane Superconducting Coherence Length of $La_{1.875}Sr_{0.125}CuO_4$, PHYSICAL REVIEW B 109, 094519 (2024)

Samanta, A., Mangel, I., Keren, A., Arovas, D.P., & Auerbach, A. 2024, Two critical temperatures conundrum in $La_{1.83}Sr_{0.17}CuO_4$, SciPost Phys. 16, 148 (2024)

Ethics Statement

The author of this thesis states that the research, including the collection, processing and presentation of data, addressing and comparing to previous research, etc., was done entirely in an honest way, as expected from scientific research that is conducted according to the ethical standards of the academic world. Also, reporting the research and its results in this thesis was done in an honest and complete manner, according to the same standards.

Acknowledgments

The generous financial help of the Israeli Science Foundation (Grant. No. 1251/19 and 3875/21) is gratefully acknowledged.

Contents

List of Figures

Abstract

The obvious interest in superconductivity (SC) due to it extraordinary features, keeps the field as relevant as ever and the search for better materials calls for better ways to evaluate and investigate them. The new technique for measuring SC parameters and their anisotropy was developed with significant advantages over traditional techniques. It is demonstrated on a high temperature superconductor (HTSC) - $La_{2-x}Sr_xCuO_4$ (LSCO), where the x in the chemical formula is the hole-doping of the sample.

The primary advantages of our technique are that the system is in thermodynamic equilibrium during the measurement, there is no direct magnetic field on the sample and hence, there is no vortexes dynamics or demagnetization factors, no leads on the sample, and it is based on a commercial tabletop system.

The fist part of the work explains the technique in details and shows results for $x = 0.17$ sample. This part starts with some verification and simulations, then shows experimental results for LSCO ring with doping $x = 0.17$ and data analysis, and finishes with the behavior of λ and ξ as function of temperature when approaching the critical temperature (T_c).

The second part of the work demonstrates how the technique is used with extremely high currents and at low temperatures. In this part, the theoretical derivation was first tested on pure Nb rings with different physical parameters (inner radius, outer radius, and height) and then applied on two rings from the same single crystal of LSOC with $x = 0.125$. Each ring had a different crystalian orientation so that in one ring the SC current is always parallel to the CuO_2 planes (c-ring) while on the other, the SC current must cross to the CuO_2 planes (a-ring). This way, we where able to measure the critical in-plane and out-of-plane critical current and extract from it the anisotropic coherence length. The in-plane critical current was not reached, but we can still set an upper limit on the in plane coherence length of $\xi_{ab} < 2.3$ nm. The out-of-plane critical current was reached and the in plane coherence length was found to be $\xi_c = 1.3 \pm 0.1$ nm. The similarity of ξ_{ab} and ξ_c shows small anisotropy at low temperatures.

The third part of the work deals with the puzzling observation of anisotropic critical temperature and trying to find its origin. A finite size effect was the main suspect and

two LSCO (a- and c-) rings of the same crystal of doping $x = 0.125$ were measured several times. Between each measurement one of the ring's physical parameter was changed. The height was reduced by fine polishing of the ring and the outer radius was reduced by femtosecond laser with high precision. A Monte Carlo (MC) numerical simulation for the 3DXY-model and an analytical derivation of a 1D Josephson array was done to show that the apparent difference in T_c is indeed the result of the finite size effect and the finite detection limit. By fitting the analytical derivation to the measurements, the stiffness anisotrophy near T_c was found to be $\alpha = 4.1 \times 10^{-5}$.

Abbreviations and Notations

SC	:	Superconductor/Superconductivity
BCS	:	Bardeen Cooper Schrieffer
HTSC	:	High temperature super conductors
MV	:	Mermin Wagner
BKT	:	Berezinskii Kosterlitz Thouless
LSCO	:	$La_{2-x}Sr_xCuO_4$
ID	:	Inner diameter
OD	:	Outer diameter
VP	:	Vector potential
EC	:	Excitation coil
ZGFC	:	Zero gauge field cooling
GFC	:	Gauge field cooling
SQUID	:	Superconducting quantum interference device
GL	:	Ginsburg Landau
TSFZ	:	Traveling solvent floating zone
a-ring	:	LSCO ring. a-axis is aligned to rings axis
c-ring	:	LSCO ring. c-axis is aligned to rings axis
MC	:	Monte Carlo
PDE	:	Partial differential equation
T_c	:	Critical temperature
ρ_s	:	Superconducting Stiffness
λ	:	Superconducting penetration length
ξ	:	Superconducting coherence length
H_{c2}	:	Second critical field of
Φ_0	:	Magnetic flux quanta
Φ_c	:	Critical magnetic flux

Chapter 1

Introduction

Superconductivity (SC) is a special phase characterized by many unique phenomena such as zero electrical resistance and perfect diamagnetism (Meissner effect). Classical SC can be explained by the BCS-Theory (named after John Bardeen, Leon Cooper, and John Robert Schrieffer) which considers attractive interaction between electrons through electron-phonon coupling. It is common to think of the charge carriers in a SC as pairs of electrons called Cooper-pairs rather than individual electrons. The critical temperature (or transition temperature) T_c refers to a temperature where the transition between the SC phase and the normal phase happens. High-temperature superconductivity (HTSC) was discovered in the mid-80's and the mechanism allowing it cannot be explained by the BCS theory. A major group of HTSC is the cuprates family, characterized by their nearly tetragonal unit cell structure that forms layers of CuO_2 with different metals and oxygen between the layers. Those materials show a plethora of phases (besides SC) and are highly anisotropic. This anisotropy manifests in both the penetration length λ and the coherence length ξ.

The inter-layer zero temperature coherence length $\xi_\perp$ is especially important because it rules the coupling between the layers, but it is also hard to measure. A standard way to measure ξ is by measuring the second critical field H_{c2}, but if $\xi \sim 1$ nm then $H_{c2} \sim 200$ T. Another way to find ξ is by measuring the vortex diameter, however, it is nearly impossible to cut the sample smooth enough for scanning probes perpendicular to the layers to see $\xi_\perp$. The most common way to determine ξ is by measuring H_{c2} close to T_c where it is relatively small and then extrapolate to $T = 0$ following one theory or another, but the choice of theory can lead to very different results at $T = 0$.

Another aspect of the strong anisotropy is manifested in measurements of T_c. Many different observations show a temperature range where SC current can flow only perpendicular to the layers as if it is a 2D SC. In 2D systems, there is no long-range order according to the Mermin and Wagner (MV) theorem, but the Berezinskii-Kosterlitz-Thouless (BKT) theory allows for short-range correlation and SC to exist in quasi-2D systems (with a finite copling between the layers) below a certain temperature T_{BKT}. But T_{BKT} must be smaller than the thermodynamic 3D T_c. It cannot explain the temperature range where SC exist only in 2D ($T_c^{c-ring} > T_c^{a-ring}$). In other words, there should be only 1 T_c in a 3D system. This difference in the critical temperature ΔT_c is a puzzling conundrum of fundamental physics.

The following sections review the cuprate family and LSCO, which are the heart of this work, and the anisotropy in its different forms. Chapter 2 describes the sample growth and preparation, the experimental setup, and the data analysis. Chapter 3 gives a more detailed account of the stiffness measurements and presents measurements of λ and ξ close to T_c. Chapter 4 presents the measurements of the ground state $\xi_\perp$ and finally Chap. 5 explains our explanation to the ΔT_c conundrum.

1.1 LSCO phase diagram[1]

The cuprates phase diagram is very rich with many motives that are typical to all members of the family. One member of this family is $La_{2-x}Sr_xCuO_4$ (LSCO). Figure. 1.1 shows LSCO's unit cell. The crystalline vectors a, b, and c are defined so that a and b are inside the CuO_2 plane and c is perpendicular to the plane. The parent compound (where $x = 0$) La_2CuO_4 has one electron per unit cell (half filling) and is antiferromagnetic with Néel temperature T_N around room temperature. When lanthanum atoms (La) are replaced by strontium atoms (Sr) (increasing x in the chemical formula) the number of electrons per CuO_2 unit decreases (hole doping), the antiferromagnetic state diminishes and T_N drops rapidly reaching $T_N = 0$ at $x \sim 0.02$. Superconductivity start at $x \sim 0.07$ and T_c increases with doping until $x \sim 0.15$ (optimal doping). Then, it decreases with doping until $x \sim 0.26$, forming the SC dome. Nevertheless, the story does not end with SC. Above $x \sim 0.26$ at low enough temperatures, the system behaves as a Fermi-liquid with T^2 resistivity dependence. At higher temperatures, the system is in the strange-

[1] In this section I rely mostly on (4),(5).

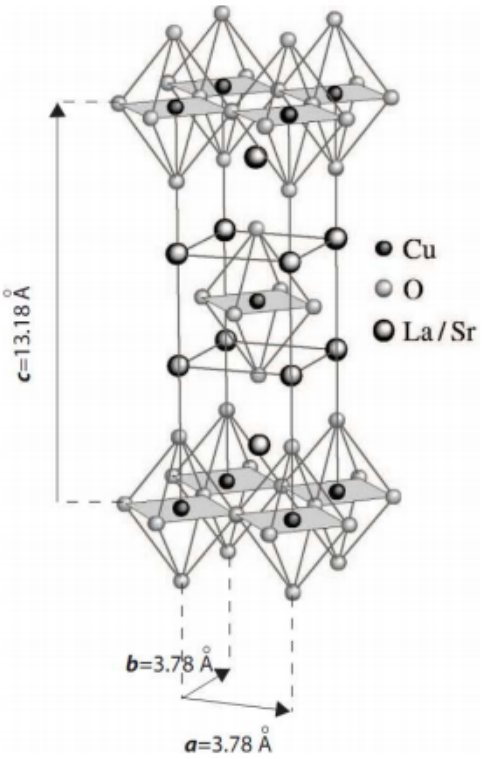

Figure 1.1: LSCO unit cell (7).

metal phase and resistivity is linear in T. This strange-metal phase exists also at lower doping for $T > T_c$. Another interesting phase is the Pseudogap phase starting below T^* and above T_c in the under doped regime. More phases are present in different doping and temperatures, such as stripes phase, spin-glass phase, and spin-density-wave phase. Further explanation of the different phases is given in the next subsections. Figure. 1.2 shows a cuprate phase diagram (not specific for LSCO).

1.1.1 Antiferromagnetism

In this phase, the spin $\frac{1}{2}$ of the Cu^{+2} ions is parallel to the CuO_2 plane and points towards one of its next nearest neighbor Cu^{+2} ion, and in the opposite direction from all of its nearest neighbors. Weak perpendicular (c direction) ferromagnetic moment in the CuO_2 planes is also formed. But, the ferromagnetic moment of neighboring planes is in the opposite direction, making the system a 3D antiferromagnet (5). The Heisenberg model with antisymmetric exchange interaction provide good microscopic explanation of the antiferromagnetic state (8). At $x \sim 0.02$, long range magnetic order is replaced by short range magnetic correlation which remain in the system up to $x \sim 0.07$.

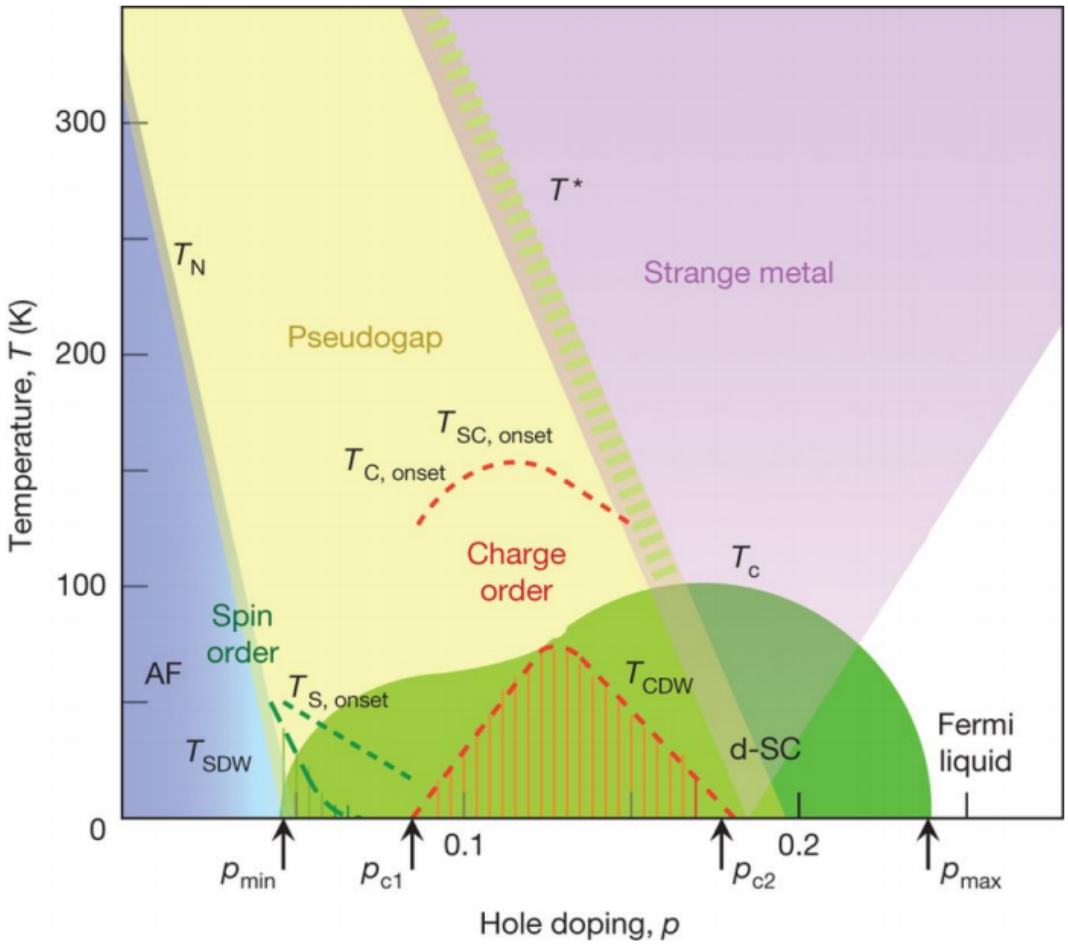

Figure 1.2: Cuprate phase diagram of hole doping x and temperature T (6).

1.1.2 Weak spin and charge order

At low temperature and doping of $0.02 < x < 0.15$, short range spin order or spin-density-wave forms in the system. Another type of short range order is a charge-density-wave, which usually forms at higher temperatures and dopings then the spin-density-wave. When charge-density-wave and spin-density-wave coexist, they are called strip order. Their presence at relatively high temperature near $x = 0.125$ (the 1/8 anomaly) where T_c is suppressed, suggest that stripe mode competes with SC.

1.1.3 Superconductivity

The SC phase is characterized by zero resistance and perfect diamagnetism. When applying magnetic field to a SC it will reject it by creating supercurrents which screen the external magnetic field. If we increase the external field, the supercurrents will also increase. Although the field is expelled from the bulk, it penetrates along the edges, and decaying exponentially with a characteristic length known as the penetration depth λ. Another important length scale that characterizes a SC is the coherence length ξ and it is common to think of ξ as the size of a Cooper-pair. SC materials can be divided into

two types depending on the ratio of ξ and λ. Type-I SC has $\lambda \ll \xi$ and type-II SC has $\lambda \gg \xi$. A type-I SC will hold the magnetic field outside until a critical field H_c is reached. Above H_c, the material "gives-up" and transforms back to the normal state letting all the magnetic flux penetrate. Type-II SC will stay field-free up to some critical field H_{c1}. For higher fields, it is capable of letting some of the magnetic flux penetrate as a vortex accommodating one flux-quanta Φ_0. The core of the vortex will be in the normal state phase, but outside of the vortex, the material will remain SC. When we increase the external field, more vortices will penetrate until they cover the entire material and it becomes normal throughout a second critical field H_{c2}. Cuprates have relatively large λ, which is about two orders of magnitude bigger than ξ, making them a strong type-II SC. The strong anisotropy dominates their SC properties. λ and ξ have different properties in the a and b directions (in plane) than in the c direction (between planes). This anisotropy will be discussed further in Sec. 1.2.

1.1.4 Fermi-liquid

In the overdoped regime ($x > 0.26$) at low enough temperature cuprates exhibit anisotropic metallic properties where resistivity ρ has T^2 dependence on temperature (but different between intra-plane and inter-plane). This behavior can be explained by the anisotropic Fermi-liquid theory. The elementary excitations of the Fermi-liquid phase are quasiparticles and quasiholes, with energy close to the Fermi energy. These quasiparticles are "dressed" by virtual excitations of particles and holes, but have the same charge and spin as bare particles. The interactions between quasiparticles are weaker than the electrons coulomb interaction. They can still scatter off each other, but have a relatively long lifetime τ. We can estimate their scattering rate near the Fermi momentum k_f from Fermi's golden rule and find that $\tau \propto (\bar{k} - k_f)^2 \equiv \delta k^2$,where $\bar{k}$ is the momenta of a thermal-excitation. The significant collisions outlying τ lies in a thermal neighborhood of the Fermi surface and so the relative momenta of low-temperature-excitation is $\delta k \sim K_B T$. The relation between resistivity and τ is: $\rho \sim (m/ne^2\tau)\Delta$ (where Δ is a fractional Umklapp scattering (9)), providing T^2 dependence between resistivity and temperature. A more careful calculation shows that electron-electron scattering alone is not enough to explain the T^2 dependence and another process of electron-phonon scattering (Umklapp (10)) must be taken into account.

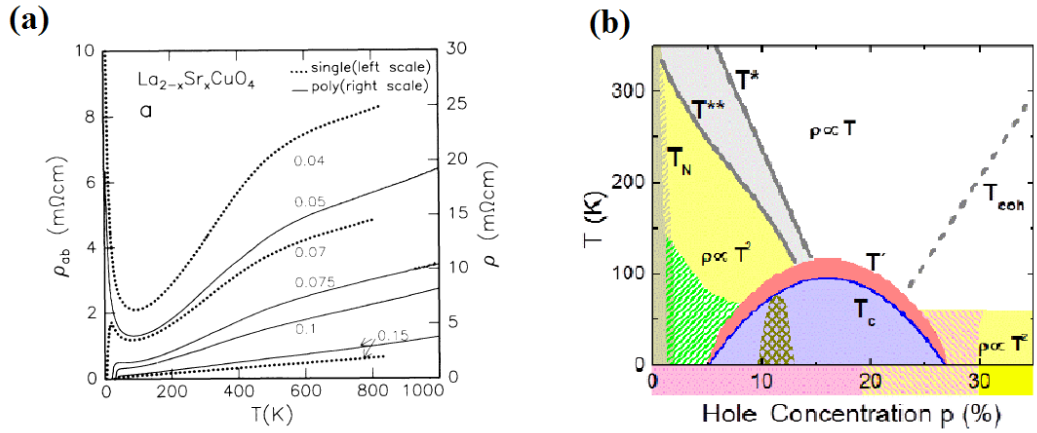

Figure 1.3: (a) The resistivity T-dependence for different doping of underdoped LSCO. The linear T-dependence last to lower temperatures for higher doping before it becomes quadratic. At low enough temperatures one can see the transition to SC for higher dopings or antiferromagnet for lower doping (Taken from: (12)). (b) Phase diagram of cuprates showing the psudogap regime below T^* and the different resistivity T-dependence regimes (Taken from: (11)). More regimes like, antiferromagnet below T_N (light brown), SC below T_c (purple), SC fluctuations between T' and T_c (red), and spin-glass regime (green), are shown. T_{coh} corresponds to the loss of antinodal quasiparticle coherence.

1.1.5 Strange metal and the pseudogap

The strange-metal phase is characterizes by linear dependence of the resistivity in temperature, contrary to the Fermi-liquid phase. Within the strange-metal phase, another anomaly occurs below a certain temperature - T^*. Angle resolved photo emission spectroscopy shows that an energy gap opens (primarily) in the antinodal direction in momentum-space, on the edges of the Brillouin-zone. When the temperature decreases, this so called psseudogap starts spreading along the Fermi arc towards the nodal direction and when another temperature T^{**} is crossed, the linear-T dependence of ρ is replaced again with the Fermi-liquid's T^2 relation (11),(12). When T_c is crossed, the SC gap opens all around the Fermi arcs apart from the nodal point. The relation between the SC gap Δ and the pseudogap Δ^* is a debateful subject. Figures 1.3 (a) and (b) shows the different T-dependence of ρ and a phase diagram (including T^* and T^{**}) respectively.

1.2 Anisotropy

The c-vector of the unit-cell is about three times larger than the a- and b-vectors, making the system highly anisotropic. This anisotropy is observed in many different experiments such as in-plane/out-of-plane resistivity (13) (14), parallel/perpendicular susceptibility (15), anisotropy of the upper critical fields (16), Stiffness measurements (1), and more. It is reasonable to assume that this anisotropy plays a key role in the origin of ΔT_c.

1.2.1 Structural anisotropy

Except for the in-plane/out-of-plane anisotropy, the system can be anisotropic inside the planes. When the a and b-vectors are equal, the unit cell is tetragonal, and when a, and b are not equal the unit cell is orthorhombic. This symmetry depends on doping and temperature (and also pressure). At high temperatures, the system is tetragonal. But at low doping and below a certain temperature, the system becomes orthorhombic. This doping-dependent temperature of the structural phase transition tetragonal $\rightarrow$ orthorhombic (often denoted by T_0) decreases with doping and reaches 0 at $x \sim 0.22$ (4). This in-plane anisotropy can influence the coupling between layers and the in-plane/out-of-plane anisotropy.

1.2.2 Anisotropy in resistivity measurements

The usual way to measure the in-plane/out-of-plane resistivity is by cutting two bars (or plates) with different orientations from the same single crystal and use the four-contact technique. The current flows from one end of the bar to the other while the voltage difference is measured between the ends. In one bar the CuO_2 planes are perpendicular to the current direction and the inter-plane resistivity ρ_c is measured. In the second bar the CuO_2 planes are parallel to the current direction and the intra-plane resistivity ρ_{ab} is measured. ρ_c is always larger than ρ_{ab} and the ratio ρ_c/ρ_{ab} is usually about $\sim 10^3$. In the work by S. Komiya et al. (13) on underdoped LSCO it was found that ρ_{ab}'s T-dependence changes smoothly with doping for $0.02 < x < 0.17$, while ρ_c's behavior changes when crossing to the SC doping regime ($0.07 > x$). Another work by G.S. Boebinger et al. (14) used high magnetic fields (~ 61 T) to suppress SC and measure the normal-state resistivity inside the SC dome near optimally doping of LSCO. Metallic state is defined by $\frac{d\rho}{dT} > 0$ and insulating state by $\frac{d\rho}{dT} < 0$. At low doping both ρ_{ab} and ρ_c are insulating and slightly above optimal doping, they are both metallic, but the insulator-to-metal crossover occurs at different doping/temperature as shown in Fig. 1.4. The different behavior of $\frac{d\rho}{dT}$ is another signature of the strong anisotropy. Other resistivity measurements (17) with strong magnetic field perpendicular to the CuO_2 planes showed strong decoupling between the planes while the in-plane coupling was unaffected.

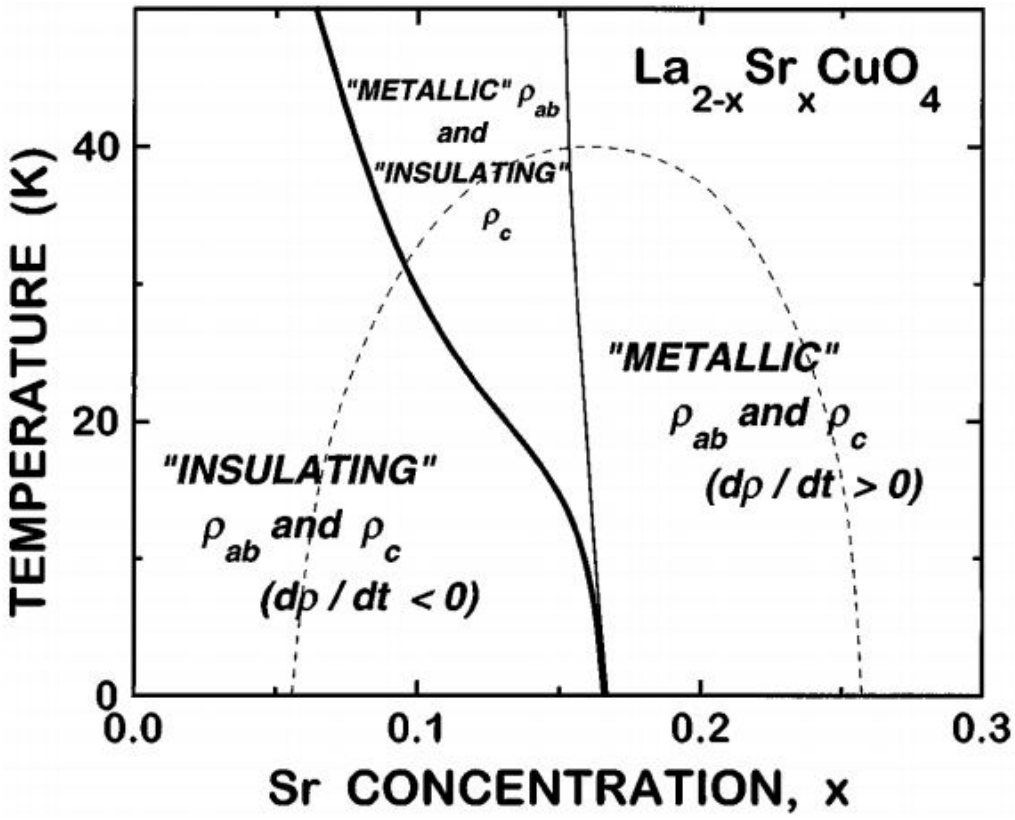

Figure 1.4: Normal state insulator-to-metal crossover of in-plane/out-of-plane resistivity, ρ_{ab} and ρ_c inside the SC dome (SC is suppressed by a magnetic field of ~ 61 T) (14).

1.2.3 Anisotropy in magnetization measurements

When cooling a SC sample below T_c and applying a magnetic field, the sample generates a magnetic moment to repel the external field (Meissner effect). Then, by heating the system while measuring the magnetic moment, one can measure T_c. By cutting needle-shaped samples from the same single crystal with the CuO_2 planes parallel/perpendicular to the needle's axis and measuring T_c, G. Drachuk et al. (15) found different T_c between the two needles. Such difference in T_c is another demonstration of cuprats anisotropy.

1.2.4 Anisotropy in stiffness measurements

Using a Stiffnessometer, I. Kapon measured (1) the difference in T_c for in-plane and out-of-plane currents. The measurement is done in equilibrium, detects only macroscopically phase coherent SC state, and avoids local SC fluctuations. A 0.64 K difference was found in $x = 0.125$ LSCO, and in my Msc-thesis I measured more samples of different doping with the same technique and again, observed ΔT_c.

Chapter 2

Research Methods

Most of the technical details of the system and data analysis are embedded in the articles themselves. In this section, the focus will be on crystal growth, sample preparation, and coil making. I will also introduce the Stiffnessometer, our main tool in this research.

2.1 Making $La_{2-x}Sr_xCuO_4$ samples

All samples are made in our lab from scratch. The chemical elements are mixed, pressed and molded into a single crystal. The crystalline orientation is determent by x-ray Laue diffraction and two plates are cut from the same crystal, but with different orientation. A diamond disc saw is used to cut the crystal into plates. Ring-shape samples are cut from the plates using a femto-second laser. The different stages of the growth and cutting are explained in this section.

2.1.1 Single crystal growth

The process starts by mixing CuO, La_2O_3, and $SrCO_3$ of the right amounts for the desired doping. At least four cycles of mixing and sintering are done until we get a uniform homogeneous powder, checked by x-ray powder-diffraction. The powder is pressed to a rod with 55000 PSI and sintered again at 1050 c° for 24 hours. Then, we use a traveling solvent floating zone (TSFZ) furnace to transform the rods of pressed powder in to single crystal. One rod (called feed) is hung over another shorter rod (called seed) and they rotate in different directions at 15 tpm. The edges of the rods (bottom of the feed and top of the seed) are melted with a set of four 300 W lamps and parabolic mirrors, inside

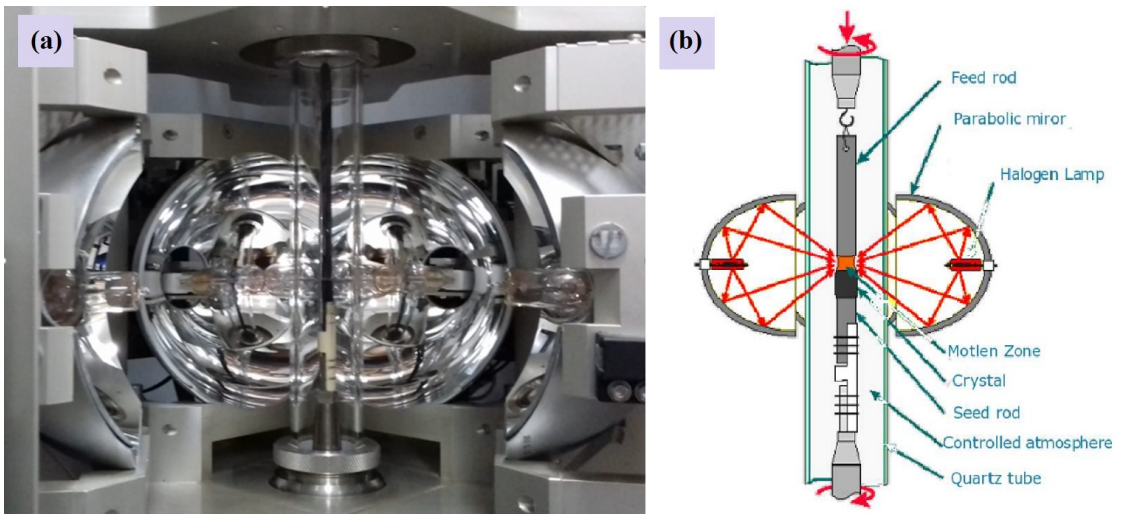

Figure 2.1: (a) Photograph of the feed and seed rods, the lamps and mirrors, and the quartz tube. (b) Schematic of the feed and seed rods, the lamps and mirrors, and the quartz tube.

a sealed quartz tube filled with argon and a small amount of oxygen gas, at a pressure of 5.5 bar.

After the initial melting of the tips of the rods we get a zone of molten solvent of LSCO and is mixed by the rods rotation. Then the stage with the lamps and mirrors is lifted slowly along the feed rod to melt it. When the hot zone moves up, the lower part of it solidifies, and if everything is right, it will also crystallized on the seed rod. The stage movement starts at 5.0 mm/h in the beginning of the growth and the rate is lowered to 1.0 mm/h and stay so during the stable growth of the single crystal.

The TSFZ furnace is shown in figure. 2.1. After the growth is finished, the crystal is annealed at a temperature of 850 C for 120 hours in an argon environment. The quality and orientation of the crystal is determined using Laue x-ray diffraction. To grow a high quality single crystal we optimized all parameters of the process (8).

2.1.2 Crystal orientation and rings cutting

The crystals are cut into two kinds of plates: plates with the copper-oxide layers parallel to the plane and plates with the copper-oxide layers perpendicular to the plane. From these plates we cut rings with tetragonal cross section using a femto-second-laser (at the Tel Aviv University Center for Nanoscience and Nanotechnology). We refer to the rings with the copper-oxide layers perpendicular/parallel to the symmetry axis of the ring as, c-ring and a-ring respectively. The rings go through another annealing process before they are measured. The LSCO rings have an inner diameter (ID) of $1.0 - 2.0$ mm, an outer diameter (OD) of $2.4 - 3.0$ mm, and height of ~ 1.0 mm. In Chap. 5 the rings are cut

again to change their cross-section.

2.2 Stiffnessometer

The superconducting stiffness $\hat{\rho_s}$ is defined by a local relation between the superconducting current density $\mathbf{j}_s$ to the vector potential (VP) $\mathbf{A}$ and the gradient of φ (the phase of the complex order parameter $\psi = |\psi|e^{i\varphi}$ [1]). This relation is:

$$\mathbf{j}_s = \hat{\rho_s}(\frac{\Phi_0}{2\pi}\boldsymbol{\nabla}\varphi - \mathbf{A}). \tag{2.1}$$

where Φ_0 is the magnetic flux quanta and $\hat{\rho_s}$ is a diagonal tensor. This equation is gauge invariant and when setting $\boldsymbol{\nabla}\varphi = 0$, we recover the London equation:

$$\mathbf{j}_s = -\hat{\rho_s}\mathbf{A}. \tag{2.2}$$

If we use the curl of Maxwell's equation: $\boldsymbol{\nabla} \times \boldsymbol{\nabla} \times \mathbf{B} = \mu_0 \boldsymbol{\nabla} \times \mathbf{J}$ (where $\mathbf{J}$ is the sum of normal, and super currents) and the definition of $\mathbf{A}$: $\mathbf{B} = \boldsymbol{\nabla} \times \mathbf{A}$, we get a partial differential equation for the magnetic field B: $\boldsymbol{\nabla}^2\mathbf{B} = \mu_0\hat{\rho_s}\mathbf{B}$. The solution (in one dimension) is: $B = B_0 e^{-x\lambda}$. This exponential decay of the magnetic field inside the bulk of a SC is called the Meissner effect and it gives us the relation between the SC stiffness $\hat{\rho_s}$ and the penetration depth λ:

$$\hat{\rho_s} = \frac{1}{\mu_0\lambda^2}. \tag{2.3}$$

The ideal Stiffnessometer is made of an infinitely long inner excitation coil (EC) piercing a ring-shaped sample. When applying current I through this EC a magnetic field is generated inside the coil with zero field outside. Nevertheless, outside of the coil there is a vector potential $\mathbf{A} = \mu_0\frac{nI}{r}\hat{\varphi}$ where n is the winding linear-density of the EC and r is the distance from the coil's symmetry axis.

If we cool the sample below T_c without any magnetic field or current in the excitation coil, there will be no VP. This cooling process is called: Zero-Gauge-Field-Cooling (ZGFC). When a sample is cooled and becomes a SC, the phase φ is chosen to be such that minimizes the free energy. So following the ZGFC protocol, $\boldsymbol{\nabla}\varphi = 0$, and $j_s = 0$. But now, changes of

[1] From the Ginsburg-Landau (GL) point of view, the system is a macroscopic quantum state, defined by a complex order parameter: $\psi = |\psi|e^{i\phi}$, where $|\psi|^2$ is the super-fluid density and φ is the phase.

φ is energetically costly for the SC, because it means breaking the coherence of the system and overcoming some energy barrier. So when we turn on the current in the coil and $\mathbf{A} \neq 0$ we generate supercurrents $\mathbf{j}_s$ inside the ring following London's equation (Eq. 2.2): $\mathbf{j}_s = -\rho_s \mathbf{A}$. These supercurrents running around in a loop create a magnetic moment m which can be measured using a pickup-loop connected to a superconducting quantum interference device (SQUID)[2].

The London equation introduces a linear relation between $\mathbf{j}_s$ and $\boldsymbol{A}$. Since $\boldsymbol{A}$ is proportional to the current in the excitation coil I and $\mathbf{j}_s$ is proportional to the sample's magnetic moment m, we get a linear relation between the applied current and the measured signal. When this linearity breaks, the system is said to be out of the "linear regime", because the critical current j_c was crossed somewhere within the sample. This process is more complicated and will depend on the geometry of the EC and the ring as explained in 2.2.4. There are two types of measurements we can do: We can stay at a constant fix temperature and increase the current I; this type of measurement determines the critical magnetic flux of the ring Φ_c from which we can extract ξ. Alternatively, we can change the temperature while the current is in the linear regime and constant; this type of measurement provides the ρ_s. When the signal of the ring disappears completely, it means there is no more persistent currant in the ring and we find T_c. But, different phenomena can influence the apparent T_cv (Correlated disorder can blunt the transition and create a "tail", and the finite size of the sample will also play a role in T_c). This is the main topic of chapter 5.

This technique is used to determine ρ_s without any leads or magnetic field. Another advantage of this technique is that it demands a global phase coherence. Therefore, phase transitions are much sharper compared to other techniques such as electric transport or magnetization measurements. Using the Stiffnessometer, we can measure T_c with great accuracy and study the stiffness close to the phase transition. Therefore, it's an ideal tool to measure ΔT_c.

The critical flux measurements (to measure ξ) can be done close to T_c where j_c is small, or well blow T_c (at $T \sim 1.7$ K), where we can use SC coils and apply high currents. When I is increased, the magnetic flux inside the coil increases and the ratio dependence on the geometry of the EC. To maximize the magnetic flux-to-current ratio (Φ_{ec}/I), we use EC with many layers which require rings with a proper geometry: The ring's inner

[2]Based on the Josephson junction effect, SQUIDs are commonly used to detect magnetic moment.

radius should be big enough for the many-layered EC, but the outer radius must be small (thin wall of about ~ 0.35 mm), making the ring very fragile and hard to manufacture. The outer radius needs to be small, because $j_c \propto r_{out}^2$ and will be explained in the data analysis Sec. 2.2.4.

2.2.1 Principle of operation

During the measurements, the ring is fixed at the center of the excitation coil and together they move along the z direction (the horizontal axis in Fig. 2.2), in and out of a gradiometer (of second order) which is fixed at $z = 0$ (z-scan procedure). The gradiometer serves as a pickup-loop that increase the signal and cancels noises. When they move, the magnetic flux through the gradiometer changes and the SQUID measures the change. The output signal from the SQUID is in voltage and proportinal to the magnetic flux through the gradiometer at each z. Figure 2.2 presents such measurements of a LSCO ring above and below T_c. Since the coil is finite, its magnetic signal is detected by the gradiometer and a combined signal of the coil and the ring is measured. The coil's signal can be measured above T_c (or without the ring), and subtracted from the combined signal, revealing the ring's signal. The difference between the maximum and the minimum of the ring's signal is labeled ΔV_{sc} and the difference between the maximum and the minimum of the excitation coil's signal is labeled ΔV_{ec}. The measurable parameters ΔV_{sc} and ΔV_{ec} are proportional to the magnetic flux generated by the ring and coil respectively, and their ratio (ΔV_{ratio}) can be translated to the stiffness (as explained in Sec. 2.2.4).

2.2.2 Experimental setup

The Stiffnessometer was developed as an add-on to S600 SQUID SUSCEPTOMETER of CRYOGENIC LTD and was adopted to the new Quantum Design MPMS3. Schematics of the setup is shown in Fig. 2.3. The excitation coil used in chap 3 and 5 is 60 mm long, with an external diameter is 0.8 mm. The coil is made of copper wire and has 2 layers of winding (1940 winding turns in total). The excitation coil used in chap 4 is 60 mm long, with an external diameter is 1.95 mm. The coil is made of a SC $TiNb$ wire and has 8 layers of winding (4800 winding turns in total). The gradiometer is made of 8 (4 in the QD MPMS3) pickup-loops to reduce noises with a long wavelength. A geometric factor G converts the coil's and ring's VP ratio on a single pickup-look $A_{sc}(R_{pl})/A_{ec}(R_{pl})$ to the voltage

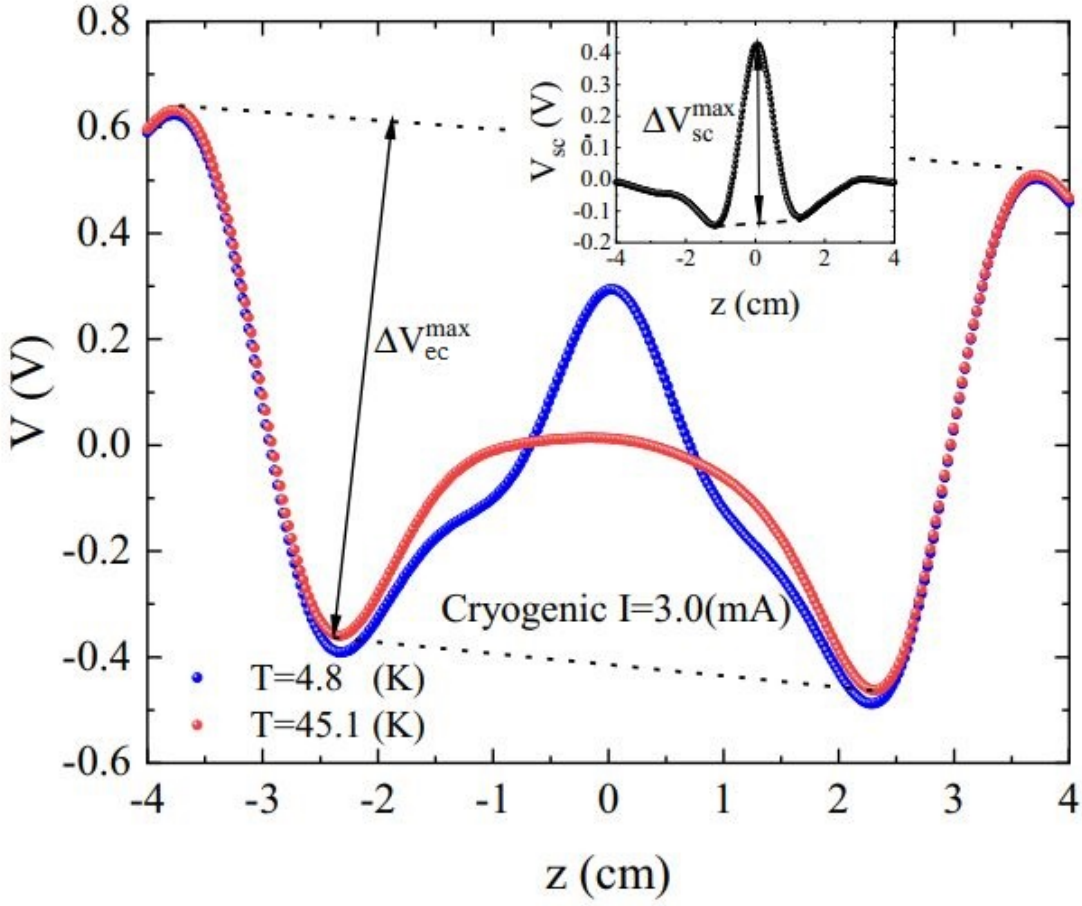

Figure 2.2: Raw data. SQUID signal for a LSCO $x = 0.17$ c-ring at high temperature (red), when the ring is not superconducting and at low temperature (blue) when the ring is superconducting. The inset shows the difference between these measurements. Subtracting the high temperature signal from the low temperature signal reviles the superconducting ring's signal. The difference between the maximum and the minimum of the ring's signal is labeled ΔV_{sc} and the difference between the maximum and the minimum of the coil's signal is labeled ΔV_{ec}.

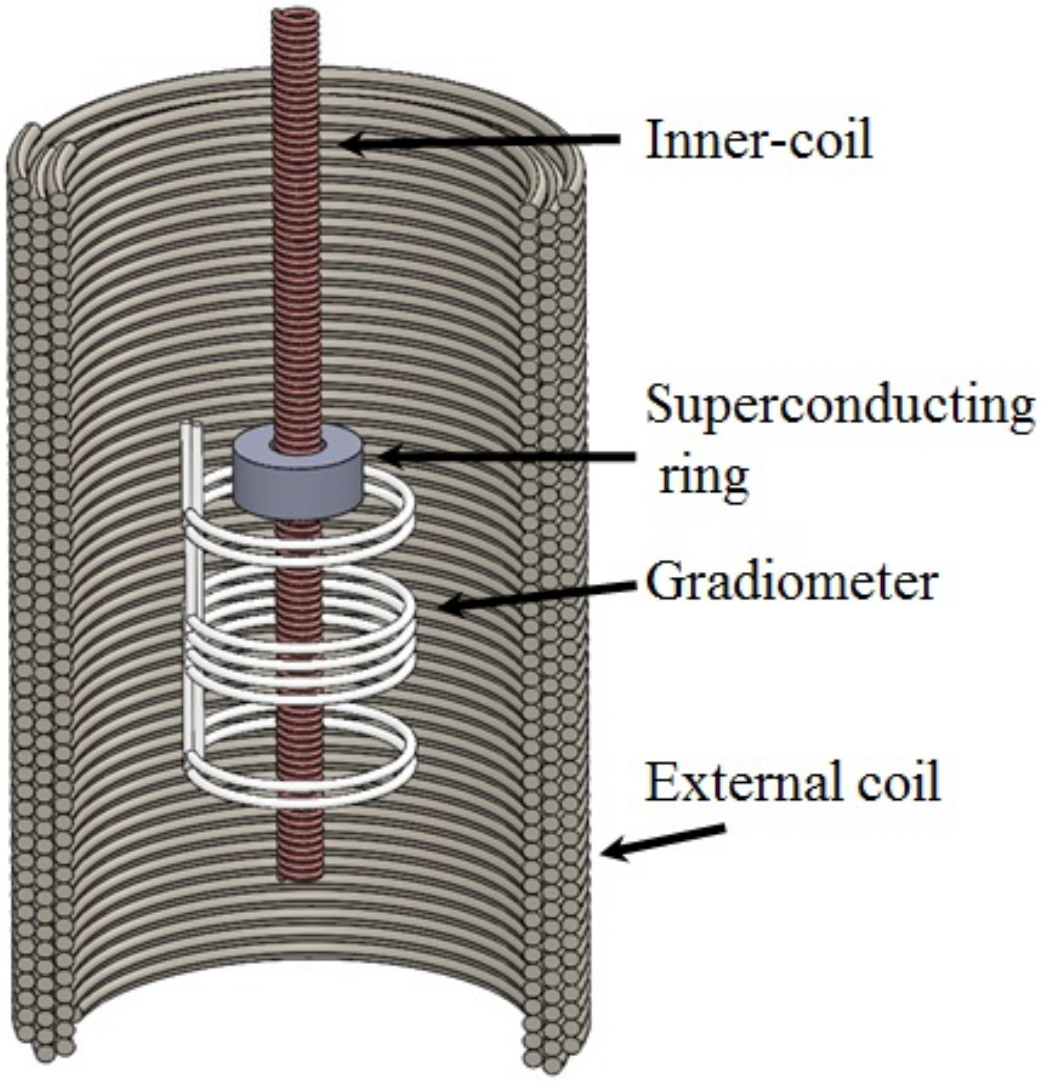

Figure 2.3: Schematics of Stiffnessometer and gradiometer. Illustration of the long excitation coil (inner-coil) with the SC ring on it, the gradiometer, and the external coil.

difference ratio measured by the gradiometer $\Delta V_{sc}(Gradiometer)/\Delta V_{ec}(Gradiometer)$. Where R_{pl} is the radius of the pickup-loop, A_{sc}, A_{ec} are the ring, and coil's VP respectively. G is calculated numerically (but can also be evaluated experimentally) and is ~ 3.62 and ~ 3.07 for Cryogenic and MPMS3 magnetometers, respectively. Another external coil is used to cancel external magnetic fields stronger than 0.001 Oe.

2.2.3 Coil fabrication

The heart of the Stiffnessometer is the excitation coil. The process of coil winding is also done in our lab to fit our needs. The coil winding must be neat to prevent leakage of magnetic field outside of the coil. Figure 2.4 (a) shows different coils, and Fig. 2.4 (b) depicts a zoom in on the winding. The coil's core is made of thin Nitinol wire covered

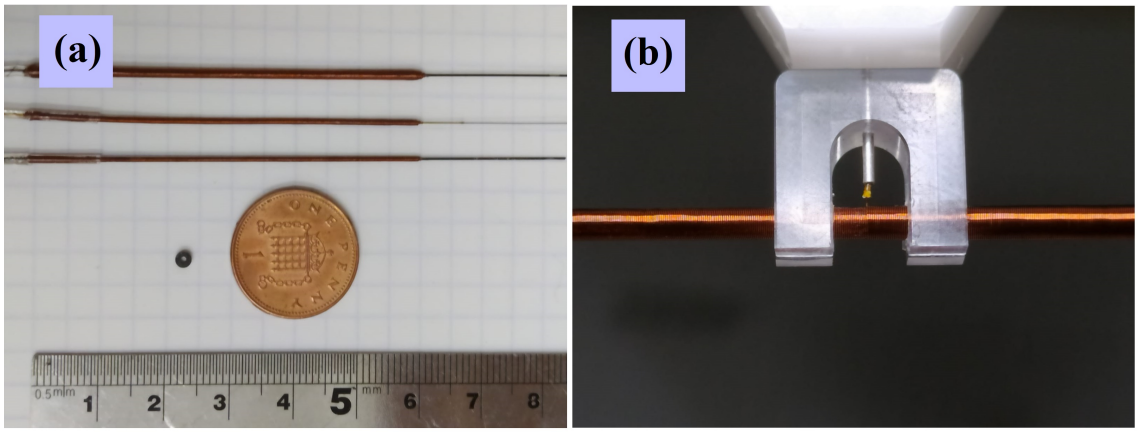

Figure 2.4: (a) Tree different coils made in our lab, a LSCO ring, and a penny for comparison. (b) Close look on a coil.

with polyamide coating. We use wires of different materials and thickness for different experiments. SC wires are used to make SC-coils for measurements with high currents at low temperatures, allowing us to measure the coherence length ξ in the ground state of the system.

2.2.4 Data analysis

When the temperature approaches T_c, λ starts to grow (compared to the ring's dimensions) and we must take into account the ring's self-inductance VP (assuming that $|\psi|$ is uniform). When the total VP inside the ring is $A_t = A_{sc} + A_{ec}$, combining Faraday's and London's equations, we obtain a partial differential equation (PDE) for A_{sc}:

$$\boldsymbol{\nabla}^2 \mathbf{A}_{sc} = \hat{\rho}_s \left(\frac{\Psi_{ec}}{2\pi r}\hat{\varphi} + \mathbf{A}_{sc}\right). \tag{2.4}$$

Changing to unitless parameters (scaling lengths by R_{pl} (the pickup-loop's radius) and $\mathbf{A}_{sc}(r)$ by $\mathbf{A}_{ec}(R_{pl})$) and working with cylindrical coordinates, Eq. 2.4 becomes:

$$\frac{\partial^2 A}{\partial z^2} + \frac{\partial^2 A}{\partial r^2} + \frac{1}{r}\frac{\partial A}{\partial r} - \frac{A}{r^2} = \frac{1}{\lambda^2}\left(A + \frac{1}{r}\right) \tag{2.5}$$

The numerical solution of the PDE is presented in Fig. 2.5, and one can see that the Stiffnessometer sensitivity is limited to the range where there is no saturation in $(R_{pl}/\lambda)^2$ (sensitivity range of $10^{-2} < \lambda < 10^{1}$ mm). At temperatures too close to T_c, the critical current j_c is low and limits the validity range of the Stiffnessometer to a tighter range of $0.1 < \lambda < 1.0$ mm.

To deal with the brake of linearity at the critical flux, we consider the spatial depen-

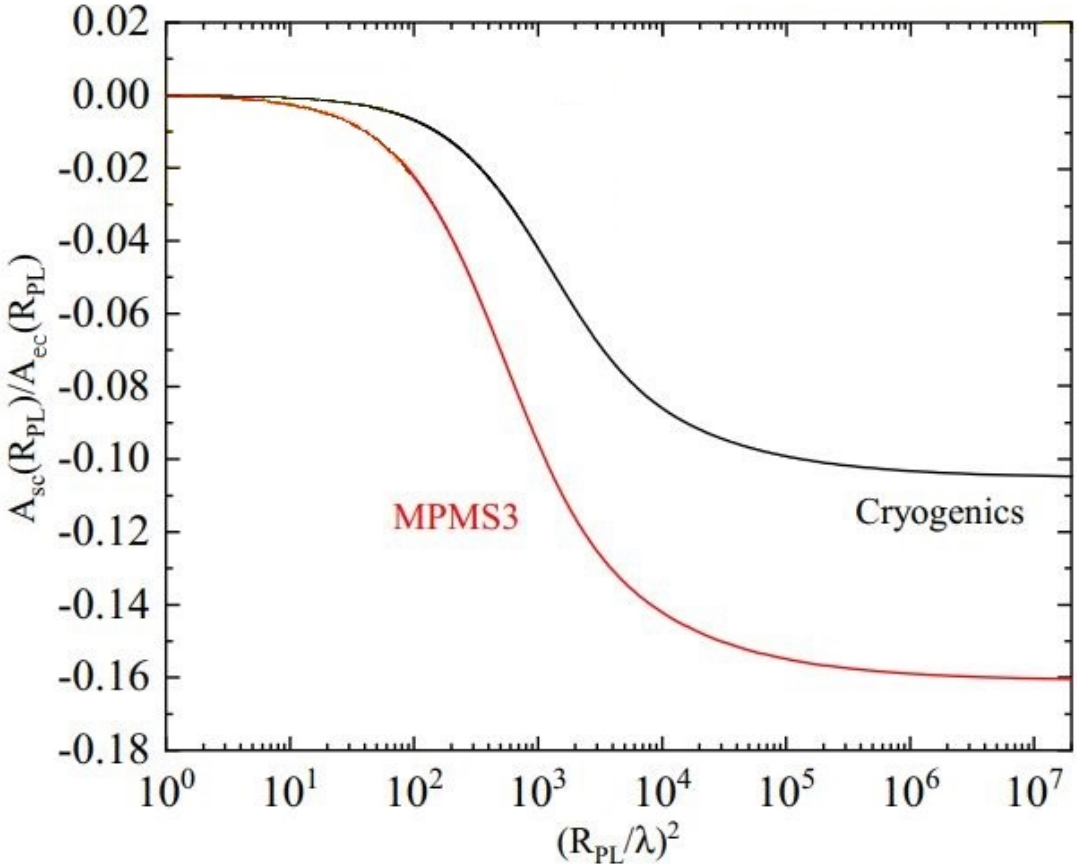

Figure 2.5: A semi-log plot of the numerical solution of the PDE (Eq. 2.5), evaluated at the pickup-loop radius, for different values of $(R_{pl}/\lambda)^2$. The pickup-loop radius R_{pl} is 13 mm and 8.5 mm in the Cryogenics and the MPMS3 respectively. The solution depends on the ring's dimensions too: ID = 1.0 mm, OD = 2.5 mm, h = 1.0 mm.

dence of the order parameter's amplitude ($|\psi|(r)$) by solving the two Ginzburg-Landau equations simultaneously. This was done by N. Gavish, O. Kenneth and A. Keren (22) for a hollow long cylinder. The solution of the two equations show that there is a critical magnetic flux (inside the excitation coil) given by:

$$\Phi_{ec}^{c} \lesssim \frac{\Phi_0 r_{out}^2}{\sqrt{8}\xi\lambda}. \tag{2.6}$$

Where r_{out} is the outer radius of the SC ring. Using this relation and λ (from stiffness measurement of other sources) we can extract the coherence length ξ from measurements of Φ_{ec}^{c}.

On Chap. 5 we focus on the measurements of the transition temperature. We define it as the temperature where the extrapolation of the sharp part of the transition meets zero when we measure the moment (or ΔV_{ring}) vs temperature. This temperature was independent of the initial current in the EC. The reason we are not looking at the point where the moment is indistinguishable from the noise is because inter layer disorder can manifest in a tail above the bulk transition temperature which is what we are interested

in.

2.3 Verification of the Stiffnessometer

As befitting a new technique, there are many tests needed to confirm it. We wanted to confirm that our assumption of an infinite coil is valid in our detection limits. Next, we wanted to validate the London equation Eq. 2.2 and the full equation of the super current Eq. 2.1. The theoretical dependence of the critical flux to the OD, ξ, and λ also needed to be tested. Last, we needed to check the finite size effect on the transition temperature. All those tests were done and are also explained in the body of the work: Chap 3, Chap 4, and Chap 5.

2.3.1 Infinite coil validation

Simulations of a finite coil with our parameters shows the external field outside the coil is about 0.3% of the field in its center and that the VP is similar to that of an infinite coil Fig. 3.2. The most direct test was measuring an open ring and see if the current in the EC influence the ring's signal. The open ring had no detectable signal Fig. 3.4. Another way to measure leakage of magnetic field was with a SQUID on chip that can scan the surface of the ring when the EC is On and OFF. The vortex number was not increased after turning on the EC (23).

2.3.2 Gauge field cooling process

The London equation states, that j_s is linear to the VP, so the measured moment should also be linear with the current of the EC. This linear relation is observed in the experiments Fig. 3.6. To demonstrate Eq. 2.1, we cooled the system below T_c while the excitation coil is on (current flows in the excitation coil), meaning: $\boldsymbol{A} \neq 0$. When we measured (z-scan[3]) while the excitation coil is still on, only the coil's signal was detected. This is because $\boldsymbol{\nabla}\varphi = \frac{2\pi}{\Phi_0}\boldsymbol{A}$ (up to a fraction of Φ_0) resulting in $\boldsymbol{j}_s = 0$. When we turn-off the excitation coil, $\boldsymbol{A} = 0$, but $\boldsymbol{\nabla}\varphi \neq 0$, and $\mathbf{j}_s = \hat{\rho_s}(\frac{\Phi_0}{2\pi}\boldsymbol{\nabla}\varphi)$; when measuring again, only the ring's signal is present. This cooling process is called gauge field cooling (GFC) and the ring's signal and phase transition are identical to what we get when following the ZGFC process.

[3]Moving the coil with/without the ring through the gradiometer and read the SQUID's output.

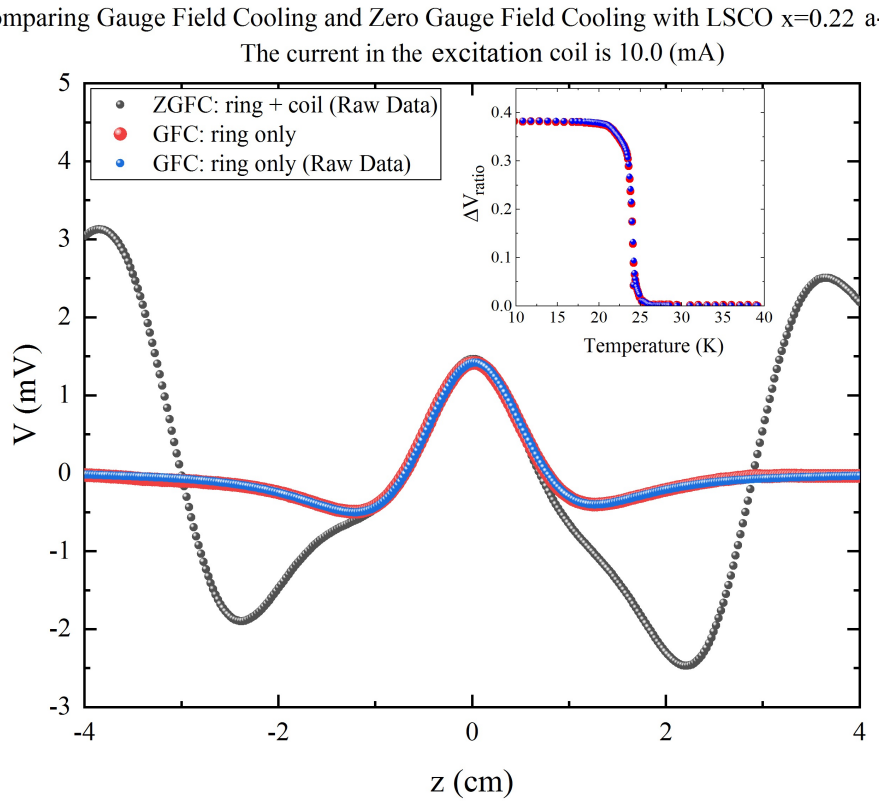

Figure 2.6: Raw signal of measurement after gauge field cooling (GFC) process, and after zero gauge field cooling (ZGFC) process and subtraction of the coil's signal. The inset shows stiffness measurements (ΔV_{ratio}) of the two protocols. Both in the raw signal and the stiffness measurements, the two different protocols give similar results. The red markers and the blue markers are similar but not identical (each one belongs to a different measurement and follow a different protocol).

This experiment is another verification that the field outside of the coil is insignificant. Figure 2.6 shows the measurements of both GFC and ZGFC protocols.

2.3.3 Critical magnetic flux verification

Equation 2.6 raises two size-relating issues: First, it is constructed for an infinite cylinder and not for a ring (flat cylinder). Second, it suggests that Φ_c depends only on the outer radius. Therefore, it was also important to check the size effect on Φ_c. This was done by measuring Niobium (Nb) rings (with known ξ, and λ) with different height or inner/outer diameter. These experiments where part of Chap. 4 and the results confirm the theory.

2.3.4 Finite size effect verification

It was suggested that the apparent T_c of the a-ring is reduced because close to T_c the inter-layer coupling is weak and the system behave as a 1D Josephson array and the inter-layer stiffness $\rho^{\perp}$ have exponential dependence on temperature and the cross section of the ring. To examine this interpretation, we measured the change of T_c, as a function of

the ring's cross-section. This was done by polishing the ring (changing its height) and by cutting the outer diameter of the ring (using again the femto-second-laser). This test was a big part of the work and is the focus of Chap. 5. The cross section was found to have significant influence over the inter-plane stiffness.

Chapter 3

Stiffnessometer: A magnetic-field-free superconducting stiffness meter and its application

Itay Mangel[1], Itzik Kapon[1], Nitzan Blau[1], Katrine Golubkov[1], Nir Gavish[2] and Amit Keren[1]

[1]*Department of Physics, Technion-Israel Institute of Technology, Haifa, 3200003, Israel*

[2]*Department of Mathematics, Technion-Israel Institute of Technology, Haifa, 3200003, Israel*

Published in PHYSICAL REVIEW B 102, 024502 (2020)

ABSTRACT

We provide a detailed account for a method to measure superconducting stiffness ρ_s, critical current density j_c, and coherence length ξ, in one apparatus, without subjecting the sample to magnetic field or attaching leads. The method is based on the London equation $\mathbf{j} = -\rho_s \mathbf{A}$, where $\mathbf{j}$ is the current density and $\mathbf{A}$ is the vector potential. Using a rotor free $\mathbf{A}$ and a measurement of $\mathbf{j}$ via the magnetic moment of a superconducting ring, we determine ρ_s. By increasing $\mathbf{A}$ until the London equation fails we determine j_c and

ξ. The method is sensitive to very small stiffness, which translates to penetration depth $\lambda \lesssim 1$ mm. It is also sensitive to low critical current density $j_c \sim 10^3$ Amm^{-2} or long coherence length $\xi \sim 1$ μm. Naturally the method does not suffer from demagnetization factor complications, the presence of vortices, or out-of-equilibrium conditions. Therefore, the absolute values of the different parameters can be determined. We demonstrate the application of this method to $La_{2-x}Sr_xCuO_4$ with $x = 0.17$.

3.1 Introduction

Superconducting stiffness ρ_s is defined via the gauge invariant relation between the current density $\mathbf{j}$, the vector potential $\mathbf{A}$, and the complex order parameter $\Psi = \psi(\mathbf{r})e^{i\phi(\mathbf{r})}$, with $\psi(\mathbf{r}) \geq 0$, according to

$$\mathbf{j} = \rho_s \left(\frac{\Phi_0}{2\pi} \nabla\phi - \mathbf{A} \right) \tag{3.1}$$

where Φ_0 is the superconducting flux quanta,

$$\rho_s = \frac{\psi^2 e^{*2}}{m^*}, \tag{3.2}$$

is known as the stiffness, and e^* and m^* are the carriers charge and mass respectively (1; 2; 3). ψ^2 is often interpreted as a measure of the superconducting carrier density with a maximum value ψ_0^2. When $\nabla\phi = 0$ the London equation

$$\mathbf{j} = -\rho_s \mathbf{A}. \tag{3.3}$$

is obtained. ρ_s can be expressed in units of length via

$$\rho_s = \frac{1}{\mu_0 \lambda^2}, \tag{3.4}$$

where λ is known as the penetration depth.

The two most important pieces of information on a superconductor (SC) are embedded in Eq. 3.1. First, ρ_s provides an indication on the ratio between carrier density and effective mass. For example, in high temperature superconductors (HTSC) the transition temperature T_c is found to be proportional to the stiffness at low temperatures. This finding, known as the Uemura plot, must play a key role in any theory of HTSC (4).

Second, the highest j for which the SC maintains $\nabla\phi = 0$ and thus the linear relation of Eq. 3.3 holds, sets the critical current j_c. j_c also has an interpretation in terms of coherence length via the shortest distance ξ on which ϕ can vary by 2π.

However, there is no direct way to measure ρ_s. The standard method is to apply magnetic field, to measure the penetration depth of the magnetic induction $\mathbf{B}$ into a material, and to use Eq. 3.4 to determine the stiffness (4; 5; 6; 7; 8; 9). However, the magnetic field raises issues one must consider: first, it is essential to take into account the sample shape via the concept of demagnetization factor. This factor is known exactly only for ellipsoidal samples, which are nearly impossible to come by. Second, magnetic fields introduce vortices, which can complicate the interpretation of the penetration depth measurements. Third, all methods have an inherent length scale window. The longest penetration depth that has been measured to the best of our knowledge is 10 μm (5; 6; 7; 8; 9). This is far shorter than a typical sample size. Therefore, there is a temperature range below T_c at which $\lambda > 10$ μm where the behavior of ρ_s is obscured. For highly anisotropic samples, this range could extend to temperatures well below T_c.

Similarly, there is no direct way to measure the critical current density j_c. The standard method is to connect leads, and to determine the current at which voltage develops across the sample (10; 11; 12; 13). However, this method could lead to two transitions: First when voltage develops and power, lower than the cooling power, is injected into the sample. Second a thermal runaway when the entire sample becomes normal and the voltage grows exponentially (11). Finally, stiffness and coherence length measurements require different experimental setups.

Here we present in detail an instrument to measure stiffness and coherence length simultaneously, in zero magnetic field and with no leads, based on the London equation (Eq. 3.3). This method determines ρ_s directly without the use of the penetration depth concept. When this equation breaks, and ρ_s can no longer be determined, it means the critical current has been reached. Consequently, we name the instrument stiffnessometer. We convert the breaking point of Eq. 3.3 to ξ using a mathematical solution of the full Ginzburg-Landau equations in the relevant setup (22). As we explain below, the stiffnessometer can measure very weak stiffness, which corresponds to λ ranging from tens of microns to millimeters. This allows measurements of stiffness closer to the critical temperature T_c than ever before, or measuring the stiffness of very anisotropic systems. Finally,

vortices or demagnetization factor are not a problem for the Stiffnessometer since the measurement is done in zero field. The stiffnessometer was previously used to measure the anisotropy of the stiffness in LSCO $x = 0.12$ (15), but only a brief account of the details of its operation was given.

3.2 Experimental setup

The method is based on the fact that outside an infinitely long coil (defining the $\hat{\mathbf{z}}$ direction), the magnetic field is zero while the vector potential is finite. This vector potential is tangential and points in the $\hat{\varphi}$ direction. When such an inner-coil is placed in the center of a SC ring, the vector potential leads to a current density in the ring according to Eq. 3.1. This current flows around the ring and generates a magnetic moment, which is detected by moving the ring and the inner-coil rigidly relative to a pickup-loop. The concept of the measurement is depicted in Fig. 3.1(a). A typical inner-coil and two superconducting rings of the cuprate SC $La_{2-x}Sr_xCuO_4$ (LSCO) are shown in Fig. 3.1(b). In Fig. 3.1(c) we present a zoom-in on three different coils with outer diameters of 2, 0.8, and 0.25 mm. They have 2 to 16 layers of wires with thickness between 10 and 100 μm, and their length is 60 mm. Our stiffnessometer is an add-on to a Cryogenic SQUID and to a quantum design MPMS3 magnetometers.

Both magnetometers use a second order gradiometer, rather than a single pickup loop. The gradiometer is made of three winding groups. The outer two are constructed from two loops each, wound clockwise, and the inner group is made of four loops, wound anticlockwise. This is also demonstrated in Fig 3.1(a). The gradiometer ensures that a magnetic moment generates voltage only when it is in the vicinity of the gradiometer center. Also, any field uniform in space gives zero signal even if it drifts in time. The gradiometer is connected to a superconducting quantum interference device (SQUID). The output voltage V of the device is proportional to the difference between flux threading the different loops of the gradiometer.

The vector potential outside of an infinitely long coil is given by

$$\mathbf{A}_{ic} = \frac{\Phi_{ic}}{2\pi r}\hat{\varphi}, \tag{3.5}$$

where r is the distance from the center of the coil, and Φ_{ic} is the flux produced by the

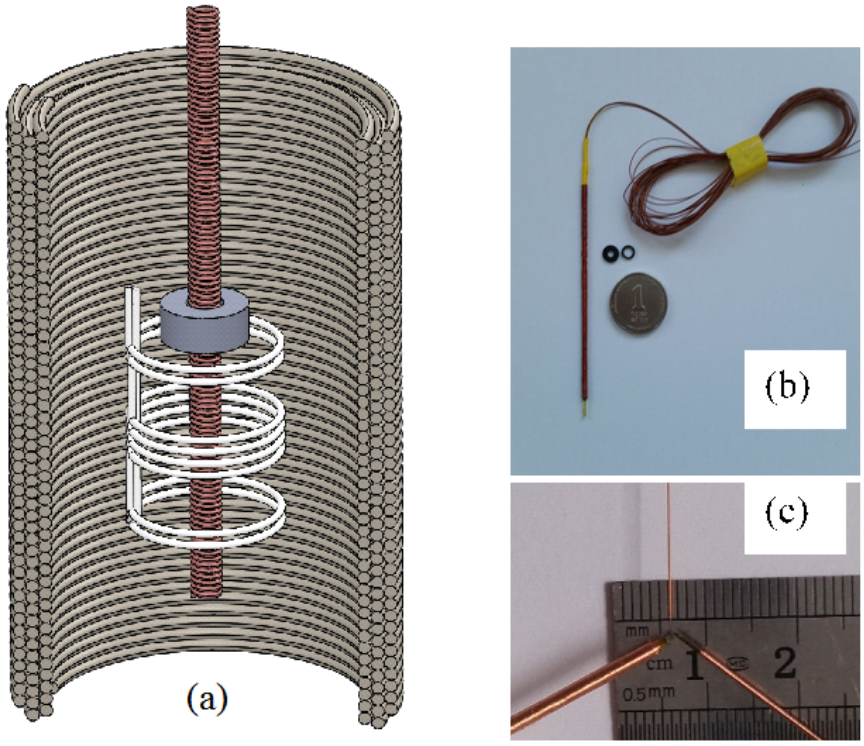

Figure 3.1: **Experimental setup.** (a) An illustration of the stiffnessometer: The superconducting ring is threaded by an inner coil, placed in the center of a gradiometer, and surrounded by a main coil that serves as a shim coil. (b) A typical inner coil, 60 mm long with 2 mm outer diameter. Also shown are two $La_{2-x}Sr_xCuO_4$ rings with a rectangular cross section. (c) A zoom-in on other inner coils with outer diameters ranging from 2.0 mm to 0.25 mm, and length of 60 mm.

inner coil. To check the validity of this expression in our case we calculated numerically the magnetic field B_z and vector potential A_φ (in the Coulomb gauge) produced by the inner coil as a function of r and z. This coil is 60 mm long, has an inner diameter (I.D.) of 0.54 mm, an outer diameter (O.D.) of 0.8 mm, 2 layers, and 1940 turns in total. The measured LSCO ring has an I.D. of 1.0 mm, an O.D. of 2.5 mm, and a height (h) of 1.0 mm. Fig. 3.2 shows the result of the calculations. The approximation of an infinite coil, presented by the dashed-doted green line, is perfect for our ring size and even for much larger rings. The calculation also shows that the strongest field just outside of the inner coil is 10^4 times smaller than the field at its center.

The sample is grown using an optical floating zone furnace. It is oriented using x-ray Laue camera and cut to plates and then into a ring shape using an ELAS master femtosecond laser cutter. The ring's plane is the CuO_2 plane of the sample. After cutting, the sample is annealed at 850 C° for 120 h in argon atmosphere.

The measurements are done in two different detection methods. (I) DC scan mode, where we record the SQUID's output voltage $V(z)$ while the relative distance between the gradiometer and the ring changes when the ring and inner coil move. The DC mode allows detection of the contribution from the inner coil as well, since the entire coil can be pulled out of the gradiometer. Our gradiometer detects magnetic moments within a range of 15 mm on each side of its center. This sets the length of our inner coils. When measuring over a wide temperature range, detection of the inner coil contribution is important in order to determine the flux it generates at each temperature. (II) VSM mode, where the ring vibrates around the center of the gradiometer. In this mode the coil does not contribute to the signal. The VSM mode is fast and allows fine temperature scans without the need to achieve temperature stability at each measuring point.

There is a risk that field generated in the inner coil leaks since no coil is infinitely long or perfect. To overcome this leak, a main coil, also shown in Fig. 3.1(a), acts as a shim to cancel the field on the ring when it is at the gradiometer center. In the Cryogenic SQUID the main coil has a field resolution of 0.1 μT. The ultralow field (ULF) capability of MPMS3 allows for field cancellation down to 0.3 μT. Therefore, we can keep the field on the ring as low as 0.1 μT when needed.

The measurements can be done in two different procedures: One is zero gauge field cooling (ZGFC) in which we cool the ring to a temperature below T_c, turn on the current

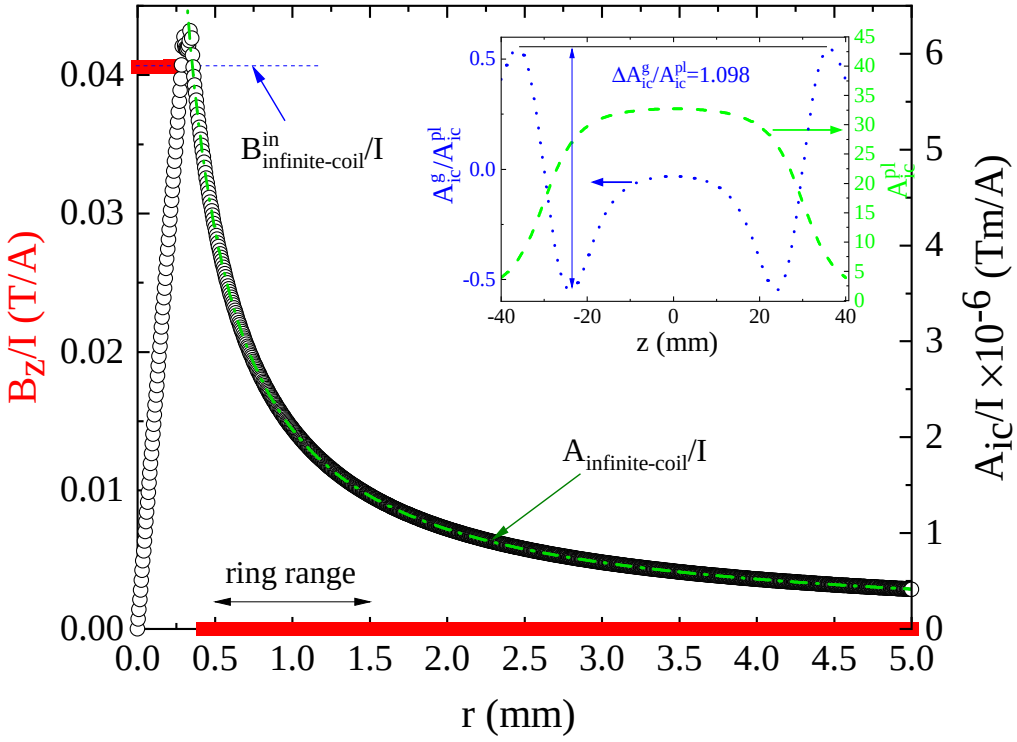

Figure 3.2: **Vector potential and magnetic field profile.** Numerical calculation of the vector potential and magnetic field per current at $z = 0$ for the inner coil used in this study. The coil parameters are: length $l = 60$ mm, inner diameter $= 0.54$ mm, outer diameter $= 0.8$ mm, 2 layers, and 1940 turns. The ring position relative to the inner coil center is demonstrated by the double arrows. The vector potential is very well approximated by an infinite coil over the range of the ring as the dashed-doted green line demonstrates. Inset: A^{pl}_{ic} and A^{g}_{ic}/A^{pl}_{ic} as a function of z, as explained in the main text.

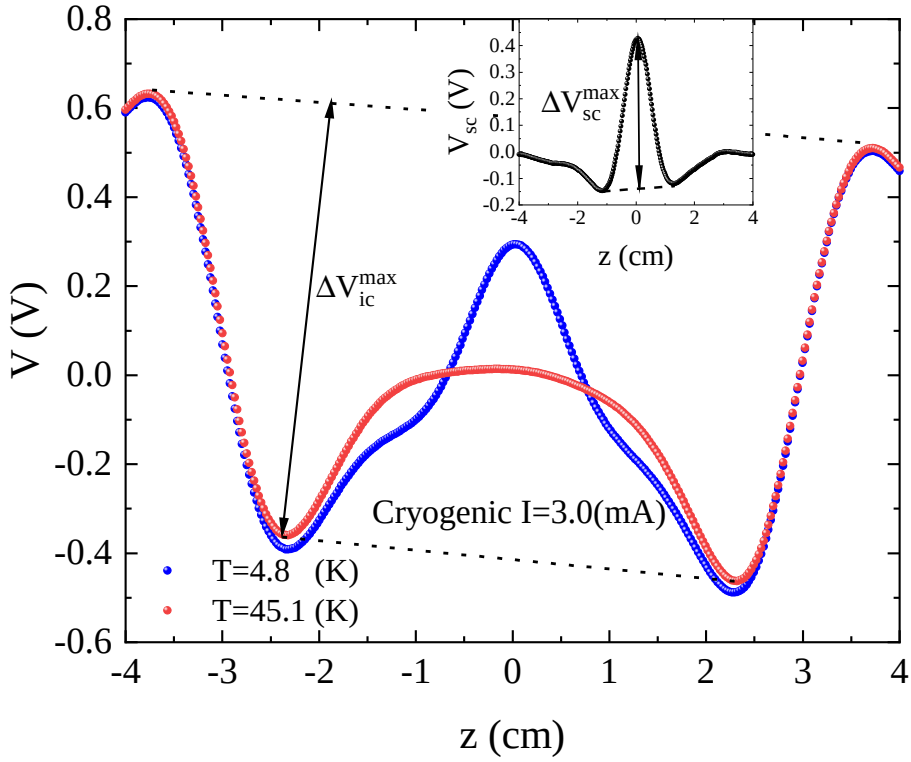

Figure 3.3: **Raw data.** SQUID signal for a LSCO $x = 0.17$ ring at high temperature, when the ring is not superconducting, and at low temperature when the ring is superconducting. The inset shows the difference between these measurements.

in the inner coil I when the ring is superconducting, and measure while warming. In this procedure, the SC minimizes its free energy by setting $\nabla\phi = 0$ in Eq. 3.1. This value of $\nabla\phi$ does not change as $\mathbf{A}$ is turned on, as long as the current in the coil is below some critical value (as explained later). In this case Eq. 3.3 holds throughout the measurements. The other procedure is gauge field cooling (GFC) in which we turn on the current in the inner-coil at a temperature above T_c, cool the inner coil and ring below T_c, and turn the current off. To minimize its free energy the SC sets $\nabla\phi$ in Eq. 3.1 such that j is as close to zero as possible. When $\mathbf{A}$ is turned off, $\nabla\phi$ does not change and plays the role of $\mathbf{A}$ in the ZGFC procedure.

To better appreciate why $\nabla\phi = 0$, even when A is ramped, one can view ϕ as the phase of an in-plane arrow. Cooling at $A = 0$ sets all the arrows pointing in the same direction. Since the phase is quantized, to change ϕ means a twist of all arrows in a closed loop, such that the phase between the first arrow and last one in the loop changes by 2π. This would lead to a discontinuity in the phase value, a procedure that costs energy, and generates instantaneous voltage according to the Josephson equation $\frac{\hbar}{e^*}\frac{\partial\phi}{\partial t}$. A nice analog is a ferromagnetic ring with the spins pointing in the same direction. Rotating the last

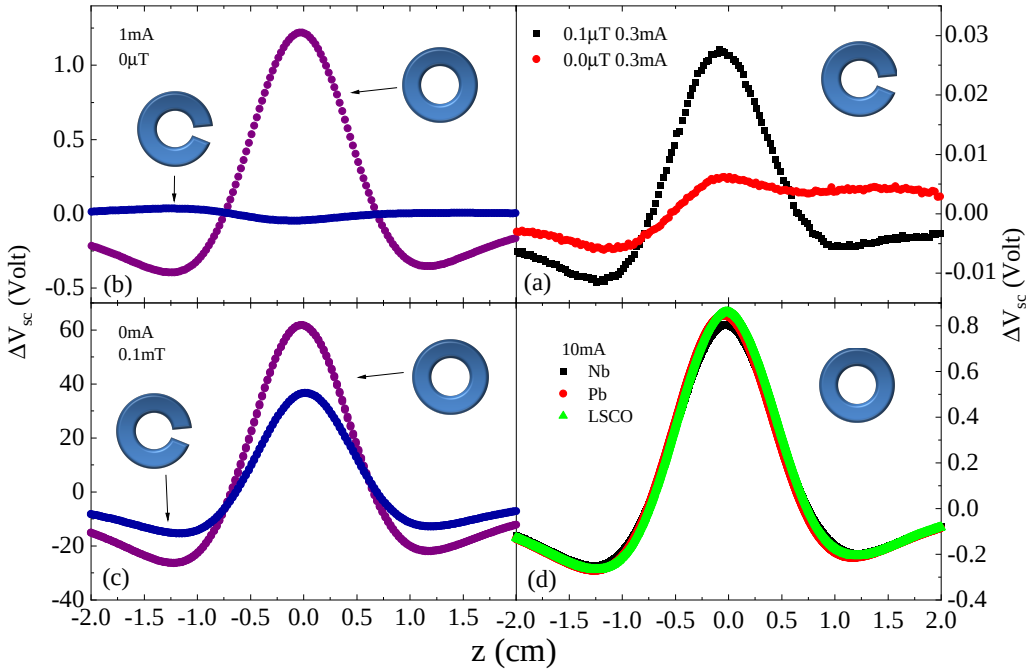

Figure 3.4: **Experimental tests.** (a) The signal with a current of 0.3 mA in the inner coil and 0.1 μT fields demonstrating the quality of the field canceling procedure. (b) The SQUID signal for open and closed rings when the field is zero and the vector potential is finite. (c) The SQUID signal for open and closed rings when the vector potential is zero but the field is finite. (d) Demonstrating that when λ is much smaller than the sample size the signal is material independent.

spin with respect to the first one by 2π requires us to break a bond. This procedure is not energetically favorable for a ferromagnet (or the SC ring). Therefore, ramping A leaves all arrows pointing in the same direction and $\nabla\phi = 0$, until A exceeds a critical value. At this point, the current is too high and it is worthwhile for the SC to "break a bond" and reduce the current.

A typical DC mode measurement is demonstrated in Fig. 3.3. The red symbols represent the signal when the entire inner coil has moved through the pickup coil at $T > T_c$. Before the lower end of the inner coil has reached the gradiometer, the flux through it is zero. During the time the lower end of the inner coil transverse the gradiometer its contribution to the total flux changes from zero to positive to negative and back to zero. The upper end of the inner coil has the opposite effect; its contribution to the flux goes from zero to negative to positive and back to zero. But there is a time (or distance) delay between the lower-end and upper-end contributions, leading to the observed signal. A linear drift of the voltage can be easily evaluated as demonstrated by the dotted lines. We define the inner-coil maximum voltage difference ΔV_{ic}^{max} as demonstrated in Fig. 3.3.

At $T < T_c$ the ring adds its own signal, as shown in Fig. 3.3 by blue symbols. The ring

produces current that generates opposite flux to the one in the inner coil. The ring signal is concentrated on a narrower range on the z axis. By subtracting the high temperature measurement from the low temperature one, it is possible to obtain the signal from the ring alone V_{sc} as demonstrated in the inset of Fig. 3.3. We define the maximum ring voltage difference ΔV_{sc}^{max} as shown in the inset. The ratio $\Delta V_{sc}^{max}/\Delta V_{ic}^{max}$ stores the information on the stiffness, as will be discussed in the Data Analysis Sec. 3.5.

3.3 Tests

To ensure that our signal is not due to leakage of magnetic field from the inner coil or any other field source, we perform three tests. In the first one we apply current in the inner coil, measure the field leakage at the ring position using an open ring, and cancel it using the main coil. Then we increase the field by only 0.1 μT. The measurements before and after the field increase are depicted in Fig. 3.4(a). They indicate that we can cancel the field in the ring position to better than 0.1 μT. Clearly in zero field there is no signal. In the second test we measure the stiffness (zero field and applied current in the inner coil) of closed and open rings, which are otherwise identical in size. The results are shown in Fig. 3.4(b). The signal from a closed ring is much bigger than the background from an open one. In Fig. 3.4(c) we repeat this measurement with an applied field in the main coil of 0.1 mT, and no current in the inner coil. In this case both open and closed rings give strong and similar signals. The difference between the two signals is consistent with the missing mass in the open ring. These tests confirm that the field leakage is not relevant to our stiffness measurement. Our ability to determine small stiffness depends on how well we can cancel the field at the ring position.

Another important test of the stiffnessometer comes from comparing the signal from rings of exactly the same dimensions, but made from different materials. At temperatures well below T_c the stiffness is expected to be strong, namely, the penetration depth should be much shorter than all the ring dimensions. In this case, as the current is turned on, and flux in the inner-coil Φ_{ic} changes, an electric field is generated in the SC ring E_{sc} according to

$$E_{sc} = \frac{1}{2\pi r}\frac{\partial \Phi_{ic}}{\partial t} = -\frac{\partial A_{sc}}{\partial t}$$

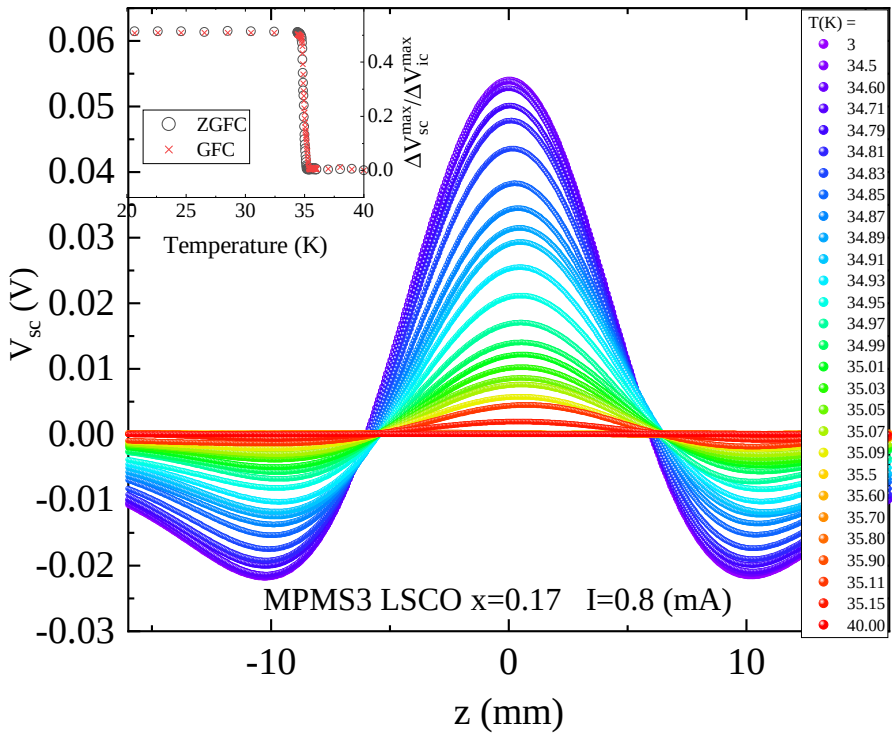

Figure 3.5: **Temperature dependence.** The SQUID signal V_{sc} for a $La_{2-x}Sr_xCuO_4$ $x = 0.17$ ring with the CuO_2 planes perpendicular to the ring symmetry axis, at different temperatures. The inset shows $\Delta V_{sc}^{max}/\Delta V_{ic}^{max}$ in the ZGFC and GFC procedures as a function of temperature.

where A_{sc} is the vector potential of the ring. This leads to

$$\Phi_{sc} = 2\pi r A_{sc} = -\Phi_{ic},$$

where Φ_{sc} is the flux generated by the SC ring at its center. In other words, when λ is short compared to the ring dimensions, the SC produces flux which exactly cancels the applied flux through it, regardless of the material used. Therefore, all materials should produce the same signal. This is demonstrated in Fig. 3.4(d) for niobium (Nb), lead (Pb), and LSCO. They all have the same ΔV_{sc}.

3.4 Measurements

In this section we present mainly stiffnessometer raw data out of which we are able to extract ρ_s, ξ, and j_c as a function of temperature in favorable conditions.

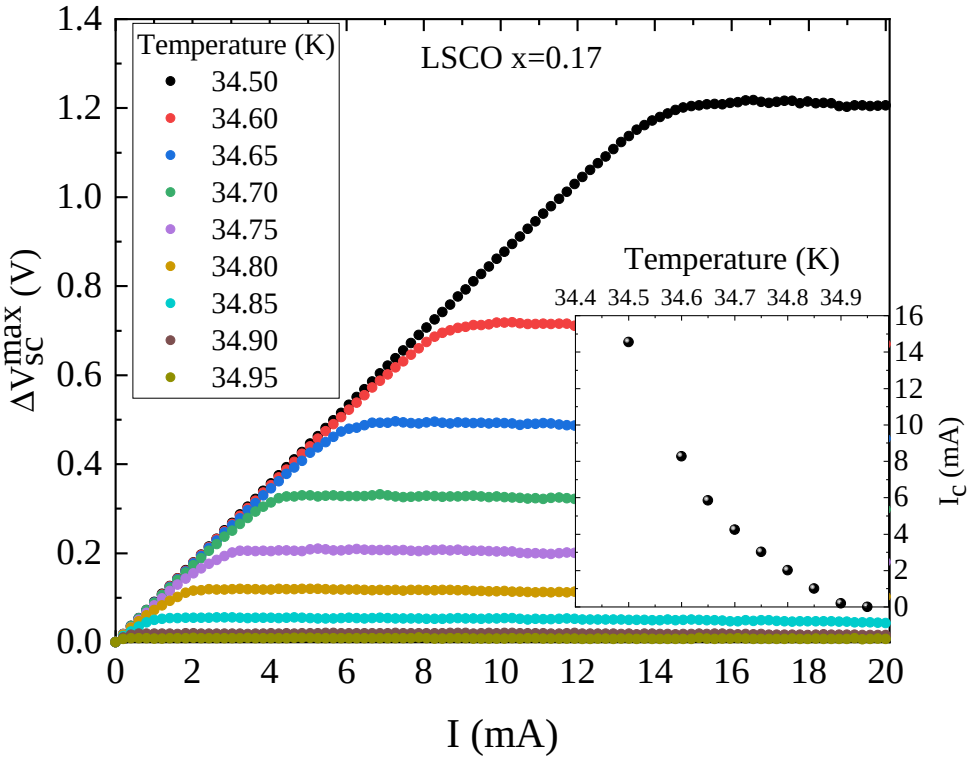

Figure 3.6: **Critical currents.** The SC ring signal ΔV_{sc}^{max} as a function of applied current in the inner-coil I, for different temperatures approaching T_c. The inset shows critical current I_c, where the signal becomes current independent, as a function of temperature.

3.4.1 Stiffness and its temperature dependence

In Fig. 3.5 we present the stiffnessometer signal evolution with temperature for the LSCO $x = 0.17$ ring as measured by the DC mode and ZGFC procedure with $I = 0.8$ mA. At temperatures between 3.0 and 34.7 K there is no change in the signal. But, between 34.7 K and $T_c = 35.53$ K the signal diminishes rapidly, as expected. The inset of Fig. 3.5 shows $\Delta V_{sc}^{max}/\Delta V_{ic}^{max}$ from both ZGFC and GFC measurement protocols. There is no difference between the two strategies.

3.4.2 Critical current and its temperature dependence

The stiffnessometer can also be used to measure critical currents. This is depicted in Fig. 3.6 for the LSCO ring at various temperatures. The signal from the ring ΔV_{sc}^{max} grows linearly with I at each T, but abruptly becomes I independent at a critical current $I_c(T)$, presented in the inset. It means that the SC can generate only a finite amount of opposing flux. Therefore, we are detecting j_c of the SC.

As I exceeds I_c, vortices start to flow into the center of the ring, so that j in the ring never exceeds j_c. In other words, once the critical current in the sample is crossed, $\nabla\phi$

is no longer zero and becomes $\nabla\phi = m/r$ with $m \neq 0$. The SC selects m such that j is fixed. Therefore, for $I > I_c$, the current in the ring and ΔV_{sc}^{max} are fixed.

3.5 Data analysis

Analyzing the stiffnessometer signal is done in steps: (A) we consider a single pickup loop and then a gradiometer. (B) The order parameter magnitude $|\Psi|$ is taken to be constant in space and the stiffness is weak. Weak stiffness means that the vector potential on the ring is only due to the applied current. The vector potential generated by the internal current of the ring is ignored. This approximation is valid when the ring's current density is smaller than j_c and the penetration length is longer than the sample dimensions. The weak stiffness analysis is analytical, and valid close (but not too close) to T_c. (C) The order parameter is still assumed to be constant in space but now the stiffness is strong. In this case, the self vector potential is taken into account. This leads to a partial differential equation (PDE), which we solve numerically with relatively simple means. (D) A full solution of the coupled Ginzburg-Landau equations allowing for both $|\Psi|$ and A to be space dependent. This level of analysis is required only when the SC is nearly destroyed by the internal currents, and it is good for extracting j_c and ξ. The case of a very tall hollow cylinder, is covered in Ref. (22). Consequently, at present we can only place limits on j_c and ξ.

3.5.1 Single pickuploop and gradiometer

Had we used a single pickup loop, the voltage would have been proportional to the flux threading it $\Phi = 2\pi R_{pl} A(R_{pl})$, where $R_{pl} = 13$ mm and $R_{pl} = 8.5$ mm for the Cryogenic and MPMS3 pickup loop radii, respectively. Above T_c, maximum voltage is achieved when the pickup loop is at the center of the inner coil so that $V_{ic}^{max} = k2\pi R_{pl} A_{ic}(R_{pl}, z = 0)$ where k is a proportionality constant. Similarly, a ring at the center of and parallel with a pickup loop would generate a maximum voltage proportional to its own flux, $V_{sc}^{max} = k2\pi R_{pl} A_{sc}(R_{pl}, z = 0)$, where A_{sc} is the vector potential generated by the ring. Therefore,

$$\frac{V_{sc}^{max}}{V_{ic}^{max}} = \frac{A_{sc}(R_{pl}, z = 0)}{A_{ic}(R_{pl}, z = 0)}. \tag{3.6}$$

Next, we convert between the signal detected by a gradiometer to the signal that would

have been detected by a single pickup loop. We find a conversion factor G from the vector potential evaluated on a single pickup-loop A^{pl} to the differences in the vector potential generated by the gradiometer ΔA^g. This has to be done for both the ring and the inner coil. The vector potential of a ring with magnetic moment $\mathfrak{m}$ on the pickup loop depends on the moment's height z from the plane of the loop according to $A = 2\pi\mathfrak{m}R_{pl}^2/(R_{pl}^2+z^2)^{\frac{3}{2}}$. Therefore, for a ring and our gradiometer

$$\frac{A_{sc}^g(R_{pl},z)}{A_{sc}^{pl}(R_{pl},z=0)} = \frac{-2R_{pl}^3}{(R_{pl}^2+(z+\Delta z_{pl})^2)^{\frac{3}{2}}} + \frac{4R_{pl}^3}{(R_{pl}^2+z^2)^{\frac{3}{2}}} + \\ + \frac{-2R_{pl}^3}{(R_{pl}^2+(z-\Delta z_{pl})^2)^{\frac{3}{2}}}, \quad (3.7)$$

where $\Delta z_{pl} = 7.0$ mm and $\Delta z_{pl} = 8.0$ mm is the separation between the different groups of gradiometer windings for Cryogenic and MPMS3 magnetometers, respectively. The difference between the maximum and minimum of this function is $\Delta A_{sc}^g/A_R^{pl} = 1.70$ and 3.37, again respectively, are the conversion factor for the ring.

To convert from A_{ic}^{pl} to ΔA_{ic}^g we plot by the green line in the inset of Fig. 3.2 the vector potential generated by our coil at R_{pl} as a function of z, $A_{ic}^{pl}(z)$. The plot is specific for $\Delta z_{pl} = 7.0$ mm. The function

$$\frac{A_{ic}^g(z)}{A_{ic}^{pl}} = \frac{-2A_{ic}^{pl}(z+\Delta z_{pl}) + 4A_{ic}^{pl}(z) - 2A_{ic}^{pl}(z-\Delta z_{pl})}{A_{ic}^{pl}(0)} \quad (3.8)$$

is also plotted in the inset by the blue line. The difference between the maximum and minimum of this function is the conversion factor for the inner coil. We find numerically that $\Delta A_{ic}^g/A_{ic}^{pl} = 0.47$. Thus

$$\frac{\Delta V_{sc}^{max}}{\Delta V_{ic}^{max}} = G\frac{A_{sc}^{pl}}{A_{ic}^{pl}} \quad (3.9)$$

with $G = 3.62$ and 3.07 for Cryogenic and MPMS3 magnetometers, respectively. By measuring $\Delta V_{sc}^{max}/\Delta V_{ic}^{max}$ one can predict the expected vector potential ratio between the coil and the ring at the pickup-loop position. As we show below, G could also be calibrated experimentally.

As for the VSM method, the magnetic moment $\mathfrak{m}$ of the ring and A_{sc}^{pl} are related by

$$\frac{\mathfrak{m}}{\Delta V_{ic}^{max}} = F\frac{A_{sc}^{pl}}{A_{ic}^{pl}} \quad (3.10)$$

where F is a calibration factor. In the GFC procedure ΔV_{ic}^{max} is measured before the

coil current is turned off. F is determined by measuring $\mathfrak{m}$, and calculating A_{sc}^{pl}/A_{ic}^{pl} in conditions that are not sensitive to the stiffness, as demonstrated in Sec. 3.3.

3.5.2 Weak stiffness, $|\psi(\mathbf{r})| = \psi_0$

The current from each ring element is $j(r)hdr$ where h is the ring height and dr is a ring element width. Using the London equation, the magnetic moment generated by each ring element is $d\mathfrak{m} = \frac{r\rho_s\Phi_{ic}h}{2c}dr$. Integrating from the inner to the outer radii yields the total moment of the ring $\mathfrak{m} = \frac{\rho_s\Phi_{ic}h}{4c}(r_{out}^2 - r_{in}^2)$, and

$$A_{sc} = \frac{\mathfrak{m}}{r^2} \tag{3.11}$$

Using Eq. 3.4, the penetration depth is given by

$$\lambda^2 = \frac{h(r_{out}^2 - r_{in}^2)}{8R_{pl}} \frac{A_{ic}(R_{pl})}{A_{sc}(R_{pl})}. \tag{3.12}$$

Since all the dimensions of the ring and pickup loop are on the order of 1 mm, and we can measure voltage ratios to better than 5%, we can measure λ on the order of 1 mm.

3.5.3 Strong stiffness, $|\psi(\mathbf{r})| = \psi_0$

In the strong stiffness case, the total vector potential experienced by the ring $\mathbf{A}_t$ is the sum of $\mathbf{A}_{ic}$ and $\mathbf{A}_{sc}$. Using Faraday's and London's equations, with $\mathbf{B} = \nabla \times \mathbf{A}$, and the transformation $\psi(\mathbf{r})/\psi_0 \to \psi(\mathbf{r})$, one finds that

$$\nabla^2 \mathbf{A}_{sc} = \frac{\psi^2(\mathbf{r})}{\lambda^2} \left(\frac{\Phi_{ic}}{2\pi r}\hat{\varphi} + \mathbf{A}_{sc} \right), \tag{3.13}$$

where $\psi(\mathbf{r}) = 1$ inside the SC and zero outside. The Coulomb gauge is built into Eq. 3.8 inside the ring since for any vector field $\mathbf{F}$, $\nabla \cdot \nabla \times \mathbf{F} = 0$. Outside of the ring this gauge has to be imposed separately. In cylindrical coordinates $\mathbf{A}_{sc} = A(z,r)\hat{\varphi}$, and with the coordinate transformation

$$\mathbf{r}/R_{pl} \to \mathbf{r}, \mathbf{A}_{sc}/A_{ic}(R_{pl}) \to \mathbf{A}, \lambda/R_{pl} \to \lambda \tag{3.14}$$

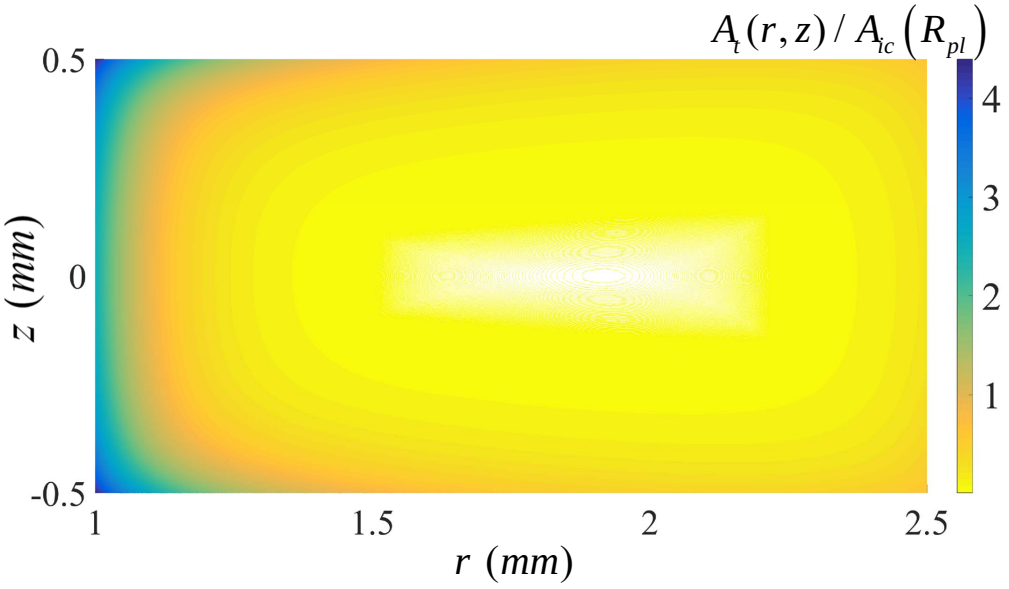

Figure 3.7: A_t **distribution inside the ring.** The total vector potential obtained from the solution of Eq. 3.15 and the vector potential of the inner-coil A_{ic}, as a function of r and z for $\lambda/R_{pl} = 0.1/13$, $r_{in} = 1$ mm, $r_{out} = 2.5$ mm, $h = 1$ mm.

the equation in the ring becomes

$$\frac{\partial^2 A}{\partial z^2} + \frac{\partial^2 A}{\partial r^2} + \frac{1}{r}\frac{\partial A}{\partial r} - \frac{A}{r^2} = \frac{\psi^2(\mathbf{r})}{\lambda^2}\left(A + \frac{1}{r}\right) \tag{3.15}$$

with r, z, and λ in units of R_{pl}, and A is in units of $A_{ic}(R_{pl})$. The solution of this equation, evaluated at R_{pl}, is the quantity one would measure with a single pickup loop as indicated in Eq. 3.6.

We solved Eq. 3.15 for different λ values and our LSCO ring parameters with both the COMSOL 5.2a and FREE-FEM (16) softwares. We used finite elements in a box $[-L_z, L_z] \times [0, L_r]$ where $L_z = L_r = 8$. Dirichlet boundary conditions are imposed at $z = \pm L_z$, $r = 0$, and $r = L_r$. Maximal mesh spacing is set to be $h = 0.01$ in the ring and its immediate vicinity, and $h = 0.25$ elsewhere. The total vector potential A_t for $\lambda/R_{pl} = 0.1/13$, and for all values of r and z in the ring cross section is presented in Fig. 3.7. Clearly the vector potential, hence the current, is strongest close to the inner radius of the ring. They decay towards the center of the ring. The solutions at $r = 1$ and $z = 0$ and our ring parameters, for a range of λ values, and different magnetometers, are presented in Fig. 3.8 on a semi-log plot. The inset is a zoom-in on the long λ region emphasized by a yellow rectangle. The solid line represents Eq. 3.12 again with our LSCO

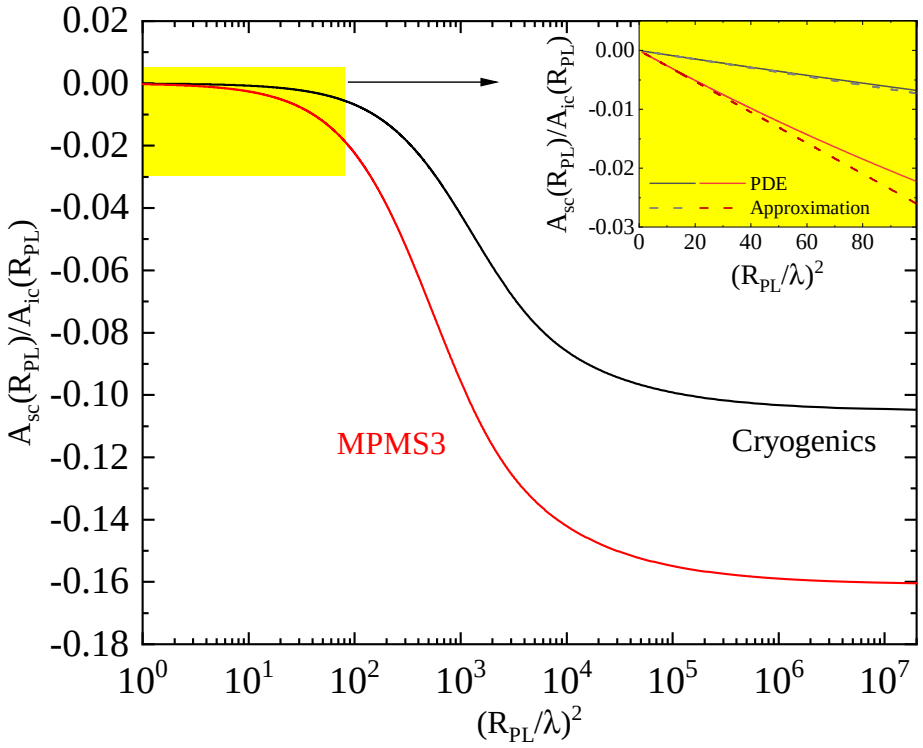

Figure 3.8: **Solution of the stiffnessometer PDE.** A semi-log plot of the solution of Eq. 3.15 evaluated at the pickup-coil radius, for different values of $(R_{pl}/\lambda)^2$. The inset shows the behavior for large λ. The solid line is given by Eq. 3.12.

ring parameters. There is a good agreement between the PDE solution at long λ and the weak-stiffness approximation.

In Fig. 3.8 we see that when the penetration depth is very short, $A_{sc}^{pl}/A_{ic}^{pl} = -0.16$ for the MPMS3. Multiplying the absolute value of this number by the MPMS3 $G = 3.07$ we expect a saturation value of $\Delta V_{sc}^{max}/\Delta V_{ic}^{max} = 0.49$. The measured value, however, is 0.516 as seen in the inset of Fig. 3.5. The calculated and experimental G factors are somewhat different. The experimental "G factor" is determined by dividing the measured saturation voltage ratios by the numerical saturation value. For the presented data of LSCO $x = 0.17$ this yields $G = 3.22$.

3.5.4 Ginzburg-Landau

When the current j somewhere in the SC is strong enough to destroy superconductivity, ψ becomes space dependent even inside the SC. One has to solve two Ginzburg-Landau equations simultaneously. Consider a hollow long cylinder. Using the transformation $2\pi R_{pl} A_{sc}/\Phi_0 \rightarrow A_{sc}$ and normalizing all lengths by R_{pl} these equations are given by

$$\frac{\partial^2 A_{sc}}{\partial r^2} + \frac{1}{r}\frac{\partial A_{sc}}{\partial r} - \frac{A_{sc}}{r^2} = \frac{\psi^2(r)}{\lambda^2}\left(A_{\rm sc} + \frac{J}{r}\right), \tag{3.16}$$

and

$$\xi^2\left(\frac{\partial^2\psi}{\partial r^2} + \frac{1}{r}\frac{\partial\psi}{\partial r}\right) = \psi^3 - \left(1 - \xi^2\left(A_{\rm sc} + \frac{J}{r}\right)^2\right)\psi. \tag{3.17}$$

The applied flux is now expressed explicitly in the equations by

$$J = \Phi_{ic}/\Phi_0, \tag{3.18}$$

and $A_{\rm sc}(0) = A_{\rm sc}(\infty) = 0$. For r inside the SC, $\psi(r) \geq 0$, outside $\psi(r) = 0$. The other boundary conditions are $\psi'(r_{\rm in}) = \psi'(r_{\rm out}) = 0$. The analysis of Eqs. 3.16 and 3.17 for the case $\xi \ll \lambda \ll 1$ is described in Ref. (22).

The emerging picture is that when J is small, the analysis of Sec. 3.5.3 is valid. Only for $J > r_{in}^2/\sqrt{8}\xi\lambda$, the order parameter's magnitude ψ begins to diminish in the inner rim of the cylinder and the cylinder's hole is effectively larger than r_{in}. Nevertheless, the SC still expels the flux of the inner coil and no critical point appears in $A_{sc}(R_{pl})$. The effective hole size r_{in}^{eff} increases with increasing J, until ψ survives only on a boundary layer of width λ at r_{out}. At even larger J, the SC is no longer able to expel the applied flux, A_{sc} does no longer grow with I, and vortices are expected to penetrate into the SC hole. These vortices are manifested in an increase of $\nabla\phi$. This behavior occurs at a folding point given by

$$J_{fold} \lesssim \frac{r_{out}^2}{\sqrt{8}\xi\lambda}. \tag{3.19}$$

The name "folding" means that increasing J past J_{fold} does not change the solution. The smaller ξ and λ, the better the approximation of J_{fold} is.

To evaluate the critical current j_c, we realize that when j is pushed to a boundary layer of width λ at r_{out}, it is still capable of expelling the inner-coil flux, but higher current will destroy SC completely. Therefore, $\Phi_{ic} = \mu_0 j_c \lambda \pi r_{out}^2$. Using Eqs. 3.18 and 3.19 we find

$$j_c \gtrsim \frac{\Phi_0}{\sqrt{8}\pi\mu_0\lambda^2\xi} \tag{3.20}$$

where now λ and ξ are in units of length.

Although Eq. 3.19 is derived for a tall cylinder, we anticipate that it is valid for our

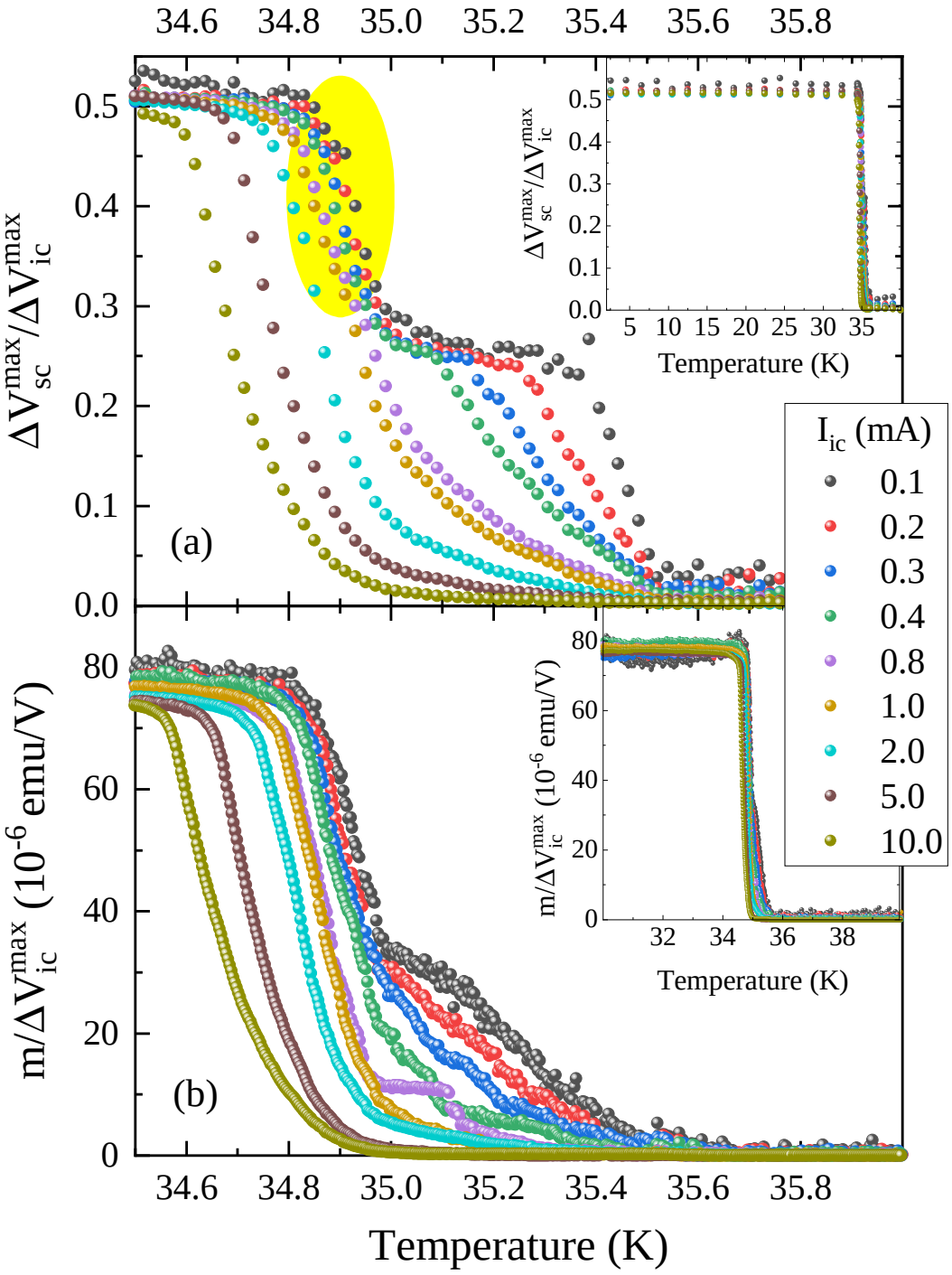

Figure 3.9: **Temperature dependence of normalized signals** (a) $\Delta V_{sc}^{max}/\Delta V_{ic}^{max}$ obtained by DC measurements (see Eq. 3.9) as a function of temperature close to the phase transition. The yellow shade is the region where the full Ginzburg-Landau analysis is valid. The inset is a zoom-out on the entire temperature range. (b) The magnetic moment normalized by the coil signal (see Eq. 3.10) obtained by VSM measurements. Again, the inset is a zoom-out on a broader temperature range.

ring. As long as λ is smaller than all dimensions of the ring, currents will flow on the boundaries of the "effective ring", as in Fig. 3.7 and will be strongest at the inner rim of the "effective ring", but with a J dependent r_{in}^{eff}. A change in behavior of the signal will take place only when $r_{in}^{eff} \simeq r_{out} - \lambda$ as in the cylinder case.

3.6 Results

Figure 3.9(a) depicts $\Delta V_{sc}^{max}/\Delta V_{ic}^{max}$ obtained by DC measurements. The signal is flat at low T and drops close to T_c. As the current decreases, the drop of the signal is postponed to higher temperatures. At currents below $I = 0.4$ mA a knee develops in the middle of the phase transition. Nevertheless, there is one $T_c = 35.53$ K for all currents. Isolated islands of SC with stronger stiffness cannot be the origin of these knees since only macroscopic closed lopes of SC can contribute to the signal. We speculate that these knees are related to SC surface states (17), with very small critical currents. In fact, knees were seen before in magnetization measurement on needle shaped LSCO, at very low fields, but they were not given much attention (9). The inset of Fig. 3.9(a) shows the full temperature range demonstrating that the normalized signal is independent of the applied coil current. In Fig. 3.9(b) we show the $\mathfrak{m}/\Delta V_{ic}^{max}$ data collected using the VSM method. Quantitatively, it looks the same as the DC measurement but less sharp and with few glitches of the signal. The knees disappear or smear and the uprise of the signal when cooling from T_c is less abrupt. The inset again demonstrates that at low temperature the magnetic moment is proportional to the applied current as is mirrored in ΔV_{ic}^{max}.

Using the measurements presented in Fig. 3.9(a), the experimentally determined conversion factor G, and the solution of Eq. 3.15 presented in Fig. 3.8, we extract the penetration depth as if the solution is valid for all temperatures. The extracted λ versus temperature with two applied currents $I = 0.8$ mA and $I = 0.2$ mA is depicted in Fig. 3.10 on a log scale. Ideally we would like to find the $I \to 0$ limit of λ. However, at low temperatures where the signal saturates, the determination of λ is noise. Close to T_c there is a major behavior change at low current due to the knee. Moreover, a full Ginzburg-Landau analysis requires $\lambda \ll R_{pl}$. This leaves a small window where we can properly analyze our data. This window is marked by a yellow circle in Fig. 3.9(a), and by yellow shade in Fig. 3.10. We zoom-in on the shaded area in the inset of Fig. 3.10 and show with arrows

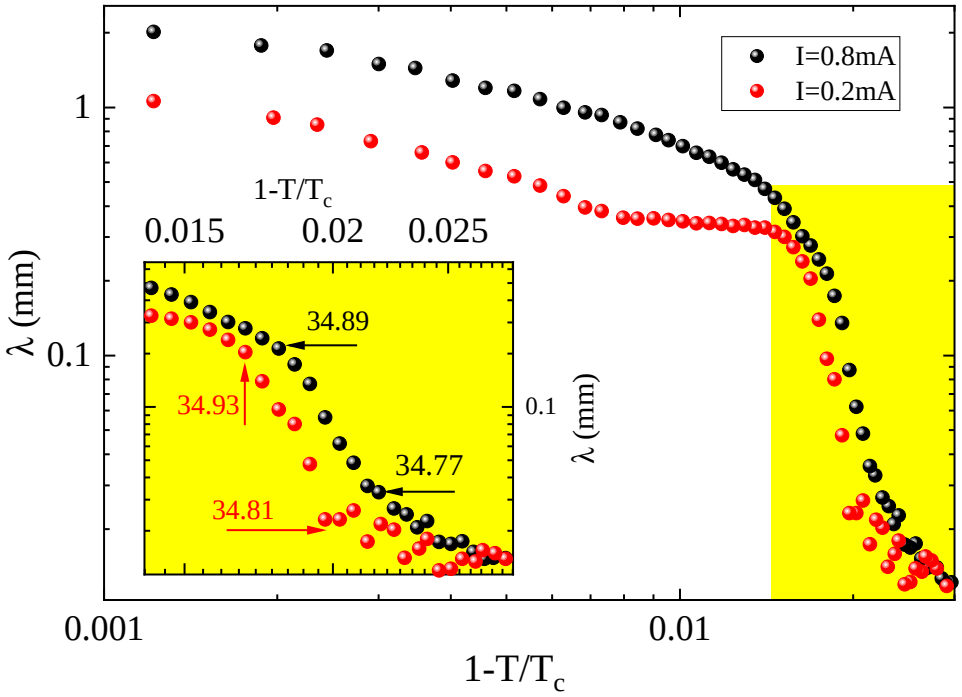

Figure 3.10: **Temperature dependence of the penetration depth.** λ extracted from the data of Fig. 3.9(a), based on Eq. 3.15, over the full temperature range. The inset arrows mark the λ's rang that meet all criteria required for full Ginzburg-Landau analysis.

the temperature range where our analysis is valid.

As for ξ and j_c; in Fig. 3.6 $\Delta V_{sc}^{max}(I)$ is measured at temperatures approaching T_c but before the knee. We identify I_c in this figure with J_{fold} of Eq. 3.19. Calculating λ at currents much lower than I_c, the flux generated by the coil at I_c based on Fig. 3.2, and J_{fold} from Eq. 3.19 we extract ξ. The results for both λ and ξ are depicted in Fig. 3.11. Since $\xi \ll \lambda$ there is a small temperature region where the Ginzburg-Landau analysis is self-consistent. Using Eq. 3.20, we find that the critical current density is on the order of 10^3 Amm^{-2} at the relevant temperature range, in agreement with measurements done in a field of 0.03 T on similar samples (18).

3.7 Conclusions

We demonstrated that the Stiffnessometer can measure penetration depth on a scale of millimeters, two orders of magnitude longer than ever before. This allows us to perform measurement closer to T_c and explore the nature of the superconducting phase transition, or determine the stiffness at low T in cases where it is naturally very weak as in thin films (19). The Stiffnessometer also allows measurements of very long coherence length ξ on the order of micrometers, equivalent to small critical current density on the order of

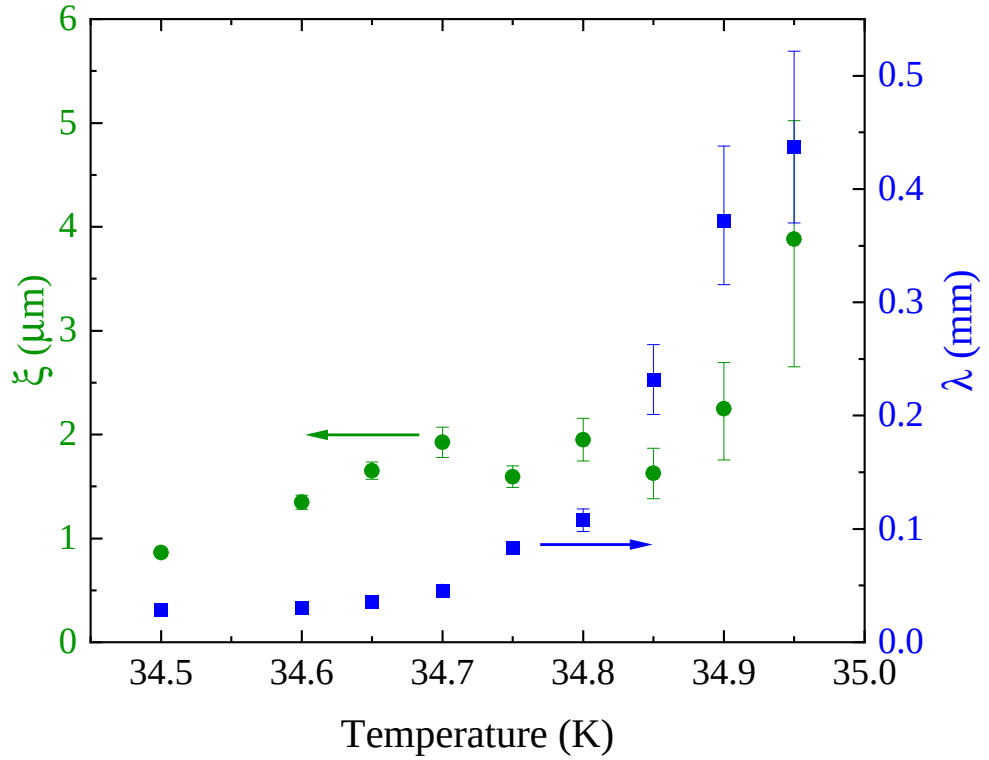

Figure 3.11: **Temperature dependence of the penetration depth and coherence length.** λ (T) and ξ (T) extracted from the data using the full Ginzburg-Landau analysis at a small temperature region where all approximations are valid and the stiffnessometer is not saturated.

10^3 Amm^{-2}, properties which again are useful close to T_c. The measurements are done in a single apparatus, at zero magnetic field, and with no leads, thus avoiding demagnetization, vortices, and out-of-equilibrium issues.

Acknowledgments

We are grateful for theoretical discussions with Assa Auerbach and Daniel Podolsky, mathematical assistance from Koby Rubinstein, and experimental tips from Ori Scaly. This study was financially supported by Israeli Science Foundation (ISF).

Bibliography

[1] Tinkham M., Introduction to Superconductivity, Courier Corporation, North Chelmsford, MA, 2004.

[2] Schrieffer, J.R., Theory of Superconductivity, CRC, Boca Raton, FL, 2018.

[3] De Gennes, P.G., Superconductivity of Metals and Alloys, CRC, Boca Raton, FL, 2018.

[4] Uemura, Y.J., Luke, G.M., Sternlieb, B.J., Brewer, J.H., Carolan, J.F., Hardy, W.N., Kadono, R., Kempton, J.R., Kiefl, R.F., Kreitzman, S.R., & others, 1989, Physical review letters: 62 2317. doi:10.1103/PhysRevLett.62.2317

[5] Lamhot, Y., Yagil, A., Shapira, N., Kasahara, S., Watashige, T., Shibauchi, T., Matsuda, Y., & Auslaender, O.M., 2015, Physical Review B: 91 060504(R). doi:10.1103/PhysRevB.91.060504

[6] Morenzoni, E., Glückler, H., Prokscha, T., Khasanov, R., Luetkens, H., Birke, M., Forgan, E.M., Niedermayer, C.h., & Pleines, M., 2002, Nuclear Instruments and Methods in Physics Research Section B: Beam Interactions with Materials and Atoms: 192 254. doi:10.1016/S0168-583X(01)01166-1

[7] Morenzoni, E., Prokscha, T., Suter, A., Luetkens, H., & Khasanov, R., 2004, Journal of Physics: Condensed Matter: 16 S4583. doi:10.1088/0953-8984/16/40/010

[8] Prozorov, R., & Giannetta, R.W., 2006, Superconductor Science and Technology: 19 R41. doi:10.1088/0953-2048/19/8/R01

[9] Drachuck, G., Shay, M., Bazalitsky, G., Berger, J., & Keren, A., 2012, Physical Review B: 85 184518. doi:10.1103/PhysRevB.85.184518

[10] Zhou, H., Maiorov, B., Wang, H., MacManus-Driscoll, J.L., Holesinger, T.G., Civale, L., Jia, Q.X., Foltyn, S.R., 2007, Superconductor Science and Technology: 21 025001. doi:10.1088/0953-2048/21/02/025001

[11] Shay, M., Keren, A., Koren, G., Kanigel, A., Shafir, O., Marcipar, L., Nieuwenhuys, G., Morenzoni, E., Suter, A., Prokscha, T., & others, 2009, Physical Review B: 80 144511. doi:10.1088/10.1103/PhysRevB.80.144511

[12] Talantsev, E.F., Strickland, N.M., Wimbush, S.C., Storey, J.G., Tallon, J.L., & Long, N.J., 2014, Applied Physics Letters: 104 242601. doi:10.1063/1.4883483

[13] Talantsev, E.F., & Tallon, J.L., 2015, Nature communications: 6 7820. doi:10.1038/ncomms8820

[14] Gavish, N., Kenneth, O., & Keren, A., 2021, Physica D: Nonlinear Phenomena: 415, 132767. doi:10.1016/j.physd.2020.132767

[15] Kapon, I., Salman, Z., Mangel, I., Prokscha, T., Gavish, N., & Keren, A, 2019, Nat. Comm: 10(1), 2463. doi:10.1038/s41467-019-10480-x

[16] Hecht, F., 2012, Journal of Numerical Mathematics: 20 251. doi:10.1515/jnum-2012-0013

[17] Samoilenka, A., & Babaev, E., 2020, Phys. Rev. B: 101 134512. doi:10.1103/PhysRevB.101.134512

[18] Wen, H.H., Yang, H.P., Li, S.L., Zeng, X.H., Soukiassian, A.A., Si, W.D., & Xi, X.X., 2003, EPL (Europhysics Letters): 64 790. doi:10.1209/epl/i2003-00627-1

[19] Keren, A., Blau, N., Gavish, N., Kenneth, O., Ivry, Y., & Suleiman, M., 2022, Supercond. Sci. Technol. 35 075013. doi:10.1088/1361-6668/ac7173

Chapter 4

Ground-state Inter-plane Superconducting Coherence Length of $La_{1.875}Sr_{0.125}CuO_4$

Itay Mangel[1] and Amit Keren[1]

[1]*Department of Physics, Technion-Israel Institute of Technology, Haifa, 3200003, Israel*

Published in PHYSICAL REVIEW B 109, 094519 (2024)

ABSTRACT

A long excitation coil piercing a superconducting ring is used to generate an ever increasing persistent current in the ring, until the current destroys the order parameter. Given that the penetration depth λ is known, this experiment measures, hypothetically, the coherence length ξ. We examine various aspects of this theoretically driven hypothesis by testing niobium rings with different dimensions, and by comparing the results to the known values of ξ. We then apply the method to two $La_{1.875}Sr_{0.125}CuO_4$ rings at $T \to 0$. In one, the current flows in the CuO_2 planes, hence it is set by ξ_{ab}. In the other, the current must cross planes and is determined by ξ_c. We find that $\xi_c = 1.3 \pm 0.1$ nm, and $\xi_{ab} < 2.3$ nm, indicating that at low temperatures the Cooper pairs are three dimensional.

4.1 Introduction

In the world of superconductivity there are two important length scales: the penetration depth λ, and the coherence length ξ. From an application point of view, λ^{-2} is a measure of superconducting carrier density and determines the current-carrying capabilities of a superconductor, while ξ sets the dimensions of Josephson junctions. There is an arsenal of experimental methods to directly measure the superconducting stiffness ρ_s and find λ via the relation $\rho_s = \frac{1}{\mu_0 \lambda^2}$ in different crystal orientations. However, methods of measuring ξ are limited. In the cuprates the coherence length in the ab plane (ξ_{ab}) was measured by the electron–boson spectral density function (1) and the vortex diameter via scanning tunneling microscopy (STM) (2). More commonly, one finds the second upper critical field H_{c2} near T_c using one of various methods, such as resistivity (3), the vortex-Nernst effect (4), specific heat (5), or thermal conductivity (6), extrapolating to $T = 0$ using theories that are not necessarily accurate over the whole temperature range, and uses the relation $\xi = \sqrt{\Phi_0/2\pi H_{c2}}$ (3; 7). All methods find ξ_{ab} on the scale of $1.5 - 3$ nm.

Measuring the coherence length in the c direction (ξ_c) in cuprates is more difficult since it is smaller and because cleaving in a plane including the c axis is challenging, making scanning techniques nearly impossible. ξ_c is bound by 1.5 nm, the thickness of a superconducting $Bi_2Sr_2CaCu_2O_{8+x}$ (Bi2212) monolayer (8). Extrapolations from high temperatures lead to $\xi \sim 1$ Å (7; 3). The only measured value of $\xi_c = 0.86$ nm at $T \to 0$, as far as we know, is from an H_{c2} of 250 T obtained using the electromagnetic flux compression method (9). This number has been questioned due to the transient nature of the magnetic field. The exact determination of ξ_c is becoming exceedingly important due to Josephson junctions created by twisted Bi2212 crystals (10; 11; 12; 13; 14) showing fractional Shapiro steps (15; 16), and as a challenge for cuprates theory.

A new approach for measuring ξ was suggested, and a very simple analysis formula was given, in Ref. (17). We name this approach the "Xiometer". Here, we briefly present the approach, justify the formula intuitively, and test it on Nb. Then, we apply it to ξ measurements in $La_{1.875}Sr_{0.125}CuO_4$ (LSCO-1/8). We find that the $\xi_c = 1.3 \pm 0.1$ nm determined by the Xiometer at $T \to 0$ is similar to the one obtained from $H_{c2} = 250$ T of Ref. (9) and calculation in Ref. (7). The implication of this finding is that the Cooper pairs are more spherical than previously thought.

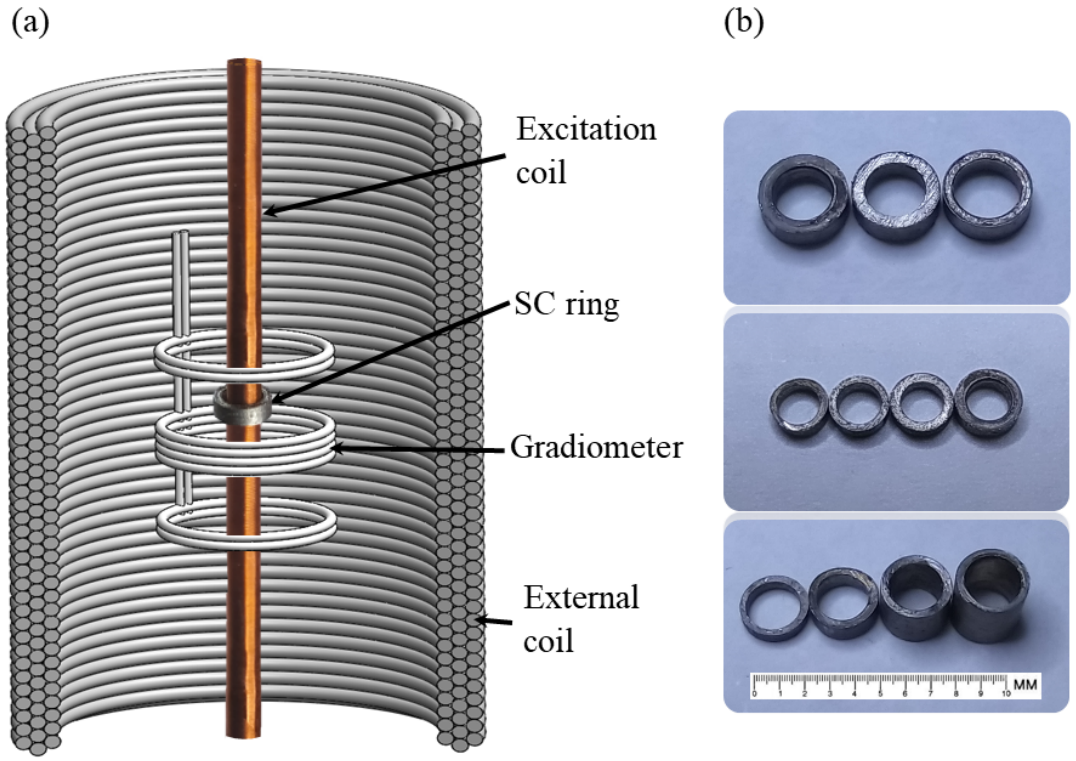

Figure 4.1: Experimental setup: (a) A niobium ring on a SC excitation coil (photo), an illustration of the gradiometer, and the external coil that serves as a shim. (b) Niobium rings with different inner radii (up), outer radii (middle), and different height (down).

The Xiometer, as the Stiffnessometer (18), is based on a long, current-carrying excitation coil (EC) piercing a superconducting (SC) ring and a measurement of the ring's magnetic moment. The measurement is done by moving both the ring and EC rigidly relative to gradiometer-type pickup loops as demonstrated in Fig. 4.1(a). The gradiometer is connected to a superconducting quantum interference device (SQUID). The ring and EC are cooled to $T < T_c$, and only then the current in the EC is turned on, and the magnetic moment of the ring is measured. The gauge invariant London equation states that

$$\boldsymbol{j} = -\rho_s \left(\boldsymbol{A}_{tot} - \frac{\Phi_0}{2\pi} \boldsymbol{\nabla} \varphi \right), \tag{4.1}$$

where $\boldsymbol{j}$ is the superconducting current density, $\boldsymbol{A}_{tot}$ is the total vector potential, Φ_0 is the flux quanta, and φ is the phase of the superconductor's order parameter. $\boldsymbol{A}_{tot}$ is a combination of the EC vector potential $\boldsymbol{A}_{ec} = \frac{\Phi_{ec}}{2\pi r}\hat{\varphi}$, and the SC ring self-induced vector potential $\boldsymbol{A}_{sc}$.

To minimize the kinetic energy after cooling, the superconductor sets its own phase gradient to zero. Since this phase is quantized, turning the EC current on, gently, conserves the phase. Therefore, at the start of a measurement, the London equation $\boldsymbol{j} = -\rho_s \boldsymbol{A}_{tot}$ is valid. In principle, this relation can be used to determine the stiffness and in this case the apparatus works as a Stiffnessometer. However, for bulk crystals at low temperatures, when λ is mach smaller than all dimensions of the sample, the SC ring exactly expels the applied flux, to keep $A_{tot} = 0$ deep inside the ring, regardless of λ. In this case, the apparatus cannot be used to properly determine the stiffness, but only the break point of the London equation, which is set by $\lambda\xi$ as we explain below. For crystals at $T \ll T_c$ we use literature values of λ and determine ξ. Hence, the name Xiometer.

4.2 Experimental details

The EC is homemade from a NbTi SC wire with 8 layers of 600 windings each (4800 in total), a wire diameter 0.106 mm, core diameter 0.35 mm, outer diameter 1.95 mm, coil length 60 mm, and flux to current ratio of $1.21 \cdot 10^{-7}\ Tm^2/A$. The apparatus is an add-on to a Cryogenics S700X SQUID magnetometer. External magnetic fields can be canceled by an external coil shown in Fig. 4.1(a), with a resolution of 5×10^{-7} T. The gradiometer radius is $R_{pl} = 13$ mm, its total height is 14.0 mm, and it is made of two

windings clockwise, four anticlockwise, and two clockwise, also depicted in Fig. 4.1(a). The set of Nb rings with different dimensions used in the first part of this experiment is shown in Fig. 4.1(b).

A typical data set of the SQUID output voltage V as a function of ring position z, is depicted in Fig. 4.2 with and without a ring. In these measurements the EC was allowed to transverse the gradiometer from one side to the next. The peaks and valleys away from $z = 0$ are due to the ends of the coil moving through the different winding groups of the gradiometer. Without the ring (red symbols) a moderately concave signal is observed around $z = 0$. This occurs when the center of the gradiometer and the center of the coil are at the same height. In this situation, flux through the gradiometer due to the EC barely changes, therefore the measurement is sensitive mostly to $\boldsymbol{A}_{sc}$. With the ring, a new signal (blue symbols) appears around $z = 0$. The difference is the net SC ring's signal (inset) and its amplitude is proportional to the magnetic moment m (or A_{sc}) of the ring. We note that a linear baseline was subtracted from both data sets due to the EC asymmetry (wires enter and exit from one side only). Linear baseline subtraction is irrelevant for the data analysis (see below).

As the EC current increases, the signal from the EC traversing the gradiometer overwhelms the ring's signal, as is clear from Fig. 4.3. Therefore, we limit the motion to a small region around $z = 0$. Consequently, it is impossible to detect the bottom of the signal and evaluate its amplitude. However, it is clear that the top of the peak at $z = 0$ becomes sharper with increasing current. Therefore, we use the second derivative of the SQUID's output voltage $V_0'' = \frac{d^2V}{d^2z}(z = 0)$ as a measure of m. This method also eliminates the undesired linear contribution of the coil's asymmetry. The conversion from V_0'' to m is explained shortly.

Finally, to keep the leads, coil, and ring cooled, liquid helium is sprayed via a diffuser from the bottom of the sample chamber on the EC and sample, and pumped along the current leads all the way to the top of the cryostat just before thicker leads are connected to the power supply. This way the EC remains cold even when currents of more than 10 A are applied.

The measured samples are 99.9% pure Nb rings, and two LSCO-1/8 single-crystal rings, grown using a traveling solvent floating-zone technique and cut with a laser cutter. Laue x-ray diffraction is used to identify the orientation of the crystals and the two rings

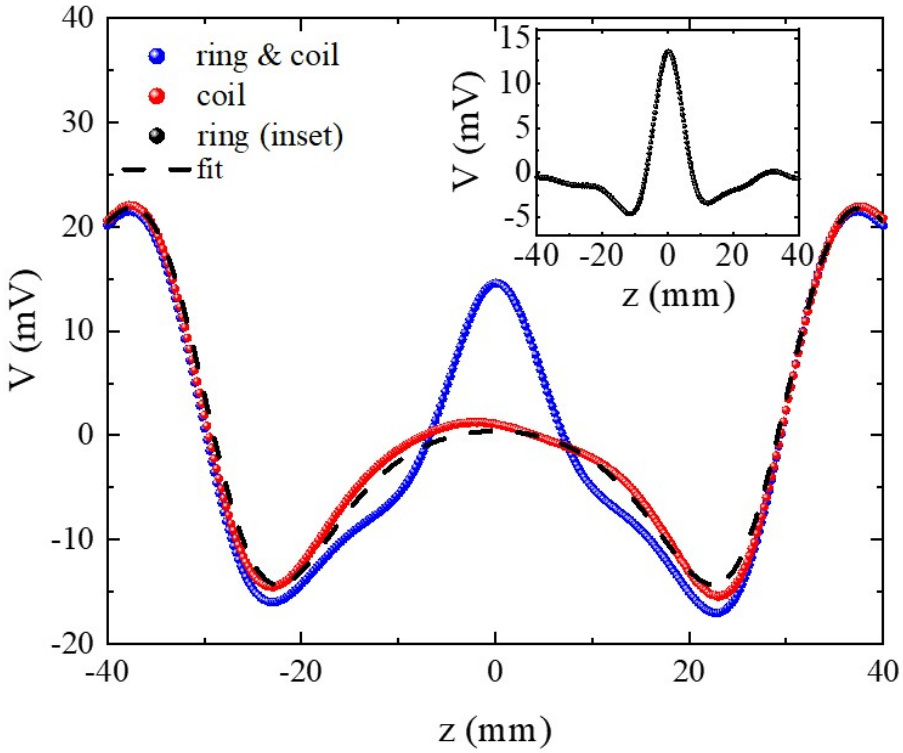

Figure 4.2: Raw data. Main: The SQUID output voltage V as a function of the relative position z of a Nb ring and coil to the gradiometer center. The EC current is 10.0 mA, $T = 1.6$ K, and the ring dimensions are $r_{in} = 1.0$ mm, $r_{out} = 1.75$ mm, and $h = 1.0$ mm. Red spheres are the EC signal without the ring. Blue spheres are the combined signal of the ring and coil. The dashed black line shows a numerical fit used to determine the conversion factor between the output voltage of the SQUID and the magnetic moment of a sample. Inset: The subtraction of the two measurements giving the ring's signal. The data presented are after subtraction of a linear component.

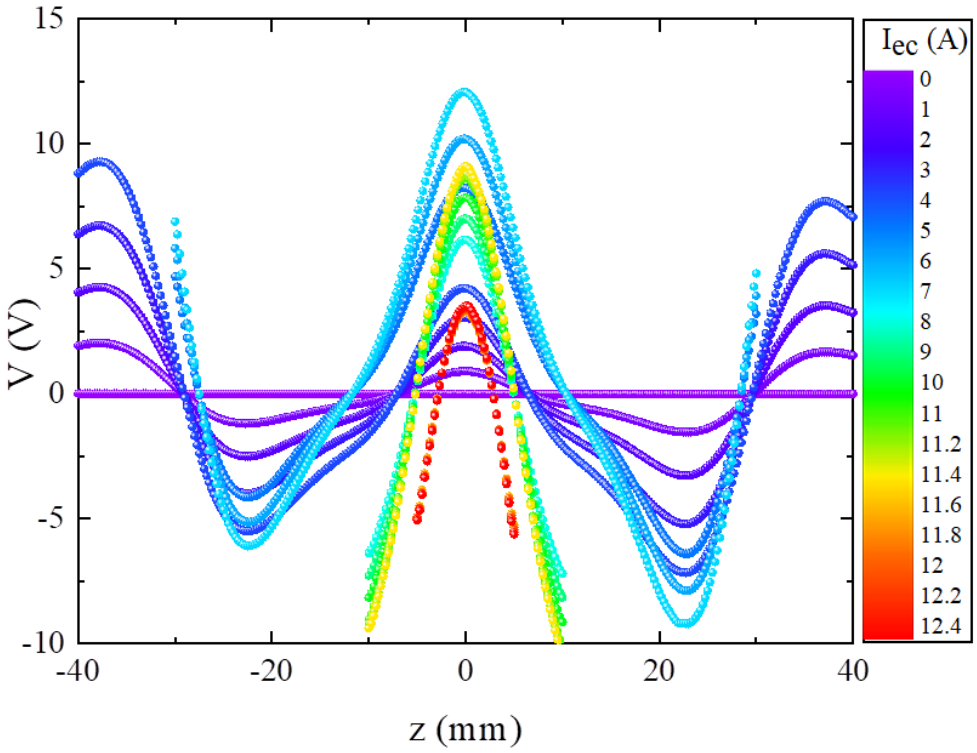

Figure 4.3: Raw data in a limited scan length. SQUID output voltage as a function of the ring's position z for different applied EC currents. For low currents $(0 - 4\ A)$ it is possible to measure the full signal of the coil and the ring (see Fig. 4.2). For higher currents the coil's signal exceeds the detector's dynamic range and a measurement on a shorter range is needed. Consequently, the edges of the coil are not observed and the signal amplitude cannot be determined. Therefore, the second derivative of the signal V_0'' is used to determine the moment as explained in the text.

are cut in different orientations of the CuO_2 planes relative to the ring's symmetry axis. In one ring the CuO_2 planes are parallel to the symmetry axis. In the other ring the planes are perpendicular to this axis. We address the two rings as a and c rings, respectively. In the c ring, current can flow around the ring on the CuO_2 planes without crossing planes. In order to flow around the a ring current must cross the CuO_2 planes.

4.3 Analysis

A detailed derivation of the Xiometer analysis theory can be found in Ref. (17). Here, we provide a back of the envelope calculation that gives the same answer up to a numerical factor. Since, as mentioned before, deep in the superconductor there are no currents (and no fields), $A_{tot} = 0$. Therefore, the magnetic flux of the EC, Φ_{ec}, is perfectly matched by the magnetic flux from the supercurrent Φ_{sc} in the ring, namely, $\Phi_{sc} = -\Phi_{ec}$. For low Φ_{ec} we assume that the supercurrent density j is uniform along a cylinder of width λ attached to the inner rim of the ring at r_{in} as in Fig. 4.4(a). The magnetic flux of such a current is $\Phi_{sc} = \mu_0 \lambda j \pi r_{in}^2$. When Φ_{ec} increases, j will also increases until it reaches the critical current density j_c of the SC. When this happens the order parameter is destroyed next to the inner rim, and the current has to retreat from the inner rim to an effective radius r_{eff} demonstrated in Fig. 4.4(b). This process continues until $r_{eff} = r_{out}$ as shown in Fig. 4.4(c). In this situation vortices start entering the sample, and the applied flux is named the critical flux; it is given by $\Phi_c = \mu_0 \lambda j_c \pi r_{out}^2$. Using the definition $j = e^* n v = \frac{m^* v}{\mu_0 \lambda^2 e^*}$ where n, v, e^*, and m^* are the carrier's density, velocity, charge, and mass, respectively, and the relations of the critical momentum $m^* v_c = \frac{\hbar}{\sqrt{3}\xi}$ (19), and the flux quanta $\Phi_0 = 2\pi\hbar/e^*$, one finds

$$\frac{\Phi_c}{\Phi_0} = \frac{r_{out}^2}{2\sqrt{\alpha}\lambda\xi} \tag{4.2}$$

where $\alpha = 3$. In the exact derivation (17) $\alpha = 2$.

It should be pointed out that the SC produces a field in the volume where the order parameter is destroyed. One might wonder if this field penetrates as vortices into the SC when it is of type II. It was found in Ref. (20; 21), using a scanning SQUID, that in an ultrathin film that shows vortices due to a sporadic magnetic field, the current in the coil does not add new vortices. This is not surprising since there is no pressure from the

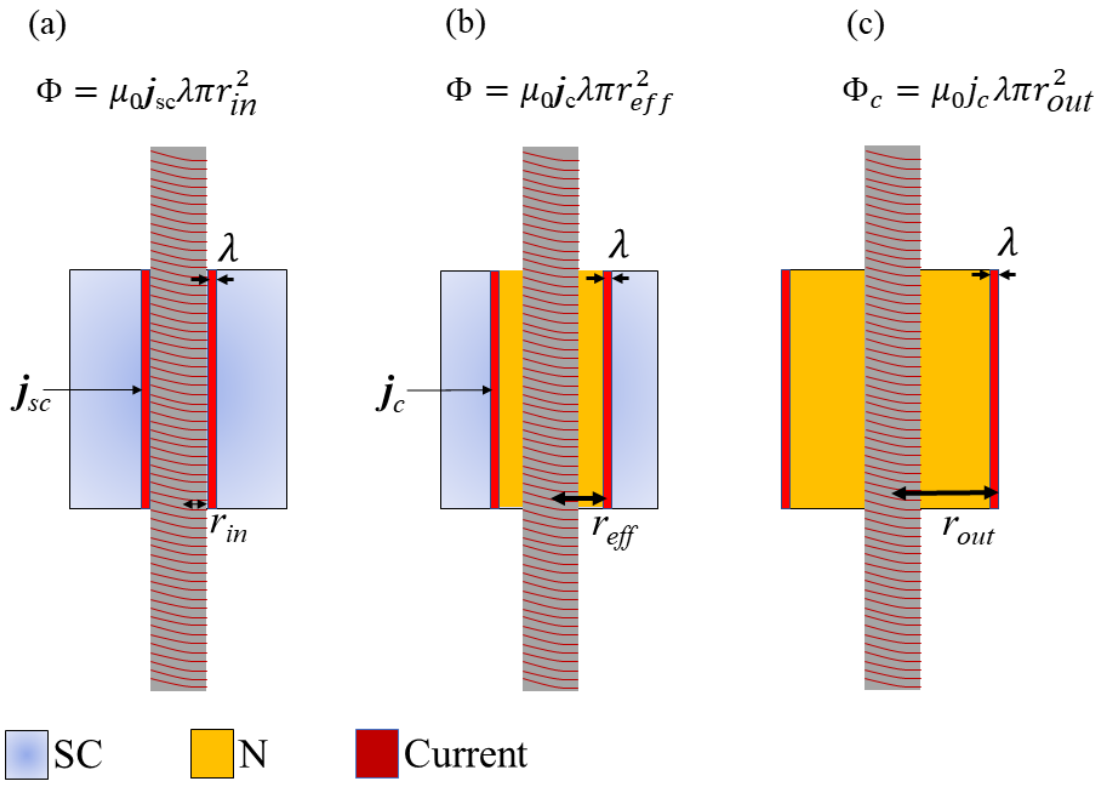

Figure 4.4: Schematic description of the superconductor screening currents evolution for increasing flux in the EC. Each sketch shows cross sections of the EC and a cylindrical ring. Yellow and gray regions represent the normal and SC states, respectively. The current flows in the red region. The flux current relations are given at the top of each panel. (a) Low flux in the EC resulting in screening current along the inner rim of the cylinder. (b) Stronger flux in the EC forces the screening current to move outwards while the inner region of the cylinder becomes normal. (c) The critical flux is reached once the screening current reaches the outer radius of the cylinder and its bulk is no longer SC.

twisted field lines bypassing the sample to penetrate into the sample. In our case the field lines are straight and in the center of the sample. They are in the most convenient place to be and do not need to penetrate the sample as vortices.

The output voltage of the SQUID is related to the flux through the gradiometer by $V = K\Phi$ where K is a conversion factor. When a sample with magnetic moment m is located at height z from the center of a single pickup loop with radius R_{pl}, its flux through the loop is $\Phi = \frac{\mu_0 R_{pl}^2 m}{2(R_{pl}^2+z^2)^{3/2}}$. To calibrate K we measured our coil for which we calculate the magnetic moment as a bundle of current loops with moment $m = \pi r^2 I$ each, where r is the loop radius. The voltage output in this case is

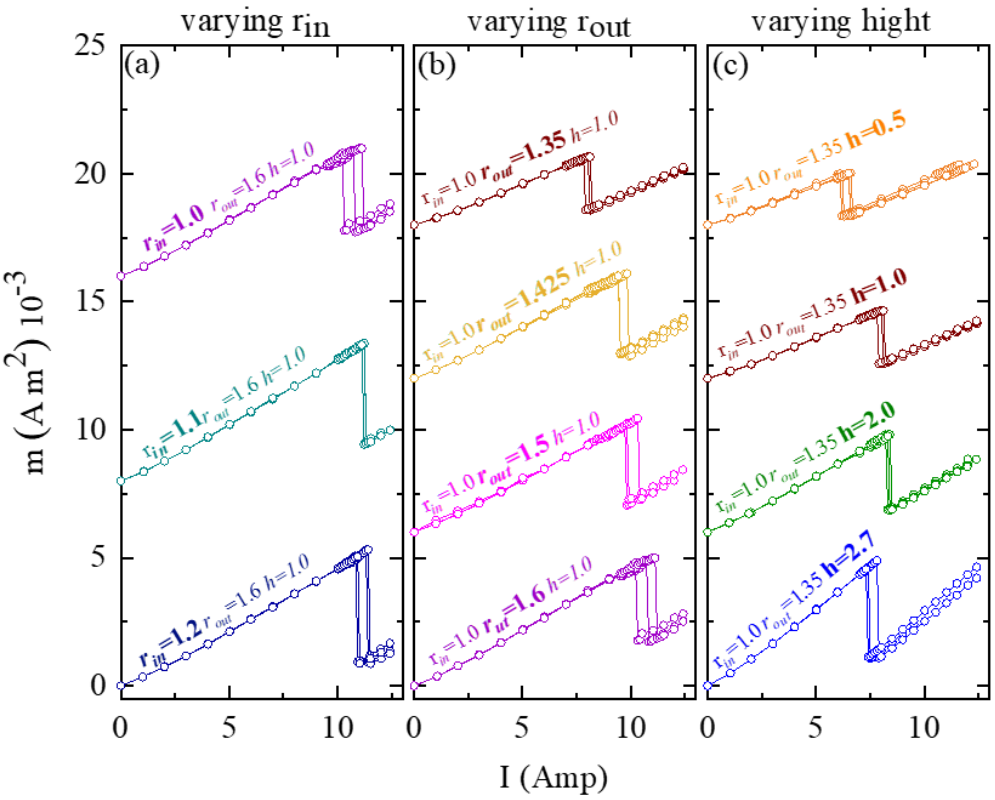

Figure 4.5: Critical current of different rings. Nb ring's magnetic moment m obtained using Eq. 4.4 as a function of current in the excitation coil. The measurements are arranged in three sets. In each set only one parameter of the rings is changing. (a) Only the inner radius of the rings varies, (b) only the outer radius of the rings differs, and (c) only the height of the rings changes. The experiment was done more than once with each ring for statistical purposes. The signal grows linearly with the EC current until it drops at some critical current I_c. The drop is due to a phase slip. The critical current varies between runs of the same ring due to thermal instability.

$$V(z) = \frac{\mu_0 R_{pl}^2 \pi I K}{2} \sum_i r_i^2 \left[\frac{2}{(R_{pl}^2 + (z + z_i - \Delta_{pl})^2)^{3/2}} + \frac{2}{(R_{pl}^2 + (z + z_i + \Delta_{pl})^2)^{3/2}} - \frac{4}{(R_{pl}^2 + (z + z_i)^2)^{3/2}} \right], \tag{4.3}$$

where z is the distance between the center of the coil and the center of the gradiometer, Δ_{pl} is the difference between the gradiometer's bundles, r_i is the radius of the ith layer, and z_i the height of the ith loop. By fitting Eq. 4.3 to a measurement of the coil with a current of 10.0 mA, as shown in Fig. 4.2, we find the conversion factor to be $K = 63.035$ V/Tmm^2. This procedure gives

$$m = 4.95 * 10^{-10} \cdot V_0'' \tag{4.4}$$

where V_0'' is in units of mV/mm^2, and m in units of Am^2.

4.4 Results

To test Eq. 4.2 we measure a set of Nb rings with different inner and outer radii, and different heights. Figure. 4.5 presents m as a function of the applied EC current I. $m(I)$ is linear for low currents. At some high current I_c, a jump in m is observed indicating that the critical flux in the coil Φ_c is reached, and that a phase slip has taken place. This process was done more than once for each ring for better statistics.

The results of the experiment with the Nb rings are separated in Fig. 4.5 into three sets. In each set only one parameter is changing: the inner radius r_{in} [Fig. 4.5(a)], outer radius r_{out} [Fig. 4.5(b)], and the ring's height h [Fig. 4.5(c)]. The variation of r_{in} is limited because of the EC. Nevertheless, it does not seem to impact the Φ_c. Variation of r_{out} has a noticeable and systematic influence on the critical flux as expected from Eq. 4.2. Finally, between the smallest $h = 0.5$ mm and all other values of h a variation in Φ_c is detected. This is not expected from Eq. 4.2. We ascribe this exception to the fact that Eq. 4.2 is derived in the limit of a tall, cylinderlike ring and the $h = 0.5$ mm is not in this limit. A summary of I_c as a function of L ($L = r_{in}, r_{out}, h$) is depicted in the inset of Fig. 4.6 where it is clear that r_{out} is the most important parameter. The error bars are statistical.

In Fig. 4.6 we present the r_{out} dependence of I_c on a full scale including the origin.

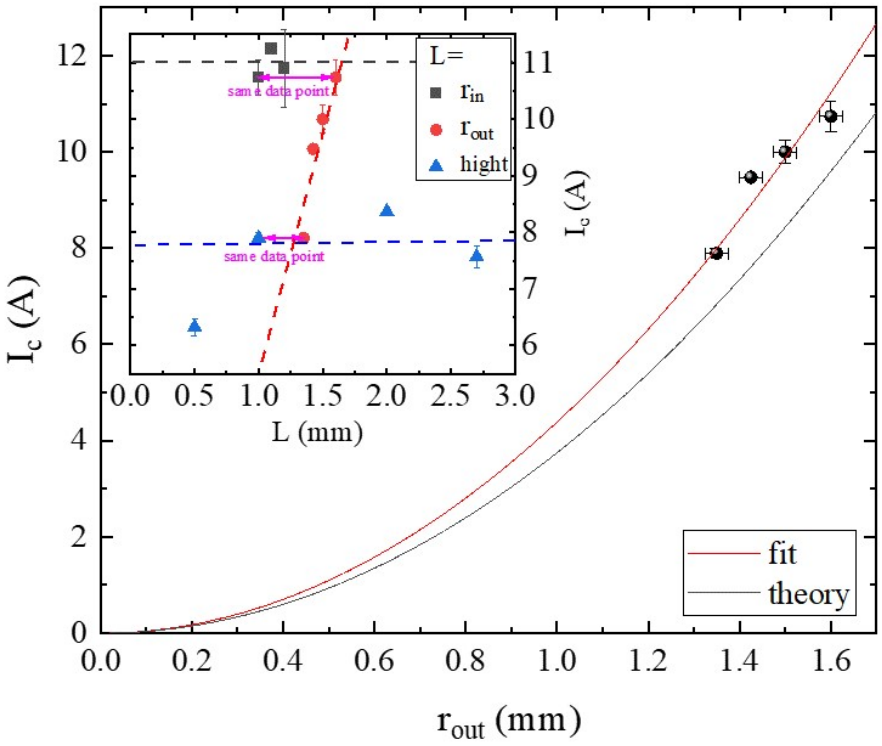

Figure 4.6: Critical current as function of different Nb ring sets. Main: The set with changing outer radius. The black line follows Eq. 4.2 for $\lambda = 38$ nm and $\xi = 39$ nm (21). The red line is a parabolic fit to the data points (through the origin). The fit parameter amounts to $\lambda\xi = 1267 \pm 32.5$ nm^2. Inset: Black squares-rings with different inner radius; red circles-rings with varying outer radius; blue triangles-rings with changing height. The dashed lines are a guide to the eye.

When taking λ and ξ of Nb as 38 and 39 nm, respectively, from Ref. (21) and applying those in Eq. 4.2 (black line), we find reasonable agreement between the measurements and theory. When fitting Eq. 4.2 to the data (red line), we find $\lambda\xi = 1267 \pm 32.5$ nm^2 while the literature value is 1482 nm^2.

Having established Eq. 4.2 we use it to measure the coherence length of the two LSCO-1/8 rings shown in the insets of Fig. 4.7 with orientation and planes illustrated in the main panel. Previously, it was found that the persistent current critical temperature for the c ring is higher than for the a ring (22). Figure. 4.7 shows m at $T = 1.6$ K as a function of EC current for both the a and c rings. At low currents, $m(I)$ is linear for both rings. But at about 2.2 A, the a-ring moment m_a has a break point where its behavior changes. The c-ring moment $m_c(I)$ stays linear all the way up to our maximum current of 12.4 A. We interpret this break point as the critical flux where vortices start entering the sample.

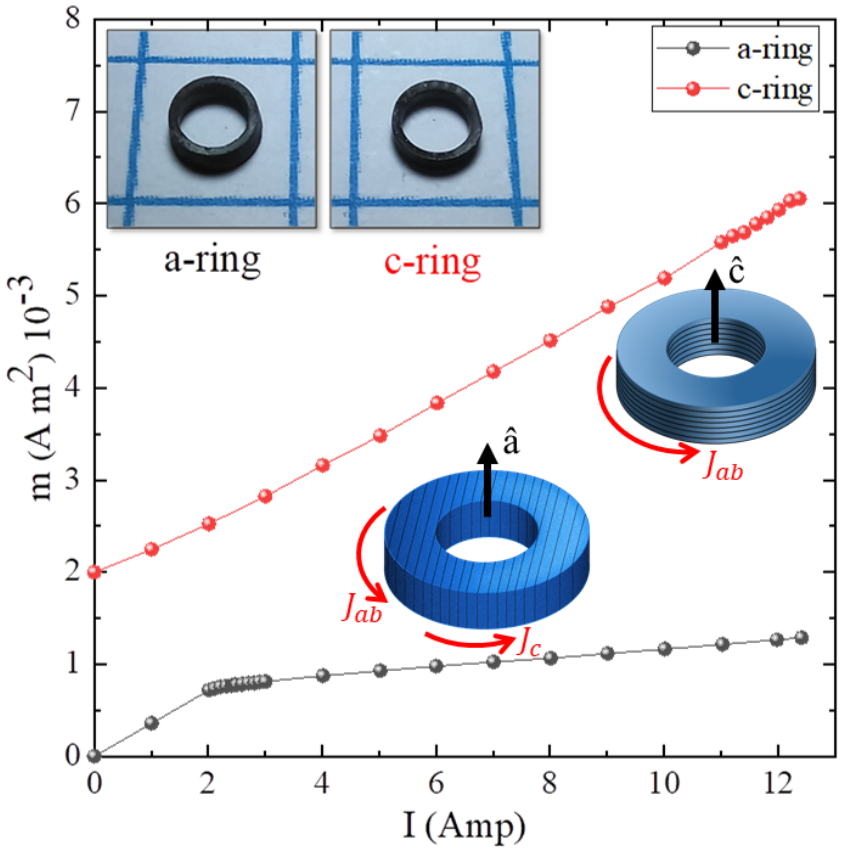

Figure 4.7: Critical flux determination of LSCO-1/8. $m(I)$ for two rings. The insets show pictures of the rings, the orientation of the planes, and the directions of the current in the ring j_{ab} and j_c. Their parameters are $r^a_{in} = 1.05$ mm, $r^a_{out} = 1.42$ mm, and $h_a = 1.02$ mm, and $r^c_{in} = 1.05$ mm, $r^c_{out} = 1.35$ mm, and $h^c = 0.89$ mm. I_c of the a ring is 2.2 A and I_c of the c ring is higher than the maximum available current of 12.4 A.

4.5 Discussion

The fact that no break point is observed in the c ring suggests that the flow inside the CuO_2 plane is not disrupted by a coil current of a few amperes. Alternatively, for current in the c direction, the radial penetration depth λ_{ab} is more than ten times that of current in the ab plane λ_c. According to Eq. 4.2 (given an isotropic ξ) the smallest critical flux is due to current in the c direction. Therefore, the assumption here is that the bottleneck for current in the a ring is the flow between planes (c direction), and that the order parameter is destroyed first on the planes perpendicular to the flow.

At the experiment's temperature, the penetration depths of LSCO with $x = 0.125$ are $\lambda_c = 4500$ nm (23), and $\lambda_{ab} = 350$ nm (22). The outer radii of the a and c rings are $r^a_{out} = 1.42$ mm, and $r^c_{out} = 1.35$ mm. Following Eq. 4.2 with λ_c we find $\xi_c = 1.3 \pm 0.1$ nm. We can also place an upper bound on $\xi_{ab} < 2.3$ nm using λ_{ab}.

The Ginzburg–Landau ξ at $T = 0$, which we measure with the Xiometer, is related to the Cooper pair size ξ_0 by a factor of 0.74 (19). ξ_0, in turn, is set by $\hbar v_F/\Delta$ where v_F is the Fermi velocity and Δ is the superconducting gap. However, in the cuprates Δ varies along the Fermi surface, v_F in the c direction is not known, and there is no theory that can be used to extract more fundamental properties or be contrasted with our findings. A derivation of such a theory could be useful.

4.5.1 Conclusions

To summarize, the relation between the dimensions of a superconducting ring, pierced by a long coil, and the critical flux in the coil, is tested. It is demonstrated that if the ring's height is similar to or bigger than its radii, only the outer radius of the ring is relevant, and the critical flux depends quadratically on this radius. Using this observation we measure ξ_{ab} and ξ_c of LSCO-1/8 at $T = 1.6$ K. Despite the cuprates being very anisotropic systems, we find that ξ_c is similar to the literature value of ξ_{ab}, indicating a three-dimensional Cooper pair.

Acknowledgements

This research was funded by the Israeli Science Foundation Grant No. 3875/21.

Bibliography

[1] Hwang J., 2021, Scientific Reports 11:11668, doi.org/10.1038/s41598-021-91163-w

[2] Pan, S.H., Hudson, E.W., Gupta, A.K., Ng, K.W., Eisaki, H., Uchida, S., & Davis, J.C., 2000, Phys. Rev. Lett. 85, 1536, doi:10.1103/PhysRevLett.85.1536

[3] Oh, B., Char, K., Kent, A.D., Naito, M., Beasley, M.R., Geballe, T.H., Hammond, R.H., Kapitulnik, A., & Graybeal, J.M., 1988, Phys. Rev. B 37, 7861, doi:10.1103/PhysRevB.37.7861

[4] Oh, B., Char, K., Kent, A.D., Naito, M., Beasley, M.R., Geballe, T.H., Hammond, R.H., Kapitulnik, A., & Graybeal, J.M., 2003, Science 299, 86, doi:10.1126/science.1078422

[5] Wang, Y., & Wen, H.H., 2008, EPL 81 57007, doi:10.1209/0295-5075/81/57007

[6] Grissonnanche, G., Cyr-Choinière, O., Laliberté, F., René de Cotret, S., Juneau-Fecteau, A., Dufour-Beauséjour, S., Delage, M.E., LeBoeuf, D., Chang, J., Ramshaw, B.J., Bonn, D.A., Hardy, W.N., Liang, R., Adachi, S., Hussey, N.E., Vignolle, B., Proust, C., Sutherland, M., Krämer, S., Park, J.H., Graf, D., Doiron-Leyraud, N., & Taillefer, L., 2014, Nature Communications 5:3280, doi:10.1038/ncomms4280

[7] Petrenko, E.V., Omelchenko, L.V., Terekhov, A.V., Kolesnichenko, Yu.A., Rogacki, K., Sergeyev, D.M., & Solovjov, A.L., 2022, Low Temp. Phys. 48, 755–762, doi:10.1063/10.0014015

[8] Yu, Y., Ma, L., Cai, P., Zhong, R., Ye, C., Shen, J., Gu, G.D., Chen, X.H., & Zhang Y., 2019, Nature 575 156–163, doi:10.1038/s41586-019-1718-x

[9] Sekitani, T., Miura, N., Ikeda, S., Matsuda, Y.H., & Shiohara, Y., 2004, Physica B 346–347, doi:10.1016/J.PHYSB.2004.01.098

[10] Lee, Y., Martini, M., Confalone, T., Shokri, S., Saggau, C.N., Wolf, D., Gu, G., Watanabe, K., Taniguchi, T., Montemurro, D., Vinokur, V.M., Nielsch, K., & Poccia, N., 2023, Adv. Mater. 35, 2209135, doi:10.1002/adma.202209135

[11] Klemm, R.A., 2005, Adv. Philos. Mag. 85, 801, doi:10.1080/14786430412331314573

[12] Song, X.Y., Zhang, Y.H., & Vishwanath, A., 2022, Adv. Phys. Rev. B 105, L201102, doi:10.1103/PhysRevB.105.L201102

[13] Lee, J., Lee, W., Kim, G.Y., Choi, Y.B., Park, J., Jang, S., Gu, G., Choi, S.Y., Cho, G.Y., Lee, G.H., & Lee, H.J., 2021, Nano Lett. 21, 10469, doi:10.1021/acs.nanolett.1c03906

[14] Takano, Y., Hatano, T., Fukuyo, A., Ishii, A., Ohmori, M., Arisawa, S., Togano, K., & Tachiki, M., 2002, Phys. Rev. B 65, 140513, doi:10.1103/PhysRevB.65.140513

[15] Zhao, S.Y.F., Cui, X., Volkov, P.A., Yoo, H., Lee, S., Gardener, J.A., Akey, A.J., Engelke, R., Ronen, Y., Zhong, R., Gu, G., Plugge, S., Tummuru, T., Kim, M., Franz, M., Pixley, J.H., Poccia, N., & Kim, P., 2023, Science 382, 1422, doi:10.1126/science.abl8371

[16] Tummuru, T., Plugge, S., & Franz, M., 2022, Phys. Rev. B 105, 064501, doi:10.1103/PhysRevB.105.064501

[17] Gavish, N., Kenneth, O., & Keren, A., 2021, Physica D 415, 132767 1, doi:10.1016/j.physd.2020.132767

[18] Mangel, I., Kapon, I., Blau, N., Golubkov, K., Gavish, N., & Keren, A., 2020, Phys. Rev. B 102, 024502, doi:10.1103/PhysRevB.102.024502

[19] Tinkham, M., 2004, Introduction to Superconductivity, Vol. 1,

[20] Khanukov, A., Mangel, I., Wissberg, S., Keren, A., & Kalisky, B., 2022, Phys. Rev. B 106, 144510, doi:10.1103/PhysRevB.106.144510

[21] Maxfield, B.W., & Mclean, W.L., 1965, Phys. Rev. 139, A1515, doi:10.1103/PhysRev.139.A1515

[22] Kapon, I., Salman, Z., Mangel, I., Prokscha, T., Gavish, N., & Keren, A., 2019, Nat. Commun. 10, 2463, doi:10.1038/s41467-019-10480-x

[23] Panagopoulos, C., Cooper, J.R., Xiang, T., Wang, Y.S., & Chu, C.W., 2000, Phys. Rev. B 61, R3808, doi:10.1103/PhysRevB.61.R3808

Chapter 5

The two critical temperatures conundrum in $La_{1.83}Sr_{0.17}CuO_4$

Abhisek Samanta[1], Itay Mangel[2], Amit Keren[2], Daniel P. Arovas[3] and Assa Auerbach[2]

[1] *Department of Physics, The Ohio State University, Columbus OH 43210, USA*

[2] *Department of Physics, Technion-Israel Institute of Technology, Haifa, 3200003, Israel*

[3] *Department of Physics, University of California at San Diego, La Jolla, California 92093, USA*

Published in SciPost Physics 16, 148 (2024)

ABSTRACT

The in-plane and out-of-plane superconducting stiffness of $La_{1.83}Sr_{0.17}CuO_4$ rings appear to vanish at different transition temperatures, which contradicts thermodynamical expectation. In addition, we observe a surprisingly strong dependence of the out-of-plane stiffness transition on sample width. With evidence from Monte Carlo simulations, this effect is explained by very small ratio α of inter-plane over intra-plane Josephson couplings. For three dimensional rings of millimeter dimensions, a crossover from layered three dimensional to quasi one dimensional behavior occurs at temperatures near the thermodynamic transition temperature T_c, and the out-of-plane stiffness *appears* to vanish below T_c by a temperature shift of order $\alpha L_a/\xi^{\parallel}$, where $L_a/\xi^{\parallel}$ is the sample's width over coherence length. Including the effects of layer-correlated disorder, the measured temperature shifts

can be fit by a value of $\alpha = 4.1 \times 10^{-5}$, near T_c, which is significantly lower than its previously measured value near zero temperature.

5.1 Introduction

A homogeneous three-dimensional superconductor is expected to exhibit a single transition temperature T_c at which the order parameter, $\Delta(T)$, and all the superconducting stiffness components vanish (1; 2). In this regard, recent measurements of the *ab*-plane ($\rho^{\parallel}$) and *c*-axis ($\rho^{\perp}$) stiffnesses of $La_{1.875}Sr_{0.125}CuO_4$ crystals by Kapon *et. al.* (3) have been puzzling. Counter to the expectation above, $\rho^{\perp}$ was seen to vanish at ${T_c}^{\perp}$, which is about 0.64 K below the vanishing temperature ${T_c}^{\parallel}$ of $\rho^{\parallel}$.

Disorder – Short range uncorrelated disorder is not expected to affect the critical behavior of a superconductor, by Harris's criterion (4). On the other hand, the cuprates are known to be highly anisotropic layered superconductors. Layer-correlated disorder, (or a gradient in dopant concentration along the *c* axis) (5; 6), yields a distribution of $\rho^{\parallel}$ and ${T_c}^{\parallel}$. Experimentally, such inhomogeneity is manifested by a high temperature tail of the measured $\rho^{\parallel}$ above the average ${T_c}^{\parallel}$, while $\rho^{\perp}$ vanishes at the lowest values of ${T_c}^{\parallel}$ (see Appendix 5.8). However, ${T_c}^{\parallel}$ in Ref. (3) exhibited inhomogeneity broadening of ~ 0.1 K, which is significantly below the apparent difference in T_c's.

Finite size effects – An alternative proposition is that finite sample dimensions play a role. Previous Monte-Carlo simulations (7; 8) of the 3dXY model found strong effects of sample dimensions on the temperature dependent stiffness coefficients. These effects are expected to be enhanced by high anisotropy.

This paper explores finite size effects experimentally and theoretically. We report systematic stiffness measurements near T_c for $La_{1.83}Sr_{0.17}CuO_4$ rings with widths L_a, L_c ranging between $L = 0.1$ to 1 millimeter. ${T_c}^{\parallel}$ is found to be weakly dependent on L_c, L_a. In contrast, a significant reduction of ${T_c}^{\perp}$ for decreasing width L_a is observed. This behavior is not expected for layer-correlated inhomogeneity. The relatively strong finite size effect demands theoretical explanation.

Phenomenologically, the monotonous relation between T_c and $\rho^{\parallel}$ in cuprates (9), and the observed jump in $\rho^{\parallel}$ at T_c in ultra-thin films (10), suggest that T_c is driven by superconducting phase fluctuations (11), and vortex unbinding (12). Therefore we appeal

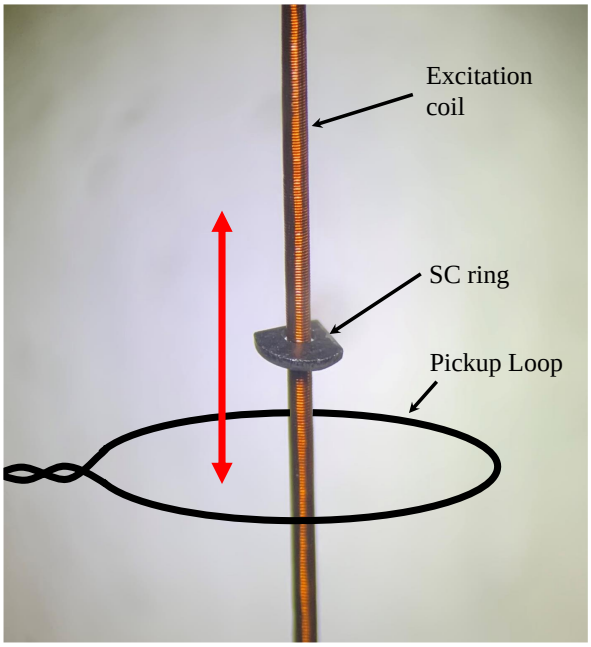

Figure 5.1: A superconducting ring cut in two directions, on the excitation coil. The red double arrow shows the moving direction of the schematic magnetization measuring pickup-loop, relative to both coil and ring.

to the three dimensional classical XY (3dXY) model (rather than BCS theory) to explain the stiffness temperature dependence toward T_c.

We applied a Monte-Carlo simulation with Wolff cluster updates on finite three dimensional lattices. The in-plane and intra-plane superconducting stiffness coefficients of the highly anisotropic 3dXY model appeared to vanish at different transition temperatures. The numerical simulations showed a strong dependence of the apparent inter-plane stiffness vanishing temperature $T_c^{\perp}$ on the layers' finite width. This dependence exceeded the magnitude expected of critical fluctuations.

The numerical and experimental observations are understood as follows. Inter-layer mean field theory (13), predicts a thermodynamic transition temperature slightly above the two dimensional Berezinskii-Kosterlitz-Thouless (12) (BKT) transition at $T_{\rm BKT} < T_c$. 3dXY critical behavior (1) is expected to be observed only very close to T_c. As temperature approaches T_c, the finite sample width L_a drives a crossover of $\rho^{\perp}$ to the stiffness of a one dimensional XY (1dXY) chain (8). This crossover results in an exponentially flat temperature dependence of $\rho^{\perp}(T, L_a)$ below T_c. For finite experimental or numerical resolution, such singular behavior always appears as vanishing of $\rho^{\perp}$ at $T_c^{\perp}(L_a) < T_c$.

We compare our theoretical analysis to the experimental values $T_c^{\perp}(L_a)$, and use the fit to estimate of the anisotropy parameter of $La_{1.83}Sr_{0.17}CuO_4$ near its thermodynamic T_c.

5.2 Experimental setup

Measurements were carried out with a 'stiffnessometer' apparatus (14) which comprises of a long excitation coil piercing a superconducting ring. A bias current in the coil creates an Aharonov-Bohm (AB) vector potential $\boldsymbol{A}$ which, by London's equation, produces a persistent current that is measured by the induced (dia-)magnetization m^α along the coil axis α. One then measures m^α by moving a pickup loop relative to the ring and coil. The apparatus is shown in Fig. 5.1.

$La_{2-x}Sr_xCuO_4$ is known to grow in large single crystals allowing significant size reductions. Therefore, powder of different doping is prepared from stoichiometric ratios of 99.99% pure CuO, La_2O_3, and $SrCO_3$ to make feed and seed rods. This powder is turned into a single crystal using an image furnace with four elliptic mirrors focusing 300 W halogen lamps. The growth was stabilised over 100 hr without any change of the lamp 59% power. Growth rate of 1.0 mm/h, down-ward translation of 0.15 mm/h, and rotation in opposite directions at 15 rmp were used. The emerging crystals looked like Fig. 1 of Ref. (15). After the growth, the crystals were annealed in argon environment at $T = 850$ C for 120 hr to release internal stress. Finally, the crystals were oriented with a Laue camera, and cut into rings with a femtosecond laser cutter. For each doping two rings, labelled by a and c, were prepared with their coil axes parallel (a) and perpendicular (c) to the CuO_2 planes. The width and height of the rings was varied by the laser, or polished down to the geometries shown in Fig. 5.2a,b.

For the a-ring, we varied mostly the narrowest (bottleneck) widths of the $a-b$ planes, L_a, whereas for the c-ring we varied both L_c and L_a (see Figs. 5.2a,b). Fig. 5.2(c) shows the narrowest bottleneck geometry of the a-ring. The requirement to: cut, measure, cut, measure, et cetera, the same pair of samples proved challenging. In most cases one of the samples broke during some step of the process. Only one pair of $La_{1.83}Sr_{0.17}CuO_4$ rings survived the reduction of L_a by factor of 10 between the initial and final cutting stages. The magnetization of this sample is depicted in Fig. 5.2.

When the transverse London penetration depth λ_c (λ_a) is smaller than the sample width L_c (L_a), the induced persistent current in the superconductor precisely cancels the AB flux of the coil. This results in a temperature independent induced magnetization m^a (m^c) at low temperatures.

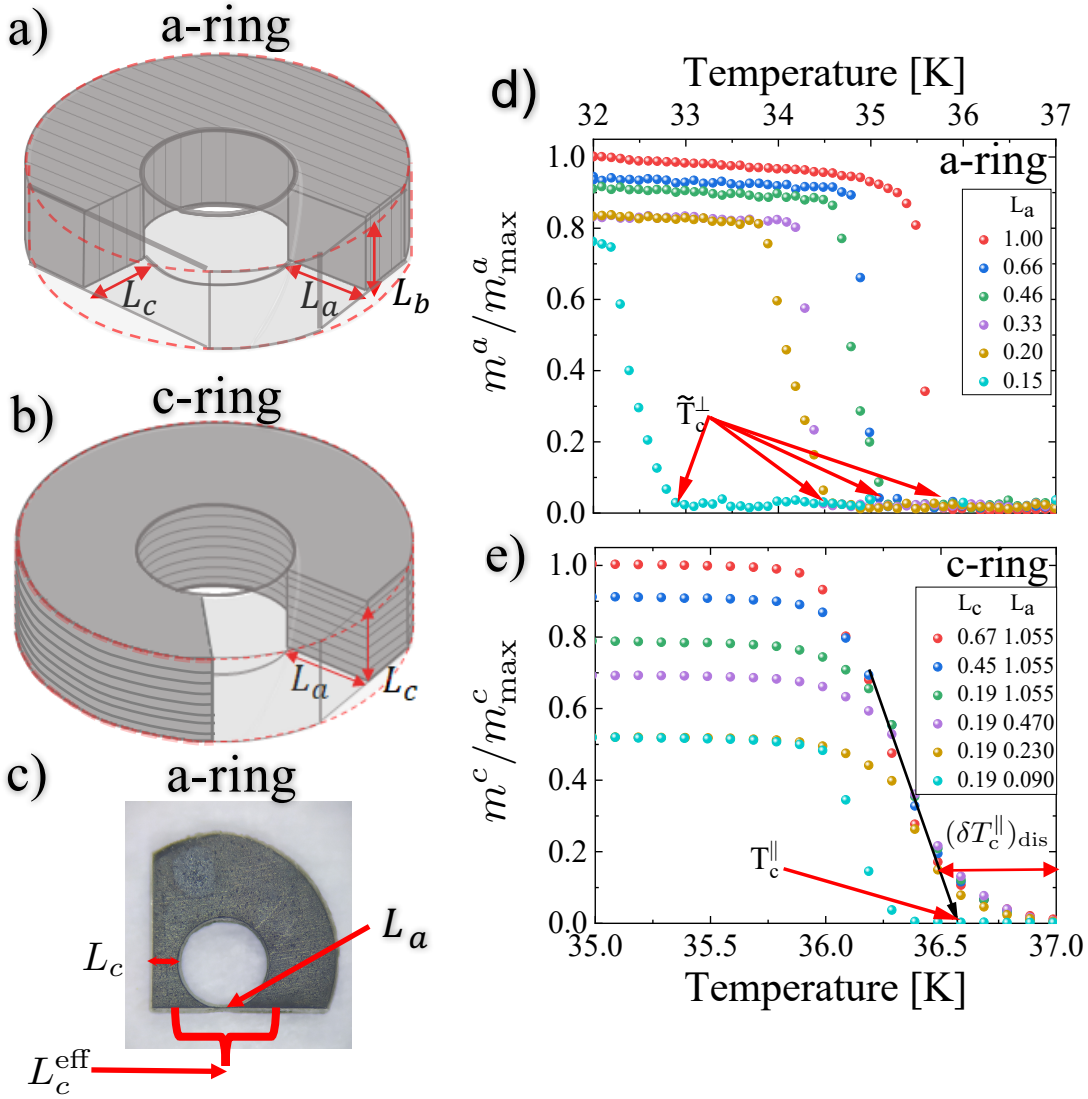

Figure 5.2: Experimental configuration and normalized magnetizations of $La_{1.83}Sr_{0.17}CuO_4$ rings for a fixed 1 mA current in the coil. (a) The interior of the *a*-ring. The CuO_2 planes are parallel to the ring's symmetry axis. This ring is sequentially polished and laser-cut, to reduce the layers' width L_a in the bottleneck region. (b) The interior of the *c*-ring. The CuO_2 planes are perpendicular to the ring's symmetry axis. This ring is polished and laser-cut along two planes which varies both L_a and L_c. (c) Photograph of an *a*-ring with two cut planes. L_c^{eff} defines the effective aspect ratio in the bottleneck region. (d) Magnetization m^a of *a*-rings with variable L_a. The apparent stiffness vanishing temperatures are denoted by $\widetilde{T}_c^{\perp}(L_a)$. (e) Magnetization m^c of *c*-rings. Except for the narrowest sample $L_a = 0.09$ (which is suspected of containing a traversing cut), the magnetizations near their transition are insensitive to L_a. The tail of width $(\delta T_c^{\parallel})_{\mathrm{dis}} \simeq 0.5\,\mathrm{K}$ is assumed to reflect some layer-correlated disorder, which is a smaller effect than the finite size dependence of the *a*-rings' $\widetilde{T}_c^{\perp}$. $\bar{T}_c^{\parallel}$ is averaged in-plane transition temperature (see Section 5.6 and Appendix 5.8).

As $T \to T_{\rm c}$, the AB flux in the coil is under screened as $\lambda_\alpha(T) \geq L_\alpha$. In this temperature regime $m^\alpha(T)$ decreases rapidly and becomes linearly proportional to the in-plane stiffness components. As an example, for the geometry of a perfect ring

$$\begin{aligned} m^{a,c}(T) &= h \int_{r_{\rm in}}^{r_{\rm out}} dr\, \pi r^2\ (\hat{\boldsymbol{r}} \times \boldsymbol{j}_{\rm sc}(r))^{a,c} \\ &= -h(r_{\rm out}^2 - r_{\rm in}^2)\ \frac{\Phi}{4}\, \rho^{\perp,\parallel}(T) \quad . \end{aligned} \tag{5.1}$$

h, $r_{\rm in}$, and $r_{\rm out}$ are the ring's height, and inner and outer radii, and Φ is the flux produced by the coil. For irregular rings extracting $\rho^\perp, \rho^\parallel$ from $m^\alpha(T)$ requires a full solution of Ginzburg-Landau and Biot-Savart equations (16). However, here we do not require the magnitude of $\rho^\perp, \rho^\parallel$ but only their vanishing temperatures ${T_{\rm c}}^\perp$ and ${T_{\rm c}}^\parallel$. These are experimentally determined by the vanishing of the corresponding magnetizations.

Figs. 5.2(d,e) depict the temperature-dependent relative magnetizations $m^\alpha(T, L_a)/\, m^\alpha_{\rm max}$, for $\alpha = a, c$. $m^\alpha_{\rm max}$ is the zero temperature magnetization of the largest ring. Fig. 5.2(d) shows a strong dependence of the a-ring's magnetization apparent vanishing temperature $\tilde{T}_{\rm c}^\perp$ on the transverse width L_a. In contrast, the c-rings' magnetization in Fig. 5.2(e), exhibit insensitivity to the sample widths in the ranges $L_a \in [1.05, 0.23]$ and $L_c \in [0.67, 0.19]$. We note an exception of the $(L_a, L_c) = (0.09, 019)$ mm sample, which we believe to be damaged by a deep fracture during the cutting process.

We note that the c-ring magnetizations exhibit a high temperature tail of $\simeq 0.5\,$K above the extrapolated transition at $\bar{T}_{\rm c}^\parallel$. This is attributed to layer-correlated inhomogeneity as discussed in the Introduction and Appendix 5.8. This inhomogeneous broadening will be taken into account in fitting theory to the experimental data in Section 5.6.

5.3 Layered 3dXY model

As mentioned before, we model the phase fluctuations of $La_{1.83}Sr_{0.17}CuO_4$ near $T_{\rm c}$ by the classical 3dXY Hamiltonian on a tetragonal lattice,

$$H_{3dXY} = -\sum_i \sum_\gamma J_\gamma \cos(\varphi_{\boldsymbol{r}_i} - \varphi_{\boldsymbol{r}_i + \boldsymbol{a}_\gamma}) \quad , \tag{5.2}$$

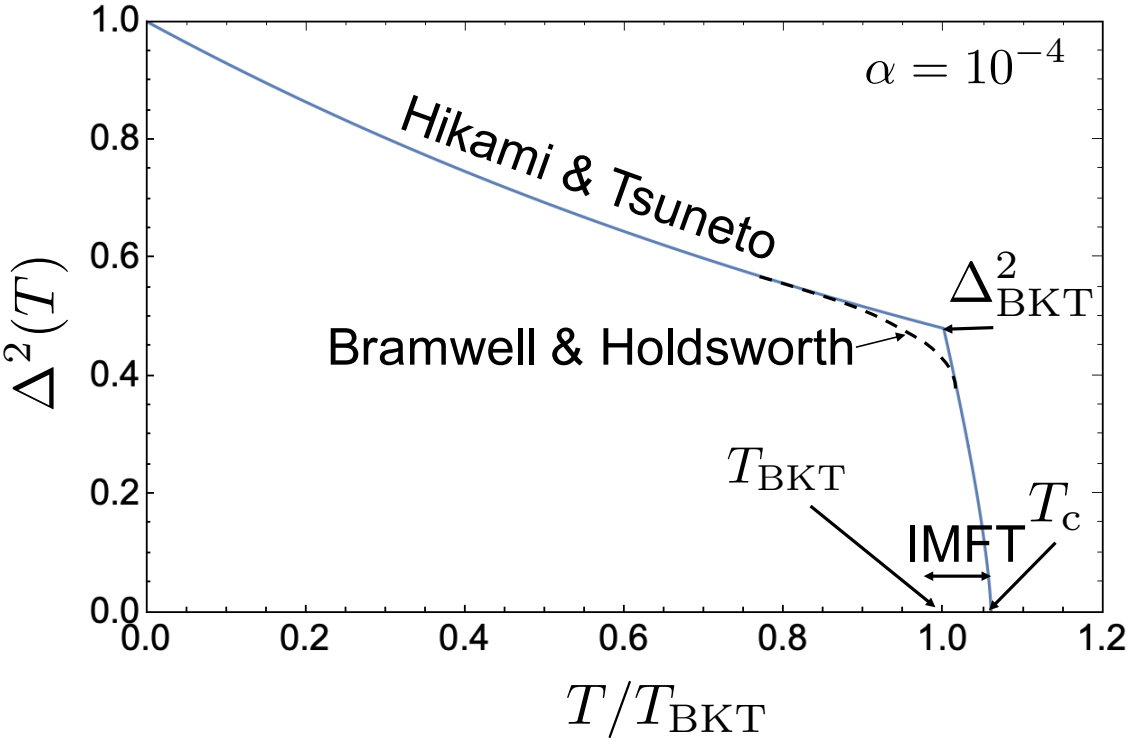

Figure 5.3: The order parameter squared as a function of temperature for the layered classical XY model, for anisotropy parameter $\alpha = 10^{-4}$. The graph patches the linear spinwave theory of Hikami and Tsuneto (22), the crossover (dashed line) power law of Bramwell and Holdsworth (19), and the three dimensional critical point which is obtained by Inter-plane Mean Field Theory (IMFT) of Eqs. (5.15), (5.4) and (5.5).

where $\gamma \in \{a, b, c\}$ and where $J_a = J_b = J^{\parallel}$ and $J_c = J^{\perp}$ are the effective intra- and inter-plane Josephson couplings. The effective anisotropy parameter is defined as $\alpha = J^{\perp}/J^{\parallel}$. α will later be determined to fit experimental data near $T_{\rm c}$. The two dimensional limit $\alpha = 0$ reduces to the two dimensional XY (2DXY) model, where by Mermin and Wagner theorem the superconducting order parameter $\Delta = \langle e^{i\varphi} \rangle$, and $\rho^{\perp}$ vanish at all temperatures. Nevertheless, the in-plane stiffness is non-zero below $T_{\rm BKT} \simeq 0.893 J_a$.

For small but finite anisotropy $0 < \alpha \ll 1$, inter-layer mean field theory (IMFT) is very useful (17; 18; 19; 20; 13). It predicts $\Delta(T) > 0$ for $T < T_{\rm c}$, where $T_{\rm c}$ is the three dimensional critical temperature. IMFT uses the exponential divergence of the BKT susceptibility above $T_{\rm BKT}$ to obtain,

$$\frac{T_{\rm c}(\alpha) - T_{\rm BKT}}{T_{\rm BKT}} = \left(\frac{b}{|\ln(0.14\alpha)|} \right)^2 \quad . \tag{5.3}$$

Here, the (non universal) constant is taken to be $b = 2.725$ (21).

In the regime $[0, T_{\rm BKT}]$, the order parameter magnitude $\Delta = |\langle e^{i\varphi} \rangle|$ decreases from

unity as calculated by Hikami and Tsuneto (22),

$$\Delta^2(T)_{T\leq T_{\rm BKT}} \simeq \exp\left(-\frac{T\,\log(1/\alpha)}{4\pi J_a}\right) \quad . \tag{5.4}$$

Over the crossover regime $T \in [T_{\rm BKT}, T_{\rm c}]$, the order parameter squared initially crosses over with an intermediate power law of $|T-T^*|^{0.46}$, where $T^* = T_{\rm BKT} + \frac{1}{4}(T_{\rm c} - T_{\rm BKT})$ (19), above which it drops precipitously toward $T_{\rm c}$ as,

$$\Delta^2(T) = \Delta^2_{\rm BKT}\, t^{2\beta} \quad , \quad t \equiv \left(\frac{T_{\rm c}-T}{T_{\rm c}-T_{\rm BKT}}\right) \quad , \tag{5.5}$$

where β crosses over from the mean field value $\frac{1}{2}$ to the 3dXY exponent 0.349, within a narrow three dimensional Ginzburg critical region of width $T_{\rm c}/\log^4(\alpha)$ (13).

Fig. 5.3 depicts the smoothed "trapezoidal" temperature dependence of Δ^2 which differs from the BCS theory for the gap squared. We note that the spectral gaps observed by photoemission do not directly measure the thermodynamic order parameter. In the underdoped pseudogap phase(23), parts of the Fermi surface gap survives above $T_{\rm c}$ (24; 25). A more direct measurement of Δ^2 near $T_{\rm c}$ would be the superconducting stiffness (1; 13), since

$$\rho_\gamma(T) \propto \Delta^{2-\eta\nu\beta^{-1}} \tag{5.6}$$

where η and ν are the critical correlation function power law and correlation length exponents respectively. For the 3dXY model $\eta\nu = 0.0255$ which is small and henceforth neglected.

5.4 Monte Carlo simulations

The superfluid stiffness (*i.e.* helicity modulus) of Eq. 5.2 with $a_\gamma = 1$, is given by (26; 7)

$$\begin{aligned}\rho_\gamma = \frac{J_\gamma}{V}\left\langle \sum_{\langle ij\rangle} \cos\big(\varphi_{\boldsymbol{r}_i} - \varphi_{\boldsymbol{r}_j}\big)\,(r_i^\gamma - r_j^\gamma)^2 \right\rangle \\ - \frac{J_\gamma^2}{VT}\left\langle \Big(\sum_{\langle ij\rangle} \sin\big(\varphi_{\boldsymbol{r}_i} - \varphi_{\boldsymbol{r}_j}\big)\,(r_i^\gamma - r_j^\gamma)\Big)^2 \right\rangle \quad , \gamma = a,b,c.\end{aligned} \tag{5.7}$$

$V = L_a L_b L_c$. The first contribution measures the short range correlations, which are proportional to minus the energy along the bonds in the γ direction. The second contribution

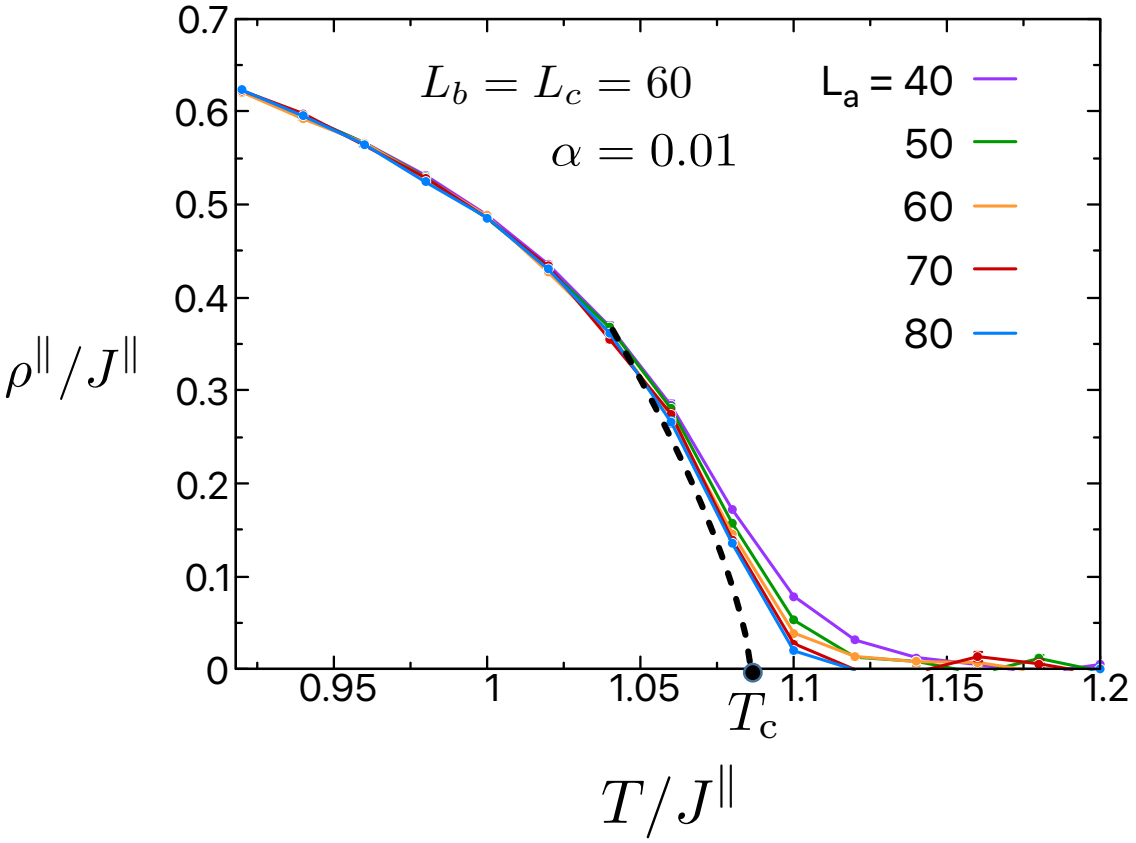

Figure 5.4: The intra-plane stiffness $\rho^{\parallel}$, plotted as a function of temperature T, for $\alpha = 0.01$ and for different L_a between 40 and 80, while L_b and L_c are kept fixed at 60. The error bars are smaller than the point sizes. The black dashed line shows the critical behavior near the thermodynamic transition temperature T_c, according to Eq. (5.6).

measures long range current fluctuations, which vanish at zero temperature, and reduce the stiffness at finite temperatures.

We compute Eq. (5.7) by a Monte Carlo (MC) simulation of H_{3dXY} with the Wolff cluster updates algorithm (27), see Appendix 5.11 for details. We choose $L_c = L_b = 60$, and vary the width in the range $L_a \in \{40, 50, \ldots, 80\}$ using the anisotropy parameters in the range $\alpha = 0.01 - 0.02$. The minimal accessible anistropy parameter is determined by the maximal lattice size.

In Fig. 5.4, we plot the intra-plane stiffness $\rho^{\parallel}$ as a function of temperature T, and width L_a. The ansitropy parameter is fixed at $\alpha = 0.01$. $T_c \simeq 1.086$. The expected thermodynamic critical behavior, Eq. (5.6), is depicted by a dashed line in Fig. 5.4. For the disorder-free model, the tail above T_c indicates that the in-plane correlation length exceeds L_a. Thus, a larger L_a reduces the width of the tail. For millimeter scale superconducting rings, this tail should be unobservably small.

In Fig. 5.5, the MC data for $\rho^{\perp}(T)$ are shown as points. Given a numerical resolution threshold ε, $\rho^{\perp}(T)$ appears to vanish at transition temperatures $\widetilde{T}_c^{\perp}$ which depend on ε

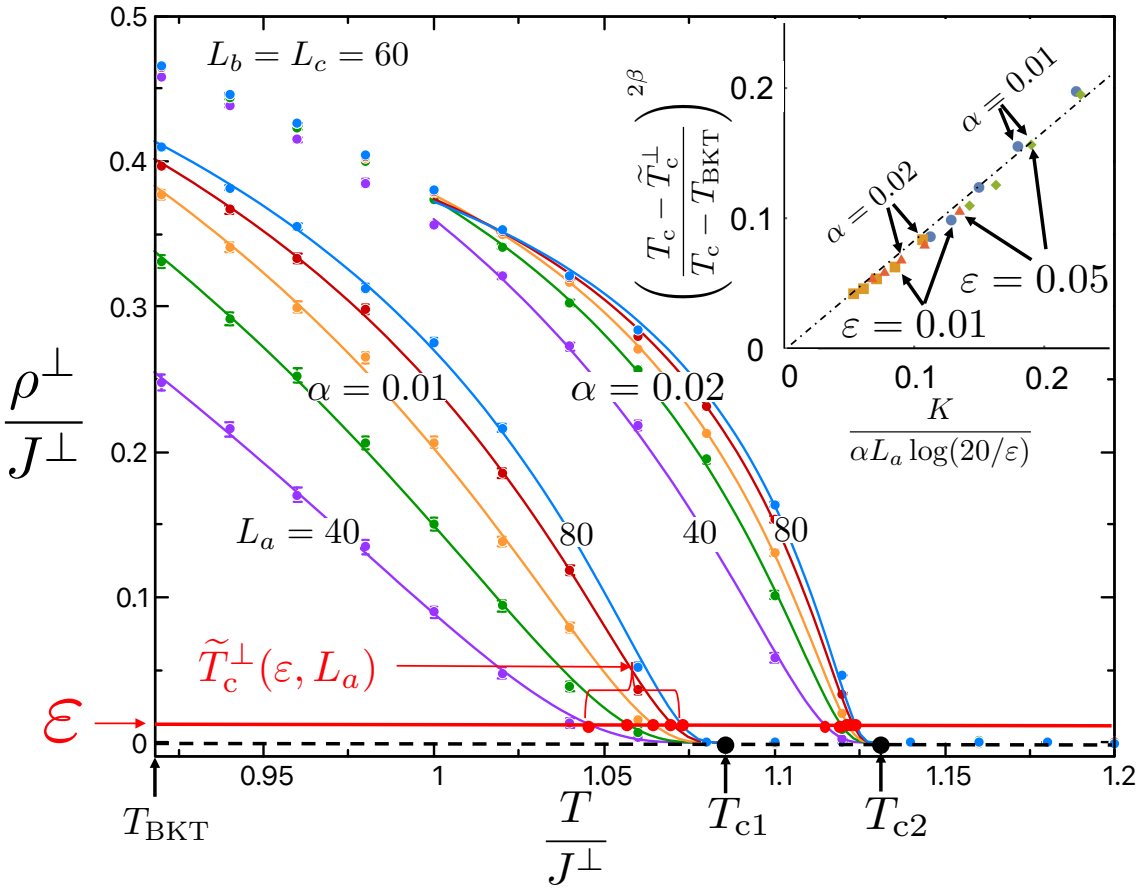

Figure 5.5: MC evaluations of $\rho^{\perp}$ for the clean 3dXY model Eq. (5.2), a function of temperature for a range of sample widths $L_a \in \{40, 50, \ldots, 80\}$, and anisotropy parameters α. The thermodynamic critical temperatures are evaluated as $T_{c1} = 1.086 J_a$ and $T_{c2} = 1.13 J_a$ for $\alpha = 0.01$ and 0.02, respectively. Solid lines are best fits to Eq. (5.12). ε is arbitrarily chosen as the numerical resolution which defines the apparent transition temperatures $\widetilde{T}_c^{\perp}$ by Eq. (5.14). Inset: Verification of Eq. (5.15) by collapse of all the temperature shifts for various L_a, ε, α obtained from the main graphs.

and the width L_a. The solid lines and the inset describe a fit of the MC data to analytic formulas derived in the following Section.

5.5 Crossover to one dimensional Josephson array

The *apparent* premature vanishing of $\rho^{\perp}$ in a finite size sample of an approximately unit aspect ratio, is due to its crossover to a quasi one-dimensional behavior as $T \to T_{\rm c}$. The stiffness of a one dimensional (1d) classical XY chain with inter-site coupling $J_{\rm 1d}$, lattice constant a and chain length L is,

$$\begin{aligned} \rho_{\rm 1d}(T,L) &= TLZ_2/Z_0 \\ Z_{2p} &= \sum_{n=-\infty}^{\infty} \left(\frac{I_n(J_{\rm 1d}/T)}{I_0(J_{\rm 1d}/T)} \right)^{L/a} n^{2p}, \end{aligned} \tag{5.8}$$

where I_n are modified Bessel functions and $p = 0, 1$. Luttinger liquid (LL) theory (28; 8), which applies at $L \gg a$, yields an analytic result where $\rho_{\rm 1d}$ depends on the dimensionless variable $x \equiv LT/(J_{\rm 1d}\, a)$ as,

$$\begin{aligned} \rho_{\rm LL}(J_{\rm 1d}, x) &= J_{\rm 1d}\, a \left(1 - \frac{\pi^2}{x} \frac{\vartheta_3''(0, e^{-2\pi^2/x})}{\vartheta_3(0, e^{-2\pi^2/x})} \right) \\ &\simeq J_{\rm 1d}\, a \begin{cases} 1 & (x \le 2) \\ 20\, \exp(-0.472\, x) & (x \ge 10) \end{cases}, \end{aligned} \tag{5.9}$$

where $\vartheta_3(z,q) = 1 + 2\sum_{n=1}^{\infty} q^{n^2} \cos(2nz)$, and prime denotes differentiation with respect to z. Comparison between Eqs. (5.8) and (5.9) is shown in Appendix 5.9.

Now we return to the c-axis stiffness $\rho^{\perp}$ of the layered model (5.2), which can be described as a chain of Josephson junctions along the c-axis with inter-grain coupling,

$$J_{\rm eff}(T) \;=\; \frac{L_a L_b}{(\xi^{\parallel})^2} \times J^{\perp} \Delta^2(T), \tag{5.10}$$

Toward $T_{\rm c}$, $\Delta^2(T)$ vanishes as $t^{2\beta}$ by Eq. (5.5). Substituting $J_{\rm 1d} = J_{\rm eff}(T)$ we expect the asymptotic behavior of Eq. (5.9) to be realized after replacing

$$x \to \frac{L_c T}{J_{\rm eff}(T)\, \xi^{\perp}}. \tag{5.11}$$

Thus for $t \ll 1$, $x \gg 1$ and

$$\rho^{\perp}(T) \approx 20\,\rho^{\perp}(T_{\rm BKT}) \exp\left(-\frac{K}{\alpha L_a}\, t^{-2\beta}\right) \quad , \tag{5.12}$$

$$K \simeq \frac{0.472\, r T_{\rm c}\, (\xi^{\parallel})^2}{J_a\, \Delta_{\rm BKT}^2\, \xi^{\perp}} \quad . \tag{5.13}$$

For any experimental resolution ε, an apparent vanishing temperature $\widetilde{T}_{\rm c}^{\perp}(\varepsilon)$ is defined by the threshold condition,

$$\frac{\rho^{\perp}(\widetilde{T}_{\rm c}^{\perp})}{\rho^{\perp}(T_{\rm BKT})} = \varepsilon. \tag{5.14}$$

By Eq. (5.12), the apparent width dependent transition temperature is,

$$T_{\rm c} - \widetilde{T}_{\rm c}^{\perp} = (T_{\rm c} - T_{\rm BKT}) \left(\frac{K}{\alpha L_a \log(20/\varepsilon)}\right)^{1/2\beta} \tag{5.15}$$

The most important consequence of the quasi one-dimensional behavior, is that the temperature shifts are proportional to $(\alpha L_a)^{-1/2\beta}$. This is a much larger shift than expected from critical fluctuations, which are of order $(\alpha L_a^2)^{-1}$.

In the inset of Fig. 5.5 we verify the validity of Eq. (5.15) by collapsing of all the temperature shifts onto a straight line. The slope of this line differs only by 20% from unity, which we attribute to the choice of the (non-universal) constants in the asymptotic expression of Eq. (5.9).

5.6 Comparison of Theory to Experiments

In comparing Eq. 5.15 to the MC results, we have used the 3dXY critical exponent $\beta = 0.349$.

For the experimental $La_{1.83}Sr_{0.17}CuO_4$ crystals, the millimeter width corresponds to $\sim 10^5$ effective lattice constants, and the anistropy parameter will turn out to be $\alpha < 10^{-4}$, which yields an unobservable narrow Ginsburg critical region. Hence we shall fit the Eq. 5.15 with the mean field exponent $\beta = 0.5$.

The a-ring is sequentially cut such that the induced current is governed by the bottleneck region. There, the induced current flows along the c axis over an effective length of $L_c^{\rm eff} = 2$ mm. The transverse dimension $L_b = 0.46$ mm yields $r = 4.34$. The width is

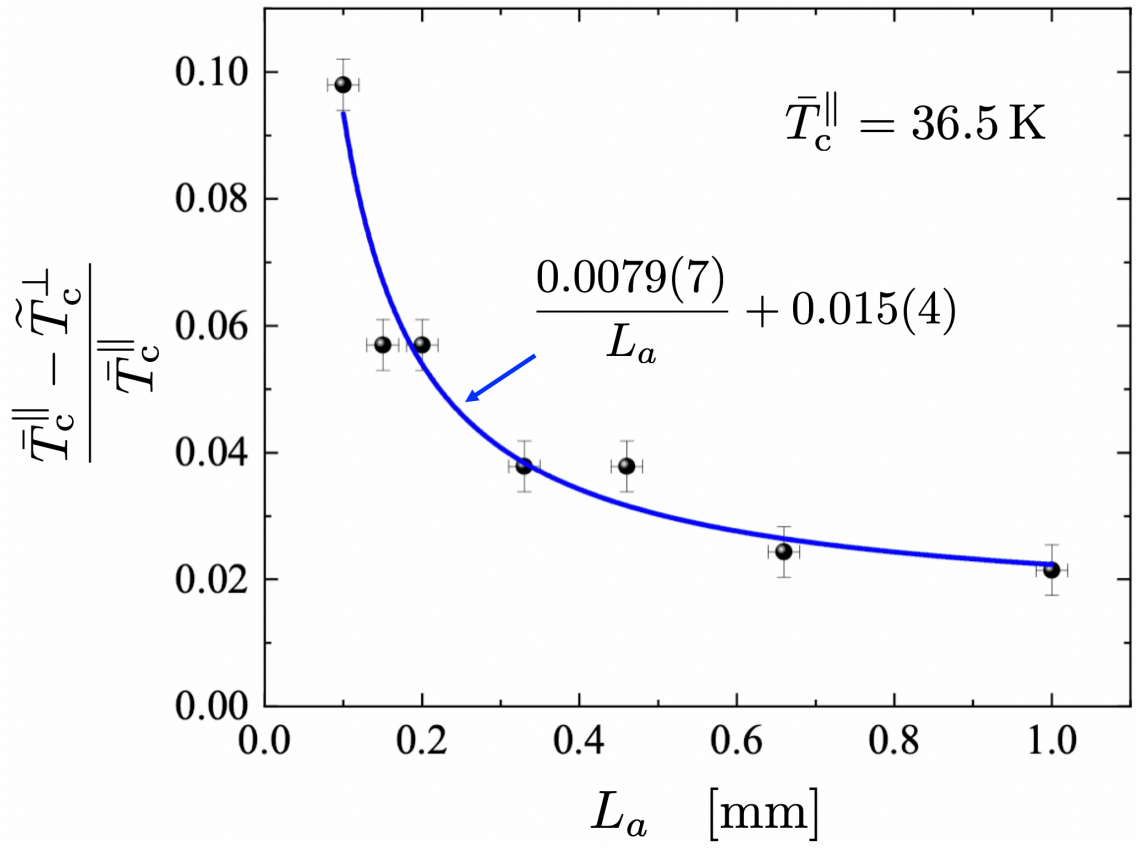

Figure 5.6: Comparison of experimental results for $La_{1.83}Sr_{0.17}CuO_4$ rings of Fig. 5.2 and theoretical prediction of Eqs. (5.15) and (5.19). Crosses: The apparent c-axis transition temperature shifts $\widetilde{T}_c^{\perp}$ of the a-rings, as determined in Fig. 5.2(d). L_a are the bottleneck widths of the ab planes. Line: the least square fit using $\alpha^{\mathrm{fit}} = 4.1 \times 10^{-5}$. The offset of the reduced temperature 0.015(4) agrees with the estimated layer-correlated disorder (see text). We use the mean field exponent $\beta = \frac{1}{2}$, due to the narrow Ginzburg critical regime near T_c.

varied in the range $L_a \in [0.1, 1]$ mm. We estimate the experimental resolution at $\varepsilon = 10^{-2}$. (High accuracy of ε is not essential, since $\widetilde{T}_c^{\perp}$ depends on it logarithmically).

At zero temperature the coherence lengths have been determined experimentally (24) to be $\xi^{\parallel}(0) \simeq 3\,\mathrm{nm}$ and $\xi^{\perp}(0) \simeq 1.3\,\mathrm{nm}$. The in-plane lattice constant for the effective 3dXY model is the coherence length estimated at T_{BKT} to be $\xi^{\parallel}(T_{\mathrm{BKT}}) = \xi^{\parallel}(0)/\Delta_{\mathrm{BKT}}$. Due to the incoherent single-electron tunneling between the layers, we assume that the Cooper pair size in the c direction remains confined to a single plane $\xi^{\perp}(T_{\mathrm{BKT}}) \simeq \xi^{\perp}(0)$.

In Fig. 5.6, the apparent c-axis transition temperatures $\widetilde{T}_c^{\perp}(L_a)$ are plotted. The data is somewhat noisy, presumably because of the introduction of deep cuts during the ring's cutting process, which are eliminated by subsequent cuts. The two-parameter fit function is plotted,

$$\frac{\bar{T}_c^{\parallel} - \widetilde{T}_c^{\perp}}{\bar{T}_c^{\parallel}} = \frac{A}{L_a[\mathrm{mm}]} + (\delta t)_{\mathrm{dis}} \tag{5.16}$$

with $A = 0.0079$ and $(\delta t)_{\mathrm{dis}} = 0.015(4)$. The dimensionless temperature shift $(\delta t)_{\mathrm{dis}}$ is understood as the effect of layer-correlated inhomogeneity (see Appendix 5.8). We use the high temperature tail of magnitude $(\delta T_c^{\parallel})_{\mathrm{dis}} \simeq 0.5\,\mathrm{K}$, which is depicted in Fig. 5.2(e). Subtracting $(\delta T_c^{\parallel})_{\mathrm{dis}}$ from $\bar{T}_c^{\parallel} = 36.5\,\mathrm{K}$ yields a bound for $\widetilde{T}_c^{\perp}$ for wide samples,

$$\lim_{L_a \to \infty} \widetilde{T}_c^{\perp} = \bar{T}_c^{\parallel} - (\delta T_c^{\parallel})_{\mathrm{dis}} = 36\,\mathrm{K}. \tag{5.17}$$

The estimated layer-correlated disorder shift is consistent with the fit in Fig. 5.6,

$$(\delta t)_{\mathrm{dis}} \equiv \frac{(\delta T_c^{\parallel})_{\mathrm{dis}}}{T_c^{\parallel}} \in 0.015(4). \tag{5.18}$$

Using Eqs. (5.15), (5.4), (5.13) and (5.15), and the parameters listed above we obtain

$$A = \Delta T_c(\alpha) \frac{0.472 \times 10^{-6}\, r\, T_c\, (\xi^{\parallel})^2}{\alpha\, \Delta_{\mathrm{BKT}}^4(\alpha)\, \xi^{\perp} \log(20/\varepsilon)} = 0.0079 \tag{5.19}$$

which can be fit by the anisotropy parameter,

$$\alpha^{\mathrm{fit}}(T \simeq T_c) = 4.1 \times 10^{-5} \tag{5.20}$$

5.7 Discussion and Summary

The experimental conundrum, which was first noted in Ref. (3), was that stiffness measurements of a-rings and c-rings, cut out from same cuprate crystal, exhibited different transition temperatures. In this paper, we have shown that this difference cannot be fully explained by layer-correlated disorder, since it varies consistently with the layer's width, which is not coupled to the distribution of layer-correlated disorder.

With the help of Monte-Carlo simulations, inter-layer mean field theory, we have identified a narrow regime below the bulk transition temperature $T_{\rm c}$ where the inter-layer stiffness of finite size samples crosses over to an effective one dimensional Josephson array behavior. As a result, we resolve the conundrum, and explain the Monte-Carlo data, as a width-dependent, *apparent* reduction of the c-axis $T_{\rm c}$. The visibility of the effect depends on the smallness of the anisotropy parameter α.

We note that $\alpha^{\rm fit}$ parametrizes the effective Hamiltonian near $T_{\rm c}$. We compare it to the zero temperature anisotropy parameter reported for optimally doped $La_{2-x}Sr_xCuO_4$ (for $Sr_{0.15}$) in Ref. (30),

$$\alpha^{\lambda}(T=0) = \left(\frac{\lambda_c}{\lambda_a}\right)^{-2} = 4.6 \times 10^{-3}. \tag{5.21}$$

The difference in anisotropy can be attributed to the reduction of inter-plane coherence due to thermally excited nodal quasiparticles of the d-wave superconductor and the effects of inter-planar vortex rings above the two dimensional $T_{\rm BKT}$.

Analog in ^{4}He – We have seen that $\alpha \ll 1$ can be mapped onto an isotropic model on samples with large aspect ratio. A similar "premature" vanishing of $\rho^{\perp}$ has been observed on a quasi-one dimensional brick, *i.e.* $L_a \ll L_c$ (7). This result was used to explain the experimental disappearance of superfluid density of ^{4}He embedded in quasi one-dimensional nanopores (31; 32). Here we explain the *apparent* reduction of $\widetilde{T}_{\rm c}(L_a)$, not as a true thermodynamic transition but rather as a consequence of an essential singularity decay of $\rho^{\perp}$ toward the thermodynamic $T_{\rm c}$.

In general, layered superconductors with very high anisotropy are expected to exhibit such apparent differences between transition temperatures of in-plane and out of plane persistent currents. For example, an emergent anisotropy of layered superconductors has been an important consequence of certain pair density wave (PDW) ordering (33). We

propose that the dependence of inter-layer stiffness transition temperatures on sample width cold help characterize the emergent anisotropy parameter of that interesting PDW phase.

Acknowledgments

A.S. and I.M. contributed equally to this work. We thank Erez Berg, Snir Gazit, Dror Orgad, and Daniel Podolsky for beneficial discussions.

Funding information

A.A. acknowledges the Israel Science Foundation (ISF) Grant No. 2081/20. A.K. acknowledges the ISF Grant. No. 1251/19 and 3875/21. This work was performed in part at the Aspen Center for Physics, which is supported by National Science Foundation grant PHY-2210452, and at the Kavli Institute for Theoretical Physics, supported by Grant Nos. NSF PHY-1748958, NSF PHY-1748958 and NSF PHY-2309135.

5.8 Planar correlated disorder

Refs. (5; 6) have considered the layered XY model where the ab planes exhibit a variable z-dependent stiffness $\rho^{\parallel}(z)$ for $z \in [0, L_c]$. We can see the effects of bounded correlated disorder on superconductors with a variation of $\rho^{\parallel}(z)$ along the c-axis. In each segment, the stiffness temperature dependence has a different $T_{\rm c}$,

$$\rho^{\parallel}(T) = \rho^{\parallel}(0) \left| \frac{T - T_{\rm c}^{\parallel}(z)}{\bar{T}_{\rm c}^{\parallel}} \right|^{2\beta - \eta\nu} \tag{5.22}$$

where $T_{\rm c}^{\parallel}(z) \propto \rho^{\parallel}(z, 0)$ is the local transition temperature whose average is defined as $T_{\rm c}^{\parallel}$ and maximal variation is $(\delta T_{\rm c}^{\parallel})_{\rm dis}$. The global ab-stiffness is given by the integral

$$\rho^{\parallel} = \rho^{\parallel}(0) \int_0^{L_c} \frac{dz}{L_c} \left| \frac{T - T_{\rm c}^{\parallel}(z)}{\bar{T}_{\rm c}^{\parallel}} \right|^{2\beta - \eta\mu} \quad , \tag{5.23}$$

which smears the average critical temperature $\bar{T}_{\rm c}^{\parallel}$ by a high temperature tail at $T \in \left[\bar{T}_{\rm c}^{\parallel}, \bar{T}_{\rm c}^{\parallel} + (\delta T_{\rm c}^{\parallel})_{\rm dis}\right]$.

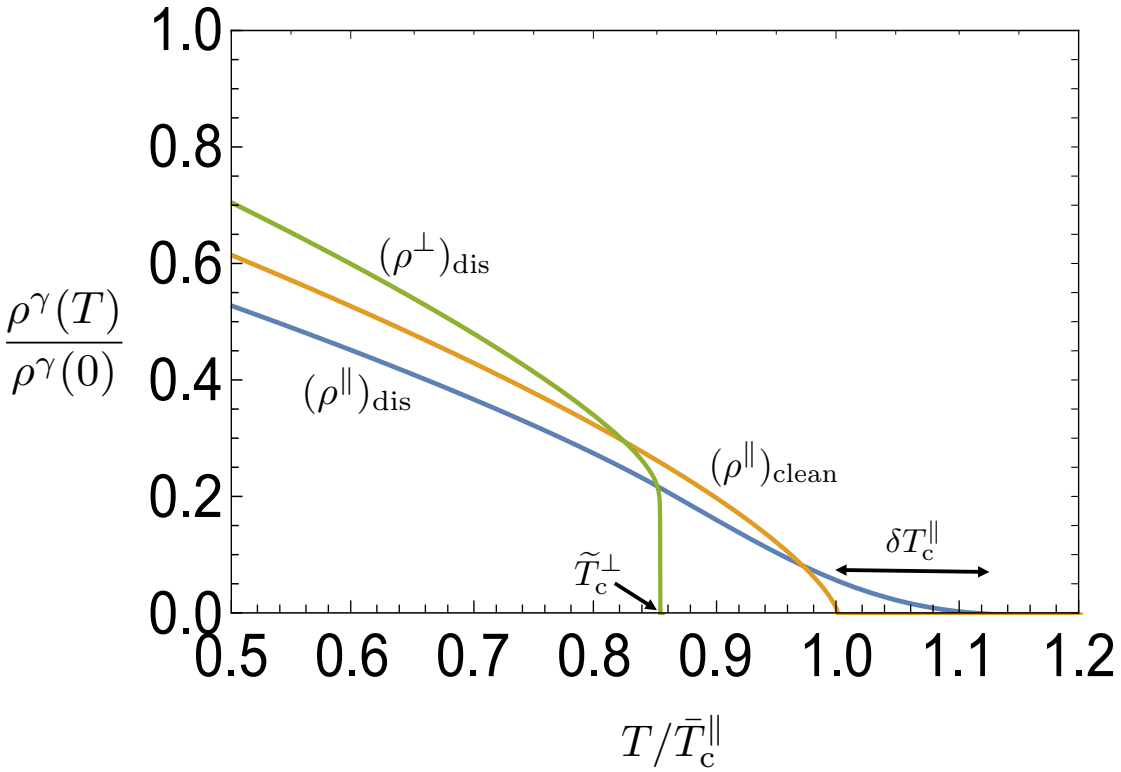

Figure 5.7: Effects of planar-correlated disordered, modelled by c-axis dependent in-plane stiffness $\rho^\parallel(z)$, with an average transition temperature $\bar{T}_{\rm c}^\parallel$ and a width of transition temperatures $(\delta T_{\rm c}^\parallel)_{\rm dis} = 0.1\bar{T}_{\rm c}^\parallel$. Orange line: The clean system with a three dimensional critical behavior. Blue line: the global $\rho^\parallel$ showing a disorder induced high temperature tail above $\bar{T}_{\rm c}^\parallel$. Green line: the global $\rho_\perp^{\rm dis}$, which is dominated by the weakest interplane stiffnesses, and vanishes below $T_{\rm c}^\parallel$.

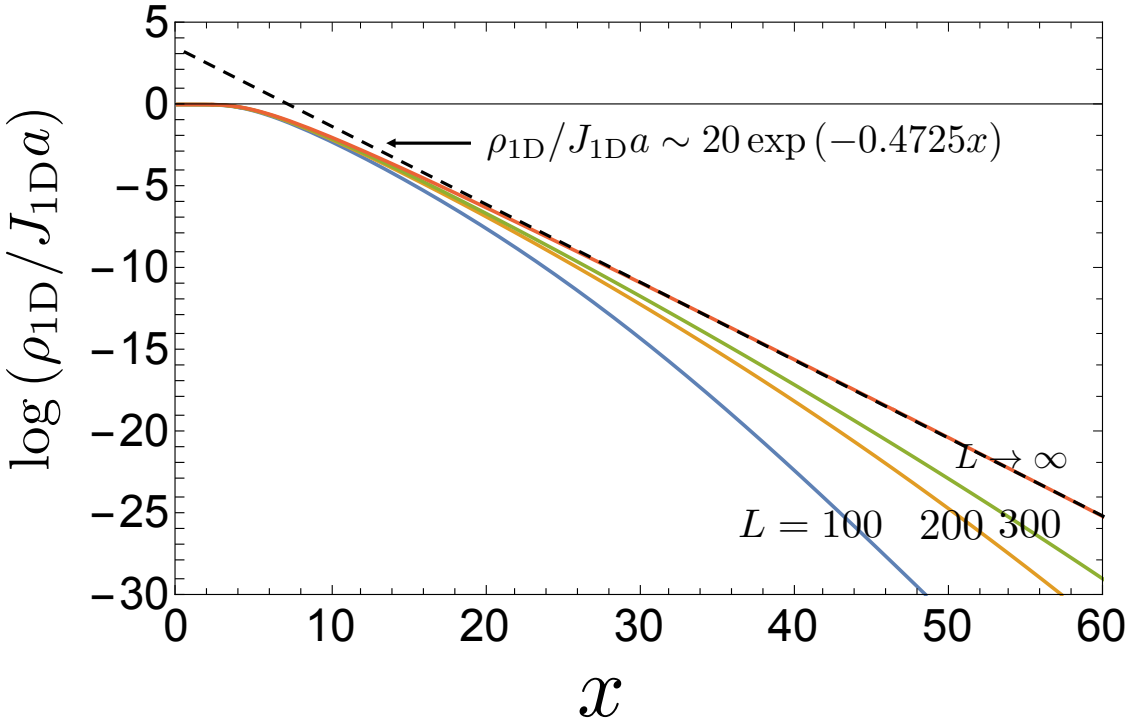

Figure 5.8: Stiffness as a function of scaled variable $x = LT/(J_{1d}a)$ in the one dimensional XY model for different lengths L as given by the exact result of Eq. (7), and asymptotically at $L \to \infty$ by Eq. (8) of the main text.

In contrast, the c-axis stiffness $\rho^{\perp}(z)/\rho^{\perp}(0)$ is proportional to the local order parameter squared $\Delta(z) \propto |T - T_c(z)|^{\beta}$. The global c-axis stiffness is the harmonic average given by,

$$\rho^{\perp} = \rho^{\perp}(0) \left(\int_0^{L_c} \frac{dz}{L_c} \frac{(\bar{T}_c^{\parallel})^{2\beta}}{|T - T_c^{\parallel}(z)|^{2\beta}} \right)^{-1} \quad . \tag{5.24}$$

The weakest segment, with the lowest $\rho^{\perp}(z)$, dominates the integral. The temperatures where the order parameter of this segment vanishes is

$$\widetilde{T}_c^{\perp} \leq \bar{T}_c^{\parallel} - (\delta T_c^{\parallel})_{\rm dis} \quad , \tag{5.25}$$

above which the global $\rho^{\perp}(T)$ disappears. The effect of bounded layer-correlated disorder is demonstrated in Fig. 5.7.

5.9 Asymptotic behavior of stiffness of a one dimensional XY chain

In Fig. 5.8 we depict the exact result of the stiffness of the one dimensional XY chain as given by Eq. (7) of the main text. At large L/a the graphs show convergence to the

analytic Luttinger-Liquid form (28; 8), which at large x is given by Eq. (8) of the main text.

5.10 Estimation of finite size shift in $T_{\rm c}$

Fine size scaling produce unobservably small finite size shifts of $T_{\rm c}$ for millimeter size samples, as shown by the following. The correlation lengths above $T_{\rm BKT}$ diverge as

$$\xi^{\parallel}(t) \simeq \frac{1}{\sqrt{\alpha}} \xi_a^{(0)} t^{-\nu} \quad , \quad \xi^{\perp}(t) \simeq \xi_c^{(0)} t^{-\nu} \tag{5.26}$$

where we use the Ginzburg-Landau definition of correlation lengths, $\xi_\gamma^{-1} \propto \sqrt{\rho_\gamma}$, to obtain the factor of $\sqrt{\alpha}$ between the divergent correlation length.

For Eq. (5.2) with sample dimensions $L_\gamma, \gamma = a, b, c$ the stiffness components near $T_{\rm c}$ vanish as (34),

$$\frac{\rho_c}{\rho_c(T_{\rm BKT})} = t^v \, \Phi[x_a] \quad , \quad x_a = \xi_a(t)/L_a. \tag{5.27}$$

where $\Phi(x)$ is differentiable function with a finite value at $x = 0$. We expand Φ to linear order in ξ_a and set $\rho^{\perp} \to 0$ to obtain,

$$0 = \Phi_0 + \partial_{x_a} \Phi \times \left(\frac{t^{-\nu} \xi_a^{(0)}}{\sqrt{\alpha} L_a} \right) + \mathcal{O}(x_a^2) \tag{5.28}$$

which is solved by a positive shift of $T_{\rm c}$ by the amount

$$\delta t \simeq - \frac{\Phi_0}{\partial_a \Phi_\gamma} \left(\frac{\sqrt{\alpha} L_a}{\xi_a^{(0)}} \right)^{-1/\nu} \quad . \tag{5.29}$$

For the experimental $La_{1.83}Sr_{0.17}CuO_4$ rings, taking $\alpha = 10^{-5}$, $L_a/\xi_a^{(0)} \sim 10^6$, yields $|\delta t| \leq 10^{-4}$, which is much below experimental temperature resolution.

5.11 Details of the Monte-Carlo simulations using cluster algorithm

The superfluid stiffness or the helicity modulus (with $a_\gamma = 1$) for the classical Hamiltonian of Eq. (5.2) is given by Eq. (5.7) (26; 7; 35).

In the Wolff-cluster algorithm (27), we assume the XY spins $\boldsymbol{S}$ to be the unit vectors in

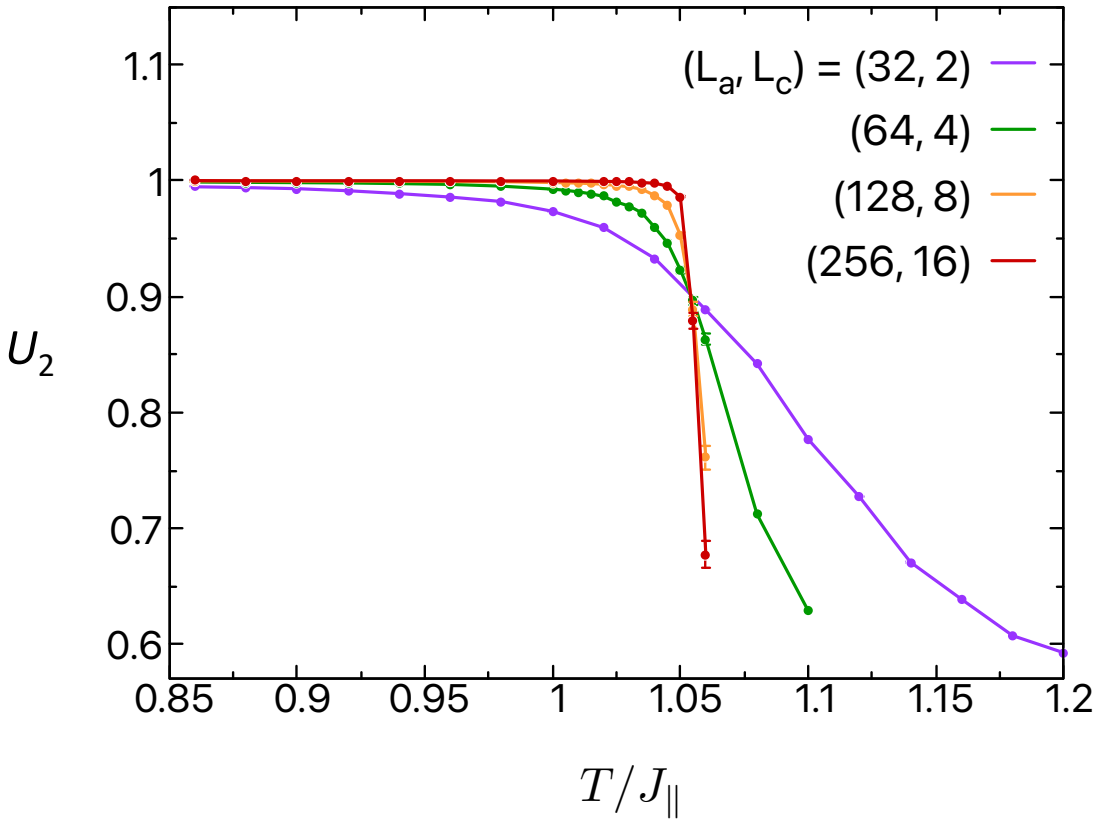

Figure 5.9: Binder cumulant U_2 plotted as a function of temperature T, for anisotropy $\alpha = 0.005$ and for different sizes with a fixed aspect ratio $L_a/L_c = 16$ and $L_b = L_a$.

$\mathbb{R}^3$. In every Monte-Carlo (MC) step, we first choose a random site $\boldsymbol{r} \in \mathbb{R}_3$ and a random direction $\boldsymbol{d} \in S_2$, and consider a reflection of the spin on that site about the hyperplane orthogonal to $\boldsymbol{d}$. Note that this is equivalent to the spin-flipping operation in Ising model. We then travel to all neighboring sites ($\boldsymbol{r}'$) of $\boldsymbol{r}$, and check if the bond $\langle \boldsymbol{r}\boldsymbol{r}' \rangle$ is activated with a probability

$$P_\gamma(\boldsymbol{r}, \boldsymbol{r}') = 1 - \exp\Big(\min\big[0, 2J_\gamma \beta (\boldsymbol{d} \cdot \boldsymbol{S}_{\boldsymbol{r}})(\boldsymbol{d} \cdot \boldsymbol{S}_{\boldsymbol{r}'})\big]\Big), \tag{5.30}$$

where β is the inverse temperature. If this satisfies, we mark $\boldsymbol{r}'$ and include it to a cluster $\mathcal{C}$ of "flipped" spins. We iteratively continue this process for all unmarked neighboring sites of $\boldsymbol{r}'$ and grow the cluster size until all the neighbors turn out to be marked. We use such 10^6 number of MC steps for thermalization, followed by another 10^7 number of MC steps for measurement of different observables, such as the helicity modulus and the binder cumulant. We estimate the errors of different observables by using a standard Jackknife analysis of the MC data.

In Fig. 3 of the main text, we have presented the inter-plane superfluid stiffness $\rho^\perp$ for different system sizes of $L_a \in [60 - 80], L_b = L_c = 60$, near the transition.

Next we calculate the Binder cumulant, defined in terms of the higher powers of magnetization m as following (36)

$$U_2 = \frac{3}{2}\left(1 - \frac{1}{3}\frac{\langle m^4 \rangle}{\langle m^2 \rangle^2}\right), \tag{5.31}$$

and we use it to extract the value of critical temperatures accurately. As an example, in Fig. 5.9, we present U_2 as a function of T, for an anisotropy parameter $\alpha = 0.005$ and for different system sizes with a fixed aspect ratio $L_a = L_b$ and $L_a/L_c = 16$. In the ordered phase when all the spins are aligned it takes a value 1, while in the disordered phase it vanishes and takes an intermediate value between 0 and 1 at the critical point. Therefore, by tracking the crossing between different system sizes, we find a critical temperature $T_c \sim 1.05$ for these parameters. using a similar analysis, we obtain T_c for other anisotropy parameters also, discussed in the main text.

Bibliography

[1] Fisher, Michael E. and Barber, Michael N., & Jasnow, D., 1973, Phys. Rev. A: 8, 1111–1124. doi:10.1103/PhysRevA.8.1111

[2] Hasenbusch, M., 2019, Phys. Rev. B: 100, 224517. doi:10.1103/PhysRevB.100.224517

[3] Kapon, I., Salman, Z., Mangel, I., Prokscha, T., Gavish, N., & Keren, A, 2019, Nat. Comm: 10(1), 2463. doi:10.1038/s41467-019-10480-x

[4] Harris, A. B., 1974, Jour. Phys. C: Sol. State Phys. 7(9), 1671. doi:10.1088/0022-3719/7/9/009

[5] Mohan, P., Goldbart, P. M., Narayanan, R., Toner, J., & Vojta, T., 2010, Phys. Rev. Lett: 105(8), 085301. doi:10.1103/PhysRevLett.105.085301

[6] Pekker, D., Refael, G., & Demler, E., 2010, Phys. Rev. Lett: 105, 085302. doi:10.1103/PhysRevLett.105.085302

[7] Kotani, A., Yamashita, K., & Hirashima, D. S., 2011, Phys. Rev. B: 83, 174515. doi:10.1103/PhysRevB.83.174515

[8] Hirashima, D. S., 2020, Phys. Rev. B: 102(10), 104506. doi:10.1103/PhysRevB.102.104506

[9] Uemura, Y. J., Luke, G. M., Sternlieb, B. J., Brewer, J. H., Carolan, J. F., Hardy, W. N., Kadono, R., Kempton, J. R., Kiefl, R. F., Kreitzman, S. R., Mulhern, P., Riseman, T. M., Williams, D. Ll., Yang, B. X., Uchida, S., Takagi, H., Gopalakrishnan, J., Sleight, A. W., Subramanian, M. A., Chien, C. L., Cieplak, M. Z., Xiao, G., Lee, V. Y., Statt, B. W., Stronach, C. E., Kossler, W. J., & Yu, X. H., 1989, Phys. Rev. Lett: 62, 2317. doi:10.1103/PhysRevLett.62.2317

[10] Hetel, I., Lemberger, T. R., & Randeria, M., 2007, Nat. Phys.: 3(10), 700. doi:10.1038/nphys707

[11] Emery, V. J., & Kivelson, S. A.,0 1995, Nature: 374 (6521), 434. doi:10.1038/374434a0

[12] Kosterlitz, J. M., & Thouless, D. J., S. A.,0 1973, Jour. Phys. C: Sol. State Phys.: 6(7), 1181. doi:10.1088/0022-3719/6/7/010

[13] Mihlin, A., & Auerbach, A., 2009, Phys. Rev. B: 80, 134521. doi:10.1103/PhysRevB.80.134521

[14] Mangel, I., Kapon, I., Blau, N., Golubkov, K., Gavish, N., & Keren, A., 2020, Phys. Rev. B: 102(2), 024502. doi:10.1103/PhysRevB.102.024502

[15] Marin, C., Charvolin, T., Braithwaite, D., & Calemczuk, R., 1999, Physica C: 329, 197. doi:10.1016/S0921-4534(99)00344-5

[16] Gavish, N., Kenneth, O., & Keren, A., 2021, Physica D: Nonlinear Phenomena: 415, 132767. doi:10.1016/j.physd.2020.132767

[17] Scalapino, D. J., Imry, Y., & Pincus, P., 1975, Phys. Rev. B: 11(5) 2042. doi:10.1103/PhysRevB.11.2042

[18] Keimer, B., Aharony, A., Auerbach, A., Birgeneau, R. J., Cassanho, A., Endoh, Y., Erwin, R. W., Kastner, M. A., & Shirane, G., 1992, Phys. Rev. B: 45, 7430. doi:10.1103/PhysRevB.45.7430

[19] Bramwell, S. T., & Holdsworth, P. C. W., 1994, Phys. Rev. B: 49, 8811. doi:10.1103/PhysRevB.49.8811

[20] Butera, P., & Pernici, M., 2009, Phys. Rev. B: 80, 054408. doi:10.1103/PhysRevB.80.054408

[21] Kosterlitz, J. M., 1974, Phys. C: Sol. State Phys.: 7(6), 1046. doi:10.1088/0022-3719/7/6/005

[22] Hikami, S., & Tsuneto, T., 1980, Prog. Theor. Phys.: 63(2), 387. doi:10.1143/PTP.63.387

[23] Hüfner, S., Hossain, M.A., Damascelli, A., & Sawatzky, G.A., 2008, Reports on Progress in Physics: 71(6), 062501. doi:10.1088/0034-4885/71/6/062501

[24] Lee, W.S., Vishik, I.M., Tanaka, K., Lu, D.H., Sasagawa, T., Nagaosa, N., Devereaux, T.P., Hussain, Z., & Shen, Z.X., 2007, Nature: 450(7166), 81. doi:10.1038/nature06219

[25] Kanigel, A,. Chatterjee, U., Randeria, M., Norman, M.R., Souma, S., Shi, M., Li, Z.Z., Raffy, H., & Campuzano, J.C., 2007, Physical Review Letters: 99(15), 157001. doi:10.1103/PhysRevLett.99.157001

[26] Teitel, S., & Jayaprakash, C., 1983, Phys. Rev. B: 27, 598. doi:10.1103/PhysRevB.27.598

[27] Wolff, U., 1989, Physical Review Letters: 62, 361. doi:10.1103/PhysRevLett.62.361

[28] Del Maestro A., & Affleck, I., 2010, Phys. Rev. B: 82, 060515. doi:10.1103/PhysRevB.82.060515

[29] Mangel, I., & Keren, A., 2024, Phys. Rev. B: 109, 094519. doi:10.1103/PhysRevB.109.094519

[30] Panagopoulos, C., Cooper, J.R., Xiang, T., Wang, Y.S., & Chu, C.W., 2000, Phys. Rev. B: 61(6) R3808. doi:10.1103/PhysRevB.61.R3808

[31] Wada, N., Taniguchi, J., Ikegami, H., Inagaki, S., & Fukushima, Y., 2001, Phys. Rev. Lett.: 86(19), 4322. doi:10.1103/PhysRevLett.86.4322

[32] Toda, R., Hieda, M., Matsushita, T., Wada, N., Taniguchi, J., Ikegami, H., Inagaki, S., & Fukushima, Y., 2007, Phys. Rev. Lett.: 99(25), 255301. doi:10.1103/PhysRevLett.99.255301

[33] Agterberg, D.F., Davis, J.S., Edkins, S.D., Fradkin, E., Van Harlingen, D.J., Kivelson, S.A., Lee, P.A., Radzihovsky, L., Tranquada, J.M., & Wang, Y., 2020, Annual Review of Condensed Matter Physics: 11(1), 231. doi:10.1146/annurev-conmatphys-031119-050711

[34] Li, Y.H., & Teitel, S., 1989, Phys. Rev. B: 40, 9122, 231. doi:10.1103/PhysRevB.40.9122

[35] Hrahsheh, F., & Vojta, T., 2012, Phys. Scripta: T151 014074. doi:10.1088/0031-8949/2012/T151/014074

[36] Sandvik, A.W., 2010, vol. 1297, pp. 135–338. American Institute of Physics. doi:10.1063/1.3518900

Chapter 6

Summary and Discussion

This chapter will summarise the three parts of the work in order.

6.1 Discussing the Stiffnessometer

The fundamental principle that the stiffnessometer is based on is the London equation $\mathbf{j} = \rho_s \left(\frac{\Phi_0}{2\pi}\nabla\phi - \mathbf{A}\right)$ where A is the VP, j_{sc} is the SC current density, and ρ_s is the SC stiffness. By changing the current in the EC we change $\mathbf{A}$ and the magnetic moment that we measure is proportional to j_s, so we can get ρ_s from the slope between the magnetisation and the current. Then we can use the relation $\rho_s = \frac{1}{\mu_0\lambda^2}$ to get λ.

But $\mathbf{A}$ in the London equation is the total VP which is the sum of the EC-VP and the SC-VP. Using Faraday's and London's equations, with $\mathbf{B} = \nabla \times \mathbf{A}$ we get a PDE which is solved numerically (after making it unite-less and assuming rotational symmetry). The numerical simulation along a cross section of the ring shows that the VP is most significant along the inner rim of the ring and nullifies in the middle of the cross Sec. 3.7. The VP is calculated on the PL. We consider the dimensions of the ring and the gradiometer used instead of a single PL and the parameters of the coil, to get a conversion between the normalized signal (the magnetic moment) to the stiffness (or λ), Fig. 3.8.

When the relation between A and j_s brakes, we know that we have reached the critical flux of the ring and from the relation $\frac{\Phi_c}{\Phi_0} = \frac{r_{out}^2}{\sqrt{8}\pi\mu_0\lambda\xi}$ we determine ξ. This relation takes into account λ, the geometry of the ring and the relation between the critical current density and ξ. A tentative explanation is in Chap. 4.3, and a full analytical derivation and numerical calculation comes from (22).

The experimental setup is an add-on to a CRYOGENICS susceptometer or a Quantum Design MPMS3 and both where used in this project. These magnetometers consist of a motor that can move a sample inside a temperature controlled chamber, and relative to a gradiometer connected to a SQUID. This way it can detect the change of magnetic flux through the gradiometer and determine the magnetic moment of the sample. An external coil can be used to create magnetic fields or in our case, cancel external fields. The use of a gradiometer instead of a single PL minimizes the noise. The stiffnessometer consists of a long and narrow excitation coil (EC) made in our lab. The EC diameter in this project is 60 mm long, with a 0.8 mm diameter, 2 layers and 1940 loops in total. The ring is placed on the middle of the coil and both of them move together in and out (of the other side) of the gradiometer and back the same way a number of times to have better statistics and smaller errors.

A few tests where made to validate our claim that the field outside our EC (which is not infinite) is negligible so that we can rightfully treat it as an infinite coil. The numerical simulation in Fig. 3.2 show the low magnetic field outside of the coil and the experiments with an open ring confirms that indeed the field out side of the coil is undetectable. It was also verified with a scanning SQUID on chip by scanning the surface of a thin $MoSi$ ring (8 nm of $MoSi$ grown on silicone wafer with 300 nm of silicone oxide). They found no visible relation between the current in the EC and the number of vertices in the sample (23).

Limitations: There are two main limitations for the technique in measuring ρ_s. From looking at the PDE solution, it is obvious that we are sensitive only when the dimensions of λ are close to the dimensions of the sample, because for smaller λ a small error in the moment leads to big error in the stiffness. When too close to T_c the initial current in the EC is bigger then the critical current of the ring in that temperature and the measurement is invalid. So we can measure the stiffness only close to T_c when λ is close to the dimensions of the sample. Other works with the stiffnessometer measured thin SC layers on a ring-shaped Si-substrate to have wider effective measurement range (27).

The main limitation in measuring ξ is that we need to know λ, so unless we rely on external measurements we will be limited to the same temperature range as λ. Another limitation of this method is that the numerical solution of the PDE is unit-less and we need to "calibrate" it with λ measurements at low temperature. In this work, we relayed

on μSR measurements (1).

But in spite of the limitations, there are significant advantages to our techniques. It requires no leads to be attached to the sample, forming SC/metal interface, and makes the sample preparation stage more complicated. There are no demagnetization factors that need to take into account and complicate the analysis. There is no direct magnetic field on the sample and so, no vortex dynamics to consider. There are also no out-of-equilibrium issues in these measurements. The same table top apparatus is used to measure λ, ξ, and T_c. The phase transition is very sharp and less sensitive to small impurity islands in the sample. And also, the measurements can be done very close to the critical temperature where both λ and ξ are on the same scale as the sample, which is a limitation for other techniques.

The main results of this part of the work is λ and ξ of LSCO $x = 0.17$ for $34.5 < T < 34.95$, Fig. 3.11. λ is in the scale of millimeters and ξ in the scale of microns. Direct measurements so close to T_c with a single apparatus are a significant contribution to science.

6.2 Discussing the ξ Measurements at Low T_c

The most common ways to find ξ are by measuring vortex diameter by Scanning tunneling microscope (STM) or by measuring H_{c2} and following the relation $\xi = \sqrt{\Phi_0/2\pi H_{c2}}$. But STM demands cleaving which are impossible in some samples or orientations, and for a very small ξ, huge magnetic fields are needed to reach H_{c2}. In our technique, we change the flux through the hole of the ring and the field in the bulk of the sample is small. Following the derivation by Gvish, Keneth and Keren (22), we have an expression for the relation between the critical flux of the ring Φ_c and ξ: $\frac{\Phi_c}{\Phi_0} = \frac{r_{out}^2}{\sqrt{8}\pi\mu_0\lambda\xi}$. This relation does not grow like ξ^{-2} and resembles the expression of the critical field of a type I SC $H_c \propto \frac{\Phi_0}{\sqrt{8}\pi\lambda\xi}$ (by GL (26), eq 4.20).

In a nut shell, the theory assumes that the ring cancels completely the change in magnetic flux by creating macroscopic persistent currents along a stripe of width λ in the inner rim of the ring. When the flux is increased, so does the current, until it reaches the critical current density j_c. Then, the order parameter (amplitude) starts to weaken and vanish from the inside out as the applied flux keep increasing, until the vanishing of the

OP reach the outer diameter of the ring. Now it is less costly (in terms of energy) for vertices to form and enter the inner hole of the ring and the SC losses its rigidity. The braking of the relation $\mathbf{j} = -\rho_s \mathbf{A}$ means that we have reached the critical flux of the ring. So, the critical flux depends on the critical current density, the outer diameter of the ring, and λ. This behavior of the OP was demonstrated numerically by simultaneous solution of the two coupled GL equations, though, a verification of the final expression was still needed.

The entering of the vertices can be explained when we look at the full expression for the SC current density, $\mathbf{j} = \rho_s \left(\frac{\Phi_0}{2\pi}\nabla\phi - \mathbf{A}\right)$. When cooling the sample with $\mathbf{A} = \mathbf{0}$, φ will be zero to minimize the energy. Now when we increase $\mathbf{A}$ below T_c, ϕ is fixed and changing it is equivalent to moving a vortex along the sample which can happen only when the SC circle is braking at some week point and the rigidity is lost.

The experimental system was similar to that of the stiffnessometer but because we needed to reach a very high magnetic flux, we did some adjustments to the system. Instead of using Cu wire, the EC was made from a SC wire with a diameter of 0.106 mm to carry more current and we reached maximal current of 12.4 A. The EC used had an external diameter of 1.95 mm, 8 layers, and 4800 loops in total to have higher flux-to-current ratio. The copper leads that connected the EC to the power source needed to be cooled during the measurements and a new set of pump lines were installed. We used the CRYOGENICS system for this experiment due to its superior cooling power compared to the QD MPMS3. Also, the LSCO rings needed to have a relatively small outer diameter so that we would reach the critical flux.

We also needed to change the way we measure because the signal from the coil exceeded the detection limits, so instead of looking at the voltage difference of the signal along a full rang scan of 80 mm, we looked at the second derivative over a very short range of 10 mm and extracted the magnetic moment from it.

The first objective in this project was to test the theory and it was done with pure Nb rings. We measured three sets of rings, where in each set only one parameter of the ring was changed and the others were fixed. In the first set we changed the inner diameter, in the second we changed the outer diameter, and in the third we changed the height. We found clear evidence that the critical flux was quadratic with the outer diameter of the rings and the theory was verified.

The second objective was measuring the anisotropic ξ in the ground state of LSCO with doping $x = 0.125$. For this purpose, a- and c-rings were cut from the same single crystal and measured at temperature of 1.6 k°.

When measuring the a-ring, the critical current in the EC was 2 A and the corresponding ξ_c is 1.3 ± 0.1 nm. The matching H_{c2} is $\backsim$ 195 T. It is also comparable to the unit cell length in the c direction 1.318 nm. In the c-ring measurements, we reached the maximal current that our SC EC could hold of 12.4 A, but the magnetization was linear all along. This means that we only have an upper limit which is $\xi_{ab} < 2.3$ nm. The fact that we were able to measure a smaller ξ in the a-rings is because of the much larger λ_c compared with λ_{ab} that play a role in the relation $\frac{\Phi_c}{\Phi_0} = \frac{r_{out}^2}{\sqrt{8}\lambda\xi}$. Our finding of comparable ξ_c and ξ_{ab} suggest that the cooper-pair in LSCO is isotropic at the ground state, regardless of the high anisotropy of the system.

6.3 Discussing the Two T_c Conundrum

The goal of the third part of the work was to find the origin of the evident difference in critical temperature of the SC stiffness in the CuO_2 planes and the SC stiffness between them. Kapon et-al (1) measured the stiffness of two rings from the same single crystal of LSCO with doping $x = 0.125$ and the a-ring's stiffness vanished 0.64 k below the c-ring's stiffness vanish. This means that in this 0.64 k range, persistent supercurrent can only flow parallel to the CuO_2 planes making the material a 2D SC. This is strange because according to the MV theorem, there can be no long-range order in 2D and no SC. Nonetheless, according to the BTK theory a power low decaying correlation length can exist in 2D under some temperature named T_C^{KTB}. But, the T_c^{KTB} must be smaller than the thermodynamic T_c (or T_C^{3D}) and here we observed the opposite situation, where $T_C^{3D} < T_C^{KTB}$. This was a strange finding.

One explanation could be Layer-correlated disorder, meaning, a gradient in the doping parameter between the CuO_2 layers (along the c vector). Such disorder is expected to manifest as a "tail" or broadening of the transition of the c-ring, but the observed tail in (1) or in this work - Fig. 5.2, are much smaller than the observed $_c$. So another explanation was considered; a finite size effect. Monte Carlo Simulations for the classical 3dXY model predicts that the inter-plane stiffness close to T_c is exponential in temperature, sample size,

and the coupling anisotropy. Combined with a finite detection limits the apparent end of the transition ($\tilde{T}_c^{\perp}$) will look smaller than the thermodynamic T_c. The correlation between sample size and the vanishing of the stiffness was tested theoretically and experimentally in this part of the work.

Near the thermodynamic (3D) T_c the inter-plane stiffness ρ_c experiences a 3dXY critical behavior and crossover to a one-dimensional XY (1dXY) chain with an exponentially flat temperature dependence. Since there is (always) an experimental detection limit, it can be seen as if ρ_c critical temperature is lower than the thermodynamic T_c.

The experimental setup for this experiment is very similar to the one in the first part of the work. We used the QD MPMS3 for this experiment, for its better temperature control. The coil we used was 60 mm long, made of Cu wire of 0.06 mm diameter, with 2 layers, and 1940 winding in total. Both a- and c-rings were cut from the same single crystal of LSCO with doping $x = 0.17$. To change the height of the rings, a fine-lapping device was used, and to change the radius we used the femtosecond laser. Instead of cutting all the outer rim of the ring to change the radius, we only cut a straight line because the relevant cross section is the narrowest one (the bottleneck).

The relevant lengths of the cross section depend on the crystalline structure. So when we change the height of the c-ring we change L_c and when we cut its radius we change L_a (or L_b but they are similar in our view). When we change the height of the a-ring we change L_a (or L_b) and we can cut its radius parallel to the CuO_2 layers and change L_c, or perpendicular and change L_b (or L_a). Figure 5.2(a-b) shows the rings and their cross-section.

The normalized magnetization as a function of temperature for different rings is presented in Fig. 5.2. The c-ring measurements (e) show a high-temperature tail of 0.5 k and consistent T_c except for the narrowest sample $La = 0.09$ suspected of containing a traversing cut. The a-ring (d) shows a clear monotonic dependence of $\tilde{T}_c^{\perp}$ in La. These findings confirm our assumption that the inter-layer is the weak link in the current's course. The difference between $\tilde{T}_c^{\perp}$ and $\tilde{T}_c^{\perp}$ is 7 times bigger than the high-temperature tail, making the Layer-correlated disorder explanation unlikely.

The Monte Carlo simulations for $\rho^{\perp}$ by the H_{3dXY} model and for two different anisotropy constants $\alpha = J_{\perp}/J_{\parallel}$, and several L_a are presented as dots in Fig. 5.5. The detection limit ϵ is marked by the red horizontal line and it can be seen how the apparent $_c$ increases with

the reduction of L_a. When anisotropy is stronger (α is smaller) the effect of L_a over $_c$ is bigger.

Near T_c and for small cross section, the system crossover to a quasi one-dimensional behavior and it can be described analytically by a classical $1dXY$ chain with inter-site coupling. Luttinger liquid theory comes in handy when the system is much larger than the lattice constant ($L \gg a$) and we get Eq. 5.12. The analytic $\rho^{\perp}$ is fitted to the simulations in Fig. 5.5 (solid lines).

The difference in T_c of the a-ring over L_a is shown in Fig. 5.6 with a fit of the analytical results to data. The parameters are $\alpha^{fit} = 4.1 \times 10^{-5}$ and $\tilde{T}_c^{\perp} = 36.5$ k. There is an offset to the fit which we denote to layer-correlated disorder, seen also in the high temperature tail of the c-ring.

Reported α at $T \to 0$ are of order 4.6×10^{-3} which is two orders bigger than the fitted α. A possible explanation for this difference is the formation of thermal excitation of nodal quasiparticles of the d-wave superconductor and inter-planar vortex rings.

Bibliography

[1] Kapon, I., Salman, Z., Mangel, I., Prokscha, T., Gavish, N., & Keren, A., 2019, Nature Communications, 10(1), doi:10.1038/s41467-019-10480-x

[2] Mermin, N.D., & Wagner, H., 1966, Physical Review Letters, 17(22):1133–1136, doi:10.1103/physrevlett.17.1133

[3] Kosterlitz, J.M., & Thouless, D.J., 1978, Progress in Low Temperature Physics, 371–433, doi:10.1016/s0079-6417(08)60175-4

[4] Uchida, S., 2003, Solid State Communications, 126(1-2):57–61, doi:10.1016/s0038-1098(02)00671-3

[5] Plakida, N., 2010, Springer Series in Solid-State Sciences, 51–120, doi:10.1007/978-3-642-12633-8-3

[6] Keimer, B., Kivelson, S.A., Norman, M.R., Uchida, S., & Zaanen, J., 2015, Nature, 518(7538):179–186, doi:10.1038/nature14165

[7] Damascelli, A., Hussain, Z., & Shen, Z.X., 2003, Reviews of Modern Physics, 75(2):473–541, doi:10.1103/revmodphys.75.473

[8] Koohpayeh, S.M., Fort, D., & Abell, J.S., 2008, Progress in Crystal Growth and Characterization of Materials, 54(3-4):121–137, doi:10.1016/j.pcrysgrow.2008.06.001

[9] Lawrence, W.E., & Wilkins, J.W., 1973, Physical Review B, 7(6):2317–2332, doi:10.1103/physrevb.7.2317

[10] MacDonald, A.H., Taylor, R., & Geldart, D.J.W., 1981, Physical Review B, 23(6):2718–2730, doi:10.1103/physrevb.23.2718

[11] Barisic, N., Chan, M.K., Li, Y., Yu, G., Zhao, X., Dressel, M., Smontara, A., & Greven, M., 2013, Proceedings of the National Academy of Sciences, 110(30):12235–12240, doi:10.1073/pnas.1301989110

[12] Takagi, H., Batlogg, B., Kao, H.L., Kwo, J., Cava, R.j., Krajewski, J.J., & Peck, W.F., 1992, Physical Review Letters, 69(20):2975–2978, doi:10.1103/physrevlett.69.2975

[13] Komiya, S., Ando, Y., Sun, X.F.,& Lavrov, A.N., 2002, Physical Review B, 65(21), doi:10.1103/physrevb.65.214535

[14] Boebinger, G.S., Ando, Y., Passner, A., Kimura, T., Okuya, M., Shimoyama, J., Kishio, K., Tamasaku, K., Ichikawa, N., & Uchida, S., 1996, Physical Review Letters, 77(27):5417–5420, doi:10.1103/physrevlett.77.5417

[15] Drachuck, G., Shay, M., Bazalitsky, G., Berger, J., & Keren, A., 2012, Physical Review B, 85(18), doi:10.1103/physrevb.85.184518

[16] Felner, I., Tsindlekht, M.I., Drachuck, G., & Keren, A., 2013, Journal of Physics: Condensed Matter, 25(6):065702, doi:10.1088/0953-8984/25/6/065702

[17] Li, Q., Hücker, M., Gu, G.D., Tsvelik, A.M., & Tranquada, J.M., 2007, Physical Review Letters, 99(6), doi:10.1103/physrevlett.99.067001

[18] Wang, Y., & Wen, H.H., 2008, Europhysics Letters, 81(5):57007, doi:10.1209/0295-5075/81/57007

[19] Wen, H.H., Yang, H.P., Li, S.L., Zeng, X.H., Soukiassian, A.A., Si, W.D., & Xi, X.X., 2003, Europhysics Letters, 64(6):790–796, doi:10.1209/epl/i2003-00627-1

[20] Fujita, K., Noda, T., Kojima, K.M., Eisaki, H., Uchida, S., 2005, Physical Review Letters, 95(9):790–796, doi:10.1103/physrevlett.95.097006

[21] Mangel, I., Kapon, I., Blau, N., Golubkov, K., Gavish, N.,& Keren, A., 2020, Physical Review B, 102(2), doi:10.1103/physrevb.102.024502

[22] Gavish, N., Kenneth, O., & Keren, A., 2021, Physica D: Nonlinear Phenomena: 415, 132767. doi:10.1016/j.physd.2020.132767

[23] Khanukov, A., Mangel, I., Wissberg, S., Keren, A., & Kalisky, B., 2022, Phys. Rev. B 106, 144510. doi:10.1103/PhysRevB.106.144510

[24] Mangel, I., & Keren, A., 2024, Phys. Rev. B: 109, 094519. doi:10.1103/PhysRevB.109.094519

[25] Samanta, A., Mangel, I., Keren, A., Arovas, D.P., & Auerbach, A., 2024, SciPost Phys. 16, 148. doi:10.21468/SciPostPhys.16.6.148

[26] Tinkham M., Introduction to Superconductivity, Courier Corporation, North Chelmsford, MA, 2004.

[27] Keren, A., Blau, N., Gavish, N., Kenneth, O., Ivry, Y., & Suleiman, M., 2022, Supercond. Sci. Technol. 35 075013. doi:10.1088/1361-6668/ac7173

תקציר

הודות לתכונות היחודיות של מוליכי-על והשימושים האפשריים שלהם, המחקר בתחום ממשיך לעמוד בחזית המדע. מוליכי-על נמצאים בשימוש במגוון תחומים אך השימוש בהם מוגבל לעבודה בטמפרטורות נמוכות ובמידה וימצא מוליך על בטמפרטורת החדר התגלית תוביל למהפכה טכנולוגית. במסגרת החיפוש המתמיד אחר מוליכי על חדשים, עולה הצורך בפיתוח שיטות מדידה חדשניות. הקבוצה שלנו פיתחה שיטה חדשה, בעלת יתרונות משמעותיים. בין היתרונות, העובדה כי המערכת נמצאת בשיווי משקל טרמודינמי במהלך המדידה, היא אינה דורשת מגעים, ניתן להזניח בה מערבולות כיוון שאין שדה מגנטי ישיר על הדגם, וכן השיטה מבוססת על מכשיר מסחרי ונפוץ.

השיטה מבוססת על סליל דק וארוך באמצעותו ניתן להשרות זרם בטבעת מוליכת-על ואת הזרם ננתן לחשב באמצעות מדידת המומנט המגנטי של הטבעת. בדוקטורט עבדתי על פיתוח השיטה וישומה למדידת $La_{2-x}Sr_xCuO_4$ (לסקו) שהינו מוליך-על בטמפרטורה גבוהה ממשפחת הקופרטים. הקופרטים אטרקטיבים במיוחד משום שלחלקם טמפרטורה קריטית גבוהה מאוד. לסקו, בדומה ליתר משפחת הקופרטים, מורכב משכבות של נחושת-חמצן ואלמנטים כבדים בין השכבות, ומאופיין באנאיזוטרופיה משמעותית. ה x בנוסחה הכימית מראה את רמת סימום החורים של המערכת ($holedoping$).

העבודה מורכבת משלושה מאמרים. המאמר הראשון מסביר את הטכניקה בפירוט, ומציג מדידות של עומק החדירה ואורך הקוהרנטיות בקרבת הטמפרטורה הקריטית עבור דגם לסקו עם סימום $x = 0.17$.

המאמר השני עוסק במדידה של אורך הקוהרנטיות האנאיזוטרופי במצב היסוד. תחילה, נבחנת השיטה באמצעות ניוביום עבורו הפרמטרים של עומק החדירה ואורך הקוהרנטיות ידועים. לאחר מכן, מוצגות התוצאות עבור לסקו עם סימום $x = 0.125$. בניסוי זה נמדדו שתי טבעות שנחתכו מאותו גביש יחידני אבל עם אוריאנטציות שונות. בטבעת אחת מישורי הגביש מקבילים לציר הסימטריה של הטבעת ולכן הזרם חייב לעבור בין מישורים (טבעת a), בטבעת השניה המישורים ניצבים לציר הסימטריה של הטבעת והזרם נע במקביל למישורים (טבעת c). ניתן להעריך את אורך הקוהרנטיות של החומר מתוך מדידה של הזרם המקסימלי שניתן להשרות בטבעת. מטבעת a נקבל את הערך שלו בניצב למישורים ומטבעת c נקבל את הערך המקביל למישורים וכך נמדוד את אורך הקוהרנטיות האנאיזוטרופי של החומר. הצלחנו למדוד את אורך הקוהרנטיות בכיוון הניצב $\xi_c = 1.3 \pm 0.1\ nm$, אבל עבור הכיוון המקביל קיבלנו רק חסם עליון $\xi_{ab} < 2.3\ nm$. הערכים שקיבלנו באמצעים פשוטים מקבילים למדידות שדה מגנטי קריטי של כמה מאות טסלה.

המאמר השלישי עוסק בחקר האנאיזוטרופיה של הטמפרטורה הקריטית. למרות האנאיזוטרופיה של החומר אשר באה לידי ביטוי בתכונות שונות, עמורה להיות טמפרטורה קריטית אחת בלבד. עם זאת, קיימות מספר תצפיות שהראו כי עבור דגם בו הזרם חוצה את המישורים הטמפרטורה הקריטית נמוכה מאשר בדגם בו הזרם תמיד מקביל למישורים. עלה החשד שלגודל הדגם יש השפעה על הטמפרטורה בה הזרם המושרה ידעך וכדי לבדוק השערה זו הוכנו זוג טבעות a ו c מאותו גביש יחידני של לסקו $x = 0.125$. הטמפרטורה הקריטית נמדדה מספר פעמים עבור כל טבעת ובין מדידה למדידה שינינו את גובה הטבעת או את הרדיוס החיצוני שלה כדי למדוד את ההשפעה על הטמפרטורה הקריטית. הניסויים הראו שקיים קשר בין גודל שטח החתך של טבעת a לבין הטמפרטורה הקריטית. החלק התאורטי של המאמר מציג חישובים מספריים עבור מודל $3Dxy$ המראים שקרוב לטמפרטורה הקריטית המערכת מתנהגת כמו שרשרת חד-ממדית של צמתי ג'וזפסון. הסימולציות מראות שגודל שטח החתך בו הזרם ניצב למישורים משפיע על צורת מעבר הפאזה ושהטמפרטורה הקריטית תראה שונה עבור רזולוצית מדידה סופית. המודל החד-ממדי מספק ביטוי אנליטי אותו התאמנו לתוצאות הניסוי וקיבלנו שערך האנאיזוטרופיה בחומר בקרבת הטמפרטורה הקריטית הינו 4.1×10^{-5}.

המחקר בוצע בהנחייתו של פרופסור עמית קרן, בפקולטה לפיזיקה.
חלק מהתוצאות בחיבור זה פורסמו כמאמרים מאת המחבר ושותפיו למחקר בכנסים ובכתבי-עת במהלך תקופת מחקר הדוקטורט של המחבר, אשר גרסאותיהם העדכניות ביותר הינן:

Mangel, I., Kapon, I., Blau, N., Golubkov, K., Gavish, N., & Keren, A. 2020, Stiffnessometer: A magnetic-field-free superconducting stiffness meter and its application, PHYSICAL REVIEW B 102, 024502 (2020)
Mangel, I., & Keren, A. 2024, Ground-state Inter-plane Superconducting Coherence Length of $La_{1.875}Sr_{0.125}CuO_4$, PHYSICAL REVIEW B 109, 094519 (2024)
Samanta, A., Mangel, I., Keren, A., Arovas, D.P., & Auerbach, A. 2024, Two critical temperatures conundrum in $La_{1.83}Sr_{0.17}CuO_4$, SciPost Phys. 16, 148 (2024)

הצהרת אתיקה

ככותבת התזה אני מצהיר שהמחקר, כולל איסוף, עיבוד והצגת המידע, השוואה למחקר קודם, וכו', בוצע באופן ישר לחלוטין כמצופה ממחקר מדעי שמבוצע בהתאם לסטנדרט האתי בעולם האקדמיה. בנוסף, הצגת המחקר ותוצאותיו בתזה זו נעשה באופן ישר ומקיף, בהתאם לאותו הסטנדרנט.

תודות

אני מודה לקרן הלאומית למדע על התמיכה הכספית הנדיבה בהשתלמותי.

מדידת אורך הקוהרנטיות הבין-שכבתי וחקר האנאיזוטרופיה של הטמפרטורה הקריטית של $LSCO$

חיבור על מחקר

לשם מילוי חלקי של הדרישות לקבלת התואר
דוקטור לפילוסופיה

איתי מנגל

הוגש לסנט הטכניון- מכון טכנולוגי לישראל
אב התשפ"ד חיפה אוגוסט 2024

מדידת אורך הקוהרנטיות הבין-שכבתי וחקר האנאיזוטרופיה של הטמפרטורה הקריטית של $LSCO$

איתי מנגל